SMALL-SCALE POLYMER STRUCTURES ENABLED BY THIOL-ENE COPOLYMER SYSTEMS

A Dissertation
Presented to
The Academic Faculty

By

Scott Edward Kasprzak

In Partial Fulfillment
Of the Requirements for the Degree
Doctor of Philosophy in Mechanical Engineering

Georgia Institute of Technology

May 2009

SMALL-SCALE POLYMER STRUCTURES ENABLED BY THIOL-ENE COPOLYMER SYSTEMS

Approved by:

Dr. Kenneth Gall, Advisor
G.W.W. School of Mechanical Engineering
School of Materials Science & Engineering
Georgia Institute of Technology

Dr. Karl Jacob
School of Polymer, Textile and Fiber Engineering
G.W.W. School of Mechanical Engineering
Georgia Institute of Technology

Dr. Samuel Graham
G.W.W. School of Mechanical Engineering
Georgia Institute of Technology

Dr. Joseph Perry
School of Chemistry & Biochemistry
Georgia Institute of Technology

Dr. Olivier Pierron
G.W.W. School of Mechanical Engineering
Georgia Institute of Technology

Date Approved: 27 March 2009

To Marianna, the light for my path

And to Henry, my reason for walking it.

ACKNOWLEDGEMENTS

First and foremost, I would like to thank my wife, Marianna, for standing by me through the long and arduous process that is described in this treatise. Without her unflinching moral and emotional support and ready supply of sumptuous food, I would surely have failed in my endeavor. I would like to acknowledge her depthless patience for my quirks and her endless and tireless nurturing that she has provided for our son, Henry. Secondly, I would like to thank Henry for his mirth and good nature. Merely witnessing his learning and growth has surely made me appreciate life and all that I have learned ever more with each passing day. Both of these individuals are the very core of my being, and I could not live without them. Without humor, life is a dark passage, and without love, life is merely existence.

The next group of people I would like to acknowledge is all of my family and friends. I certainly would not be the person I am today (or indeed ***a*** person) without the love and support of my parents. Thank you for everything you have given me. I also want to thank my other parents (the ones I got by marriage) for showing me a new kind of joy and for opening your life and family and home to me. To my brother, Andy, and sister, Megan, thank you for growing up with me and for sticking together through the best and the worst. I learned different lessons from each of you and they have helped to shape the person I am today. To my new brothers Michele and Stefano, thanks for keeping me young and sharp and "on my toes." I especially enjoy the time we spend relaxing and enjoying the non-academic parts of life (i.e. videogames …).

The friends who have helped me greatly in my time at Georgia Tech are also my labmates. Thank you all for your friendship and for the unique way in which you provided help in one form or another. Each of you will agree that our office has a unique dynamic that allows each of us to feed on one another's knowledge and experience in such a way that all are enriched for it. Thank you: to Matthew Di Prima, for your candor and unflinchingly grueling work ethic – you helped keep me on track, whether you know it or not; to Dave Safranski, "the other Delawarean," for your interesting and often random forays into polymer mechanics and other sundry academic pursuits out on the whiteboard in the hall; to Kathryn Smith, for your chipper attitude and your (frankly hilarious) propensity for "losing" your keys, cell phone, or BuzzCard; to Walter Voit, for your endless dreaming and for teaching me Die Siedler von Catan, which is a great way to sharpen the brain; to Terra Keim (well, Kissel now) for your companionship in the early classes and for "leading the way" with your master's thesis; and to Edem Wornyo for the in-depth discussions on nanoindentation and the merits of the Hysitron and MTS machines. Certainly, the many (many) undergraduates who have spent time in our group have formed relationships with me, and I thank you for taking the time out of your busy schedules to chat and become friends with a lowly graduate student.

I would also like to take this opportunity to thank my advisor, Dr. Ken Gall, for taking a risk on me when no one else would. Throughout the years his intelligent mentoring and friendship have meant the world. I want to thank Ken for his openness and for treating me and all of his other graduate students like equals, even when we hadn't earned it. His personality, guidance, and philosophy of personal independence are the core elements

which help to insure that everyone in the lab meshes well to create a research synergy and that we each grow to fulfill our own full potential.

I would like to thank the collaborators and undergraduates who have helped to make this research a reality in the form of journal submissions: Vincent Chen and Dr. Joseph Perry, for your expertise with two-photon stereolithography and for making me samples which I could indent; Tulika Raj and Blanton Martin, for all the work you put in to help me create and characterize polymers made of the most stench-ridden monomers available; and Brock Wester, for all of the photopatterning experience and advice, for the initial photomasks, for the time spent working in the cleanroom using the collimated UV source, and for making the connection to get SEM pictures taken by a friend when the SEM I had access to was down for weeks.

I also want to thank my committee members, Dr. Karl Jacob, Dr. Samuel Graham, Dr. Olivier Pierron, and Dr. Joseph Perry, for lending their expertise and experience to me for discussions and suggestions through the course of this work. And, of course, for taking the time out of their busy schedules to be a part of the reading committee for this dissertation.

Finally, real research is funded by real dollars, so I want to extend my thanks to the National Institutes of Health for funding this effort.

TABLE OF CONTENTS

ACKNOWLEDGEMENTS iv

LIST OF TABLES x

LIST OF FIGURES xi

LIST OF SYMBOLS AND ABBREVIATIONS xiv

CHAPTER 1. INTRODUCTION 1

1.1. Motivation 1

1.2. Problem Definition 2

1.3. Materials 4

1.3.1. Polymers 4
1.3.2. Shape Memory Materials 5
1.3.3. (Meth)acrylates 8
1.3.4. Thiol-enes 11

1.4. Testing and Evaluation Methods 15

1.4.1. Nanoindentation 15
1.4.2. Dynamic Mechanical Analysis 16
1.4.3. Photo Differential Scanning Calorimetry 20
1.4.4. Mechanical Testing 21
1.4.5. Fourier Transform Infrared Spectroscopy 21
1.4.6. Microscopy 23
1.4.7. Sol-Fraction 23

1.5. Purpose and Scope of Research 24

CHAPTER 2. NANOINDENTATION OF MICROSCALE POLYMER STRUCTURES FABRICATED VIA TWO-PHOTON STEREOLITHOGRAPHY 26

2.1. Summary 26

2.2. Introduction 27

2.2.1. Two-Photon Stereolithography 27
2.2.2. Nanoindentation 28

2.3. Experimental 47

2.3.1. Materials 47
2.3.2. Methods 48

2.4. Results 50

2.5. Discussion 55

2.6. Conclusions 58

CHAPTER 3. SYNTHESIS AND THERMOMECHANICAL BEHAVIOR OF (QUA)TERNARY THIOL-ENE(/ACRYLATE) COPOLYMERS 60

3.1. Summary 60

3.2. Introduction 61

3.3. Experimental 63

3.3.1. Materials 63
3.3.2. Methods 66

3.4. Results 68

3.5. Discussion 77

3.6. Conclusions 87

CHAPTER 4. PHOTOPATTERNING OF THIOL-ENE/ACRYLATES 89

4.1. Summary 89

4.2. Introduction 90

4.3. Experimental 92

4.3.1. Materials 93
4.3.2. Methods 95

4.4. Results 98

4.5. Discussion 110

4.6. Conclusions 113

CHAPTER 5. CONCLUSION 115

APPENDIX A: NANOINDENTATION OF TWO-PHOTON POLYMERS 120

APPENDIX B: SUPPLEMENTAL OPTICAL/ELECTRON IMAGES OF PHOTOPATTERNED POLYMERS..... 125

REFERENCES 135

LIST OF TABLES

Table 2.1. Exposure conditions for SR9020 structures..... 48

Table 3.1. Monomer mixtures used in study..... 65

Table 4.1. Thiol-ene/acrylate mixtures used in study. 95

Table 4.2. 2^3 factorial design experiment matrix for screening study. 97

Table 4.3. 2^3 factorial design experiment matrix for second-level study. 98

Table 4.4. Total exotherm for polymerized materials..... 102

Table 4.5. Results of first round of 2^3 factorial design study. 106

Table 4.6. Results from the second round of 2^3 factorial design study. 107

LIST OF FIGURES

Figure 1.1. Schematic of the shape memory effect. 7

Figure 1.2. Chemical structure of (a) a methacrylate and (b) an acrylate. 8

Figure 1.3. Chemical structure of (top) a dithiol and (bottom) a diene. 11

Figure 1.4. The thiol-ene reaction scheme. 13

Figure 1.5. Example strain and stress data of viscoelastic material 17

Figure 2.1. Geometry of elastic half-space and conical indenter in cut-away view. 30

Figure 2.2. Typical load vs. depth indentation compliance curve. 32

Figure 2.3. Side cut-away view of components of nanoindenter transducer. 37

Figure 2.4. Exaggerated deflection of compliant load frame 47

Figure 2.5. Chemical structure of SR9020 47

Figure 2.6. Optical micrographs of two-photon polymerized bars. 50

Figure 2.7. Results from dynamic mechanical analysis of SR9020 51

Figure 2.8. Compliance curves for representative processing conditions. 52

Figure 2.9. Graph of unload modulus, grouped by exposure condition. 53

Figure 2.10. Graph of indentation hardness at maximum load (quasistatic). 54

Figure 2.11. Elastic modulus vs. dose for SR9020 structures, using n=4 photons for multi-photon dose calculations. 55

Figure 3.1. Chemical structures of studied monomers. 64

Figure 3.2. Progression of storage modulus for thiol-crosslinked ternary mixtures, by $t_f$mol% crosslinker. 69

Figure 3.3. Progression of storage modulus for -ene-crosslinked ternary mixtures, by $e_f$mol% crosslinker 69

Figure 3.4. Glass transition temperatures for various ternary mixtures 70

Figure 3.5. Rubbery moduli for various ternary mixtures 71

Figure 3.6. Glass transition temperatures for (qua)ternary mixtures 72

Figure 3.7. Rubbery moduli for (qua)ternary mixtures..... 72

Figure 3.8. (top left) Example FTIR spectra (top right) sample area used for peak calculation and (bottom) C=C conversion for various mixtures. 74

Figure 3.9. Sol-fraction mass loss for six tested mixtures. 75

Figure 3.10. Stress-strain behaviors for various thiol-ene/acrylate mixtures. 76

Figure 3.11. Failure stress for (qua)ternary mixtures of thiol-ene/acrylate 76

Figure 3.12. Failure strain for (qua)ternary mixtures of thiol-ene/acrylate 77

Figure 3.13. Failure strain versus “molecular weight between crosslinks”..... 85

Figure 3.14. Failure stress versus “molecular weight between crosslinks”..... 85

Figure 3.15. Failure strain versus rubbery modulus 86

Figure 4.1. Chemical structures of studied monomers. 94

Figure 4.2. DMA curves for 50TATATO+50BPAEDA(512), 30.2BPAEDA(512)69.8PEGPEA(236) and 10PETMP+25BPAEDA(512). 99

Figure 4.3. PhotoDSC heat flow curves for studied materials..... 100

Figure 4.4. (Top) Conversion vs. time and dose curves full scale and (bottom) low dose detail for studied materials..... 101

Figure 4.5. Comparison of photopatterning..... 103

Figure 4.6. Internal and external corner patterning comparison 104

Figure 4.7. Additional photopatterned structures made with 50TATATO+50BPAEDA(512). 105

Figure 4.8. Optical microscopy images of (top) photomask and (bottom) resultant photopatterning of 10PETMP+25BPAEDA(512).. 106

Figure 4.9. Optical micrographs of structures from first factorial design study.. 107

Figure 4.10. Underdeveloped features from second level factorial design study.. 108

Figure 4.11. Well-developed structures from second factorial design study..... 109

Figure 4.12. Optical micrographs showing (a) negative and (b) positive features.. 110

Figure A.1. Two-photon squares of 50:50 wt:wt mixture of SR9008:SR368. 120

Figure A.2. Two-photon squares with (a) good and (b) poor processing conditions. 121

Figure A.3. Portion of second generation two-photon array of SR9008:SR368. 122

Figure A.4. Detail views of bars with (a) good and (b) poor development. 122

Figure A.5. CSM modulus for second generation two-photon array..... 123

Figure A.6. CSM hardness for second generation two-photon array. 123

Figure B.1. Additional photopatterned structures of 10PETMP+25BPAEDA(512)..... 125

Figure B.2. Optical microscope image of tweezer shape..... 126

Figure B.3. Other shapes from photopatterning screening studies. 127

Figure B.4. Optical images of photomask and bottoms of gears. 128

Figure B.5. Optical images from screening study using exposure chamber..... 129

Figure B.6. Structures from first factorial design study..... 129

Figure B.7. Images from slide 1, factorial design study round 2. 130

Figure B.8. Probe tips from slide 2, factorial design study round 2. 130

Figure B.9. Structures from slide 4, factorial design study round 2. 131

Figure B.10. Structures from slide 6, factorial design round 2. 132

Figure B.11. Structures from slide 7, factorial design round 2, showing poor development. 133

Figure B.12. Oblique SEM images of structures from round 2. 133

Figure B.13. Oblique SEM images of gear arrays from round 2. 134

Figure B.14. Various views of a small gear from round 2..... 134

LIST OF SYMBOLS AND ABBREVIATIONS

α	Cone semi-angle
a	Radius of contact
$a_f$mol%	Acrylate functionality molar percent
A	Area
AFM	Atomic force microscope
β	Geometry correction factor
BPAEDA(512)	Bisphenol A ethoxylate diacrylate, M_n 512
CSM	Continuous stiffness measurement
δ	Loss factor
DCM	Dynamic contact module
DMA	Dynamic mechanical analysis
DMPA	2,2-dimethoxy-2-phenylacetophenone
DSI	Depth-sensing indentation
DSC	Differential scanning calorimetry
dP/dh	Unload stiffness
ε	Engineering strain
ε_0	Strain magnitude
$\dot{\varepsilon}$	Strain rate
$e_f$mol%	Ene functionality molar percent
E	Young's modulus
E'	Storage modulus
E"	Loss modulus
E_i	Modulus of indenter tip

E_r	Reduced modulus
FTIR	Fourier transform infrared [spectroscopy]
h_a	Distance from initial specimen free surface to circle of contact
h_p	Actual penetration depth
h_t	Total penetration depth
I	Intensity
MEMS	Microelectromechanical systems
η	Dynamic viscosity
n	Number of photons
NMAT	Nanomechanical actuating transducer
NMR	Nuclear magnetic resonance [spectroscopy]
P	Load
PDT	1,3-propanedithiol
PEGPEA(236)	Poly(ethylene glycol) phenyl ether acrylate, M_n 236
PETMP	Pentaerythritol *tetrakis*(3-mercaptopropionate)
PI	photoinitiator
σ	Engineering stress
σ_0	Stress magnitude
σ_y	Engineering yield stress
S	Stiffness
SEM	Scanning electron microscope
t	Time
$t_f$mol%	Thiol functionality molar percent
TATATO	1,3,5-triallyl-1,3,5-triazine-2,4,6(1H,3H,5H)-trione
TMPDAE	Trimethylolpropane diallyl ether

T_g	Glass transition temperature
u_E	Uncertainty in Young's modulus
u_υ	Uncertainty in Poisson's ratio
UV	Ultraviolet
υ	Poisson's ratio
υ_i	Poisson's ratio of indenter tip
v	Stage translation speed
ω	Oscillation frequency

SUMMARY

The research described herein is aimed at exploring the thermo-mechanical properties of thiol-ene polymers in bulk form, investigating the ability of thiol-ene polymers to behave desirably as photolithographic media, and providing the first characterization of the mechanical properties of two-photon stereolithography-produced polymer structures. The thiol-ene polymerization reaction itself is well-characterized and described in the literature, but the thermomechanical properties of thiol-ene and thiol-ene/acrylate polymers still require more rigorous study. Understanding the behavior of thiol-ene networks is a crucial step towards their expanded use in bulk form, and particularly in specialized applications such as shape memory devices. Additionally, the thiol-ene polymerization reaction mechanism exhibits unique properties which make these polymers well suited to photolithography, overcoming the typical dichotomy of current materials which either exhibit excellent photolithographic behavior or have controllable properties. Finally, before two-photon stereolithography can create mechanisms and devices which can serve any mechanically functional role, the mechanical properties of the polymers they produce must be quantitatively characterized, which is complicated by the extremely small scale at which these structures are produced. As such, mechanical characterization to date has been strictly qualitative.

Characterization of bulk materials was both mechanical and chemical. Fourier transfer infrared spectroscopy revealed functional group conversion information and sol-fraction testing revealed the presence of unconverted monomer and impurities, while dynamic mechanical analysis (DMA) and tensile testing revealed the thermomechanical responses

of the systems. Nanoindentation was employed to characterize the mechanical properties of micrometer-scale polymer structures produced by two-photon stereolithography. Optical and electron microscopy were exploited to provide both quantitative and qualitative evaluations of thiol-ene/acrylate and acrylate performance in small-scale polymerization regimes.

The broad **objective** of the research was to explore thiol-ene polymer behavior both in bulk and at the small scale in an effort to supplement the material library currently used in these fields and to expand the design envelope available to researchers. The **significance** of the research is the advancement of a more complete and fundamental understanding of thiol-ene polymerization from kinetics to final properties, the quantitative establishment of the mechanical properties of materials created with two-photon stereolithography, and the comprehensive characterization of a supplementary class of photopatternable polymers with greater property tunability than is possible with currently used materials.

CHAPTER 1. INTRODUCTION

1.1. Motivation

Polymer photolithography has featured (meth)acrylate monomers, almost to the exclusion of other materials, since the very inception of the technique. Typically, highly functional acrylate monomers are used to insure rapid polymerization and pattern fidelity; these highly crosslinked networks shrink less than networks formed from lower functionality monomers. As a direct result of the high crosslink density (or low molecular weight between crosslinks) and monomer chemistry, these networks exhibit qualitatively glassy behavior at ambient temperatures - e.g. high stiffness and low ductility. Therefore, researchers are forced to choose between insuring pattern transfer fidelity and controlling the mechanical properties of the polymer. However, one of the newest techniques for patterned photopolymerization, called two-photon stereolithography, yields polymers with as yet undetermined thermomechanical properties. (Meth)acrylates are also used for shape memory applications, where such materials can be deformed to a metastable "stored" state and then be activated to recover to their initial shape in an automatic and controlled fashion, because the glass transition temperature (T_g) and rubbery modulus (E_r) can be tailored independently to suit a particular application.

There is another class of polymer, called thiol-ene, that is also readily photopolymerizable and may be well-suited to these same applications, complementing and perhaps partially replacing the use of pure (meth)acrylates while expanding the range of achievable properties. Therefore, this research was motivated by the possibility of thiol-ene polymers to replace (meth)acrylate polymers for small-scale applications and

complement them in shape memory devices, as well as by the need to determine a process-property map for two-photon and other photolithography techniques. Furthermore, the research was motivated by the need to establish a link between bulk properties and the behavior of the polymer in small-scale roles.

1.2. Problem Definition

Thiol-ene polymers have recently reemerged on the academic stage as a material system of interest because of their ability to readily photopolymerize. This photopolymerization can be carried out under ambient conditions and in the presence of oxygen, and is very rapid. Many studies have delved into the roles of various processing parameters on the polymerization reaction itself [1-27], while fewer have studied any of the resultant thermomechanical properties of the polymers [28-39]. The properties of these polymers are addressed by two related questions:

- What are the thermo-mechanical properties of various thiol-ene and thiol-ene/acrylate copolymers?

- Can the resultant properties of thiol-ene polymers be predicted (at least qualitatively) and controlled by changes in monomer chemistry?

Additionally, there are benefits of the thiol-ene polymerization scheme over typical (meth)acrylate polymerization which may make thiol-ene polymers an excellent choice for small-scale devices. This possibility was explored, as stated below:

- What benefits do the thiol-ene polymers provide for photolithography?

Two-photon stereolithography has emerged as one of the highest resolution polymerization schemes, with the ability to form solid polymer at the submicrometer level. This technique has led to the creation of microdevices, such as optical waveguides, at a scale and resolution that was impossible before. However, given the relatively recent invention of this technique and scale at which its products are created, little is known about the final properties of the product beyond optical observations and some chemical analysis. Therefore, this lack of knowledge was addressed by this research, as stated in the two questions below:

- What are the mechanical properties of polymers created by two-photon stereolithography, and how do the processing parameters affect them?

- How do these properties at the small scale compare to bulk-polymerized material?

Understanding and controlling the behavior of thiol-ene polymers are key steps required for their widespread adoption in photolithography at the small scale and in bulk applications, such as shape memory devices. Additionally, knowledge of the properties of two-photon polymerized materials, especially as compared to the bulk material, will allow researchers to create mechanically functional, three-dimensional devices with this technique. Integration of these new polymer components can expand the capabilities and applications of microscale devices, such as silicon-based MEMS.

1.3. Materials

1.3.1. Polymers

Polymers differ from most engineering materials in that they are large macromolecules, or chains, composed of hundreds to millions of smaller repeat units, called monomers. They are formed by various kinds of polymerization reactions, which are classified by the way the monomers react, the impetus for the polymerization reaction, the materials used, or the method used. The main classes of polymerization include: step vs. chain growth, addition vs. condensation, solvent-less vs. solvent vs. emulsion, catalyzed vs. radiation-induced, ionic vs. free radical, etc. The polymer can be further classified by their chain structures, the ordering of the monomers, or by the chemicals used to make them. Thermoplastic polymers, for example, can be dissolved in solvents and melted at elevated temperatures because the chains are physically entangled and not chemically linked, whereas thermoset polymers are three-dimensional networks which are chemically crosslinked and so will only swell in solvent and will degrade instead of melting at elevated temperatures [40-44]. Thermoplastic polymers can be further classified by the chain structure, such as linear, short or long branched, star-branched and so forth.

The polymers that were used in this research are all free-radical, solvent-less, radiation induced (often called photopolymerization because of the photons which carry the electromagnetic energy), and are step or chain growth reactions. Chain growth polymerization proceeds by addition of monomeric species to a radical core started by the initiator. In the step-growth mechanism involving two complimentary functional group types A and B, each A-type group can react with any other B-type group so monomer

pairs react and form into dimers, then trimers will form upon a further reaction step, until trimers grow to form oligomers and finally polymer chains. In chain-growth, there are two species sizes – growing chain-size and monomers; in step-growth, there is a broad distribution of sizes present at any given time, ranging from monomer to dimer to trimer to oligomer to full chains, where long chains do not develop until the reaction is nearly complete. In the free-radical polymerization scheme, an initiator sensitive to the wavelength of incident radiation, such as the ultraviolet (UV) initiator 2,2-dimethoxy-2-phenylacetophenone (DMPA), is cleaved into free radicals which begin the polymerization reaction. The free radical from the initiator then breaks a nearby double bond, creating a new covalent bond to the nearby molecule and propagating the radical further along the newly-forming chain. The propagation step involves the newly propagated radical attacking other nearby double bonds in succession, and termination involves various pairs of radicals interacting with each other to cause mutual extinction by either coupling, where two small chains meet up to become one larger chain, or disproportionation, resulting in the two smaller chains remaining separate and in the regeneration of a double bond. Free radical photopolymerization is popular because of its relatively low energy requirements, ability to be performed at ambient temperatures, and rapid speed [45-55].

1.3.2. Shape Memory Materials

It is commonly held that the first discovery of a "shape memory" process was made by Chang and Read in 1951 [56] during their investigation of a diffusionless phase transformation in a gold-cadmium alloy. Ten years after the discovery of Chang and

Read, a series of investigations regarding nickel-titanium alloys for naval applications by Buehler and Wiley [57] at the Naval Ordnance Laboratory (NOL) revealed that these NiTi alloys also exhibited the same type of diffusionless phase transformation; in honor of the initial investigations of this material system, an alloy of this type is often called NiTiNOL. This particular transformation behavior gave the material a "shape memory" effect, though the commercial and academic implications of their discovery did not begin to be recognized until years later [58].

Though the mechanism for the shape memory effect differs greatly from the metallic alloys, a similar deformation recovery behavior has since been shown in various polymer materials [59-65]. Regardless of the polymerization process, a polymer that undergoes a mechanical glass transition, where the modulus of the material drops by several orders of magnitude once over a threshold temperature range, can exhibit what is called the shape memory effect. Essentially, this behavior means that the material can be deformed from the initial state when soft and compliant, cooled while constrained, stored in the "frozen" state indefinitely, and then recovered to the initial state upon reheating. This is shown schematically in Figure 1.1.

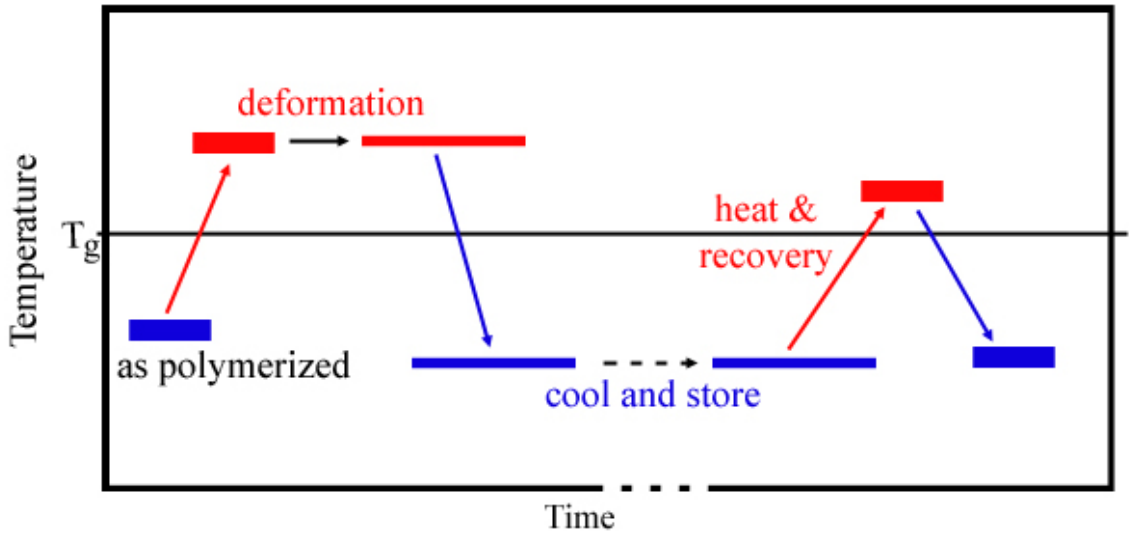

Figure 1.1. Schematic of the shape memory effect.

Classically, a polymer is classified as a shape memory polymer only when the glass transition temperature (T_g) is superambient and is glassy at ambient conditions, though this is not strictly a requirement. The shape memory effect in polymers is often visualized as an "entropic spring." When synthesized, the polymer is in an equilibrium state with the chains in a relaxed conformation such that entropy is maximized for the given conditions. As the polymer is stretched and deformed, the chains begin to align and become ordered; the entropy of the system is reduced. When the polymer is constrained and cooled, the chains are locked in place and the system is considered to be in a metastable state because the chains will remain deformed indefinitely. Once the polymer is heated, however, the "locking" of the chains releases - the chains become mobile and return to their initial conformation, again maximizing the entropy of the system.

1.3.3. (Meth)acrylates

For the better part of a century, (meth)acrylates (Figure 1.2) have formed a versatile class of polymers that play a major role in military and commercial products, from airplane canopies [66-69] and vehicle periscopes [70, 71] to optical storage media [72, 73], speakers [74], contact lenses [75], trophies [76], paints [77, 78], coatings [79], and adhesives [80-83], as well as in industrial and academic research.

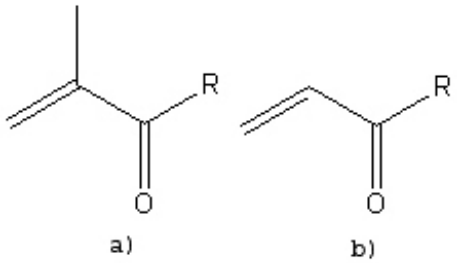

Figure 1.2. Chemical structure of (a) a methacrylate and (b) an acrylate.

They are popular because of their relatively low cost, ready availability, rapid polymerization kinetics, optical clarity, toughness, the broad range of achievable properties [84], and the relative ease of monomer synthesis and polymer manufacture and processing. (Meth)acrylates are popular materials for biomedical engineering because of their potential biocompatibility [64, 85-87], the ability to photopolymerize them *in situ* [88, 89], and the ability to tune the mechanical and degradative properties [85, 86, 90-92] of the network.

Several recent studies have illuminated the capabilities of (meth)acrylate systems which make them highly favorable for shape memory applications. The structure of

(meth)acrylate polymers can vary from a thermoplastic to a thermoset, depending on the concentration and structure of the monomers added [40-44]. A copolymer of purely monofunctional monomers results in a thermoplastic by definition, while the addition of di- or higher-functionality monomers results in thermosets ranging in behavior from lightly-crosslinked elastomers to highly-crosslinked, three-dimensional networks. More importantly, within both classes of material, it is possible to tune the glass transition temperature (T_g) by careful selection of the monomer [65, 84]. Monomers with long chains occupying the R position (Figure 1.2) tend to exhibit lower glass transition temperatures than those with α-methyl groups or other bulky groups adjacent to the unsaturated bond in the monomer [84]. The large concentration of bulky groups close to the main chain serves as a large interacting steric hindrance, which raises the T_g of the material. Long, carbon-based chains do not have as noticeable an effect due to their greater flexibility. The T_g of polymer networks is affected by both monomer chemistry and relative concentration; the crosslinking effect raises T_g while the copolymer effect can raise or lower T_g [93]. The crosslinking effect is a direct result of adding covalent links to the network, which are steric hindrances that hinder the macromolecular motion of the chains in the network. The copolymer effect, on the other hand, is a result of the actual chemical composition of the monomers included. Monomers with long flexible segments will reduce T_g, while monomers with short segments or bulky side groups in close proximity to the unsaturated bond will increase T_g, in the same way as discussed for thermoplastic (meth)acrylates. By carefully exploiting the interplay of these two effects, the T_g of (meth)acrylate networks can be adjusted.

Thermoset networks have an additional property, the rubbery modulus (E_r) or minimum storage modulus after the T_g, that is critical for shape memory applications and can be tuned *independently* from T_g [65]. E_r is controlled by the crosslink density (the inverse of the molecular weight between crosslinks) as proposed by Treloar [94]. Thus, polymers composed of difunctional (meth)acrylate monomers with higher molecular weight will, in general, have a lower E_r than those composed of lower molecular weight crosslinkers at equal concentrations. The effect is most pronounced at equal weight fraction, where the lower molecular weight crosslinker simply creates more crosslinks for an equivalent mass. It is less pronounced when compared by mole fraction except at very high mol% crosslinker, where the effects of the crosslinker are no longer diluted by the larger network behavior. Adjustment of this parameter can have important consequences. It has been found, for example, that network toughness (as determined by tensile testing) is affected by monomer chemistry when $E_r \leq 10$MPa, but is rather independent for higher values of E_r [84]. However, the exact contribution that various monomers make to some of the overall properties of the polymer is somewhat limited and not quantitatively predictable with current models [84]. Part of the difficulty in accurate property prediction lays in the inherent heterogeneity of (meth)acrylate networks. The heterogeneity stems from many factors, including self-cyclization (where a growing chain crosslinks with a pendant functional group from the main chain) [93, 95], the stochastic nature of polymerization and functional group distribution, and the basics of the (meth)acrylate polymerization reaction itself. In all (meth)acrylate networks, there are two types of chains – 1) main, pure-carbon backbone chains and 2) crosslink chains composed of the core of the multifunctional monomer. The inescapable presence of the

carbon-carbon backbone chains thereby limits the range of properties that the (meth)acrylate polymers can exhibit; the properties of the backbone chains, though not necessarily always dominant, still contribute to the behavior of the polymer. The selection and control of T_g and E_r are critical features in the design of shape memory devices. T_g, the deformation temperature, T_d, and the recovery temperature, T_r, all affect the recovery time of the polymer network [63, 65]. E_r is the main factor which controls the force of the recovery, though the aforementioned temperatures also have some contribution.

1.3.4. Thiol-enes

The thiol-ene (Figure 1.3) reaction was first suggested by the German chemist Posner in 1905 [96], but academic interest in this potential polymerization reaction remained relatively muted, especially as compared to (meth)acrylate polymerization, until the last two decades.

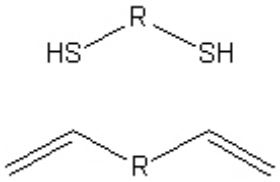

Figure 1.3. Chemical structure of (top) a dithiol and (bottom) a diene.

Interest in the thiol-ene reaction mechanism increased as distinct advantages over (meth)acrylate polymerization were discovered. Various researchers have shown that, unlike (meth)acrylates, thiol-ene reactions do not exhibit oxygen inhibition [10, 26, 34,

97, 98] and show reduced shrinkage [16, 28, 30, 99], while retaining high optical clarity. Additionally, due to the alternating nature of the reaction steps, thiol-ene polymers tend to be more homogeneous than (meth)acrylate polymers [33]. Moreover, the thiol-ene reaction is the only known free-radical addition reaction in which various chemical groups (e.g. phenolic rings, ethylene glycol groups, ester groups) can be incorporated into the main chain backbones, potentially allowing for a greater amount of property variation than is possible with pure (meth)acrylates. The polymer is no longer restricted by the presence of pure carbon-carbon chains, though these can be included if needed.

The thiol-ene free radical addition polymerization reaction, first proposed by Kharasch and coworkers in 1938 (steps 1-4) [100], is shown in Figure 1.4, assuming the –ene cannot homopolymerize:

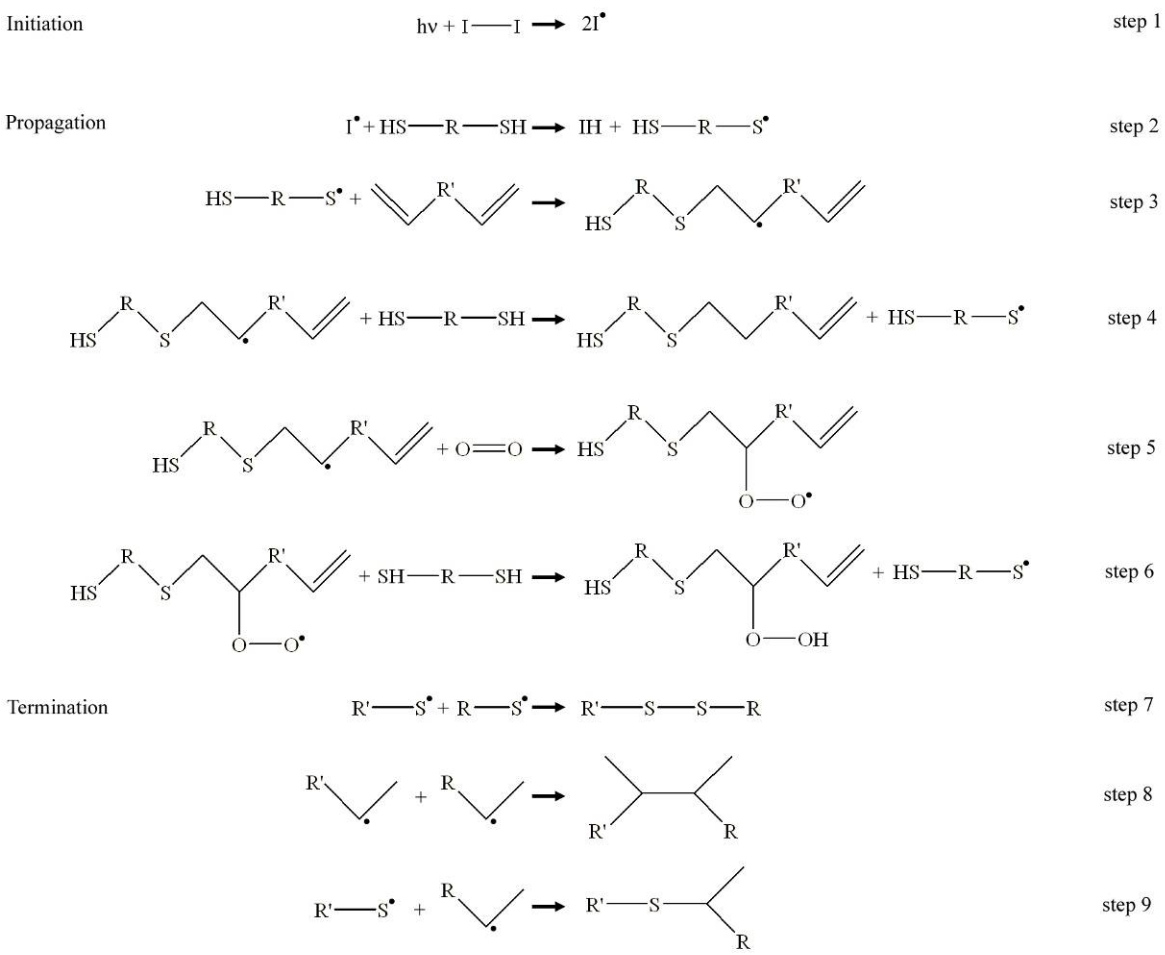

Figure 1.4. The thiol-ene reaction scheme.

Termination is generally thought to occur by radical recombination [2], as seen in steps 7-9. Steps 5 and 6 shows how inhibition by oxygen is avoided in this reaction – the peroxy radical still shows significant affinity for hydrogen abstraction from the thiol group, propagating the radical and allowing the reaction to continue. Note that, unlike (meth)acrylate polymerization where monofunctional monomers form linear chains, in order to form a polymer from the thiol-ene mechanism, the thiol and –ene must both be at least difunctional. Reaction of purely difunctional monomers results in a linear polymer system (i.e. a thermoplastic), while the inclusion of monomers with higher functionality

results in crosslinked network polymers, or thermosets. Monofunctional monomers simply act as chain terminators. To achieve full monomer conversion, a stoichiometric ratio of thiol and –ene functional groups is necessary. Note, too, that acrylates can be incorporated into the thiol-ene system because the acrylate group contains pendant unsaturated carbons. These, too, must be difunctional in order to avoid premature chain termination, but acrylates can homopolymerize, adding another step to the above reaction scheme. This added step increases the complication of both the kinetics, because the –ene and acrylate compete for thiyl radicals, and the network structure, since (meth)acrylate carbon-centered radicals can abstract a hydrogen from a thiol in the normal fashion or it can homopolymerize.

Some of the most comprehensive studies [17, 18, 101-110] on the photopolymerization of thiol-enes determined how various neighboring groups to both the –ene and the thiol affect their reactivities [10, 19]. It was found that an –ene with a neighboring vinyl ether is much more reactive than one with an allylic structure, which itself is more reactive towards hydrogen abstraction from a thiol (step 4, above) than a plain alkene [10]. Also, methacrylates are less reactive than acrylates due to the α–methyl group. The most reactive thiol type is mercaptopropionate esters followed by mercaptoacetates, and the least reactive type is alkane thiols [19]. Following in the footsteps of these studies, there are a number of studies which investigate the reaction using a variety of techniques. These techniques include modeling of the reaction [3, 4, 20, 22, 24], real time Fourier transfer infrared (RT-FTIR) spectroscopy which monitors the conversion of the groups as the sample is irradiated with ultraviolet light [1, 2, 4, 15, 16, 21], photo differential scanning calorimetry (photoDSC) which tracks the heat evolved during the

polymerization reaction as the sample is irradiated [8, 9], and rheology [1, 31, 32]. Some researchers have even investigated the unique ability of thiols to radicalize without photoinitiators [5], creating polymers without potential contaminants. Fewer studies have elucidated the mechanical properties of thiol-ene and thiol-ene/acrylate materials [29, 33, 34, 36, 111]. A rigorous process-to-thermomechanical property study of thiol-ene/acrylates was performed by the Hoyle group [37], who studied the effect of acrylate structure on the properties of various ternary copolymers composed of one trithiol, one tri-ene, and one of a selection of (meth)acrylates. However, the majority of the studies typically analyze one or two mechanical properties at most, generally with DMA. But since the thermomechanical properties of a material are a critical parameter in the design of a device for any application, a fuller understanding of the total behavior of thiol-ene polymers is necessary.

1.4. Testing and Evaluation Methods

1.4.1. Nanoindentation

Nanoindentation is a relatively new method for experimentally determining the mechanical properties of a small volume of material [112, 113]. This method is similar to standard hardness/ penetration tests, since a sharp or blunt tip is forced into the sample material. However, nanoindentation differs from typical macroscopic indentations in a critical way - the force and tip penetration depth are monitored during the experiment to obtain material properties, rather than by examining the residual impression left by the indentation tip after the indentation is concluded. For this reason, nanoindentation is often referred to as depth-sensing-indentation (DSI). Nanoindentation has been used to

measure the mechanical characteristics of materials ranging from bulk and nanoscale metals [112-118] to polymers [119-123]. Due to the small scale of the indenter tip itself and the extreme force and displacement resolution of the sensors, nanoindentation is uniquely suited to analyze small volumes of bulk materials or to analyze thin films or other materials with dimensions on the order of micrometers or nanometers, such as nanowires, thin films, and two-photon stereolithography polymer structures.

1.4.2. Dynamic Mechanical Analysis

Dynamic mechanical analysis (DMA) is a method used to determine the thermomechanical behavior of a polymer sample over a range of temperatures and/or frequencies. Essentially, the sample is deformed in a sinusoidal fashion until the limiting strain (or stress) is reached. A DMA machine records the applied strain (or stress) and resultant stress (or strain) as a function of time. Given that polymers are viscoelastic, they can be modeled as some combination of a spring and a dashpot, and there will be some phase lag, δ, between the two signals, as seen in Figure 1.5.

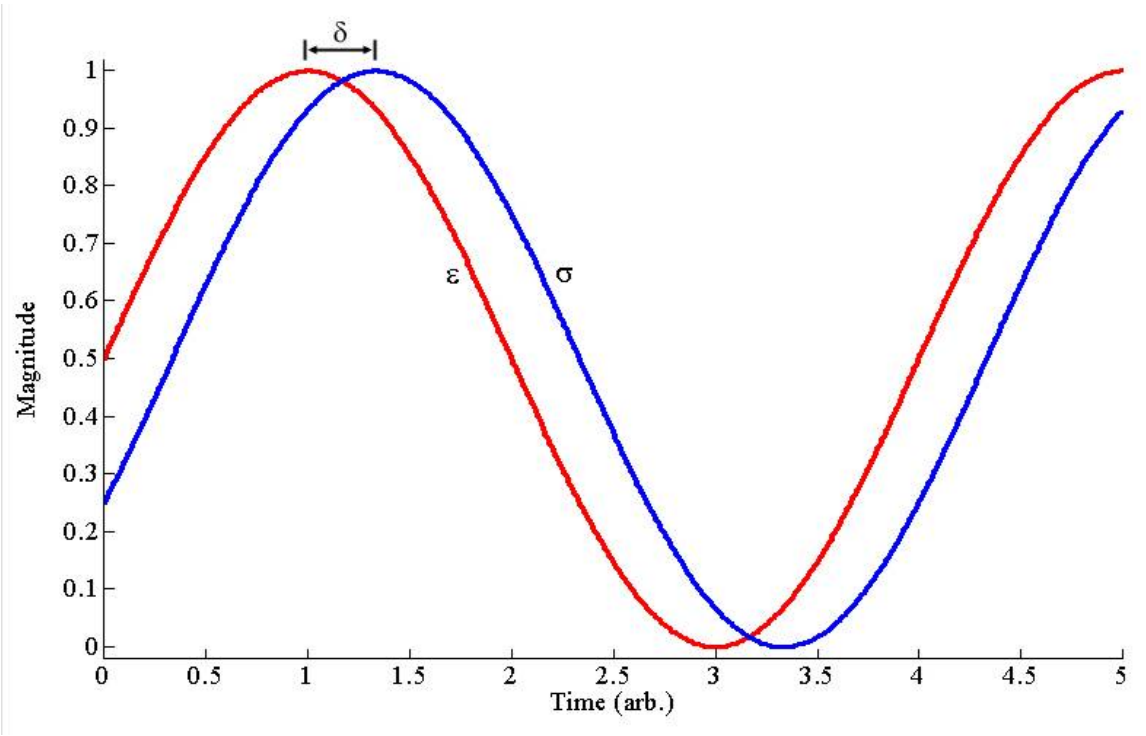

Figure 1.5. Example strain and stress data of viscoelastic material.

Assuming the applied strain is described by:

$$\varepsilon = \varepsilon_0 \sin(\omega t) \tag{1.1}$$

where ε_0 is the arbitrary amplitude, ω is the oscillation frequency, and t is time, then the stress in the spring is described by:

$$\sigma = \sigma_0 \sin(\omega t) \tag{1.2}$$

where σ_0 is the amplitude. Note that the spring stress is in phase with the strain because it is perfectly elastic. Given that deformation values are kept in the linear stress-strain region of the material, the Hooke's law relation states

$$\sigma = E\varepsilon \tag{1.3}$$

so Equation 1.2 can be rewritten

$$\sigma = E\varepsilon_0 \sin(\omega t) \tag{1.4}$$

The stress-strain relationship for a dashpot is

$$\sigma = \eta\dot{\varepsilon} \tag{1.5}$$

where η is the dynamic viscosity and $\dot{\varepsilon}$ is the first time derivative of the strain, called the strain rate. Thus, Equation 1.5 can be written

$$\sigma = \eta\omega\varepsilon_0 \cos(\omega t) = \eta\omega\varepsilon_0 \sin\left(\omega t + \frac{\pi}{2}\right) \tag{1.6}$$

Here we note that the dashpot maintains the same frequency as the applied deformation but with a 90º phase lag. The term ηω can be thought of as a sort of "viscous modulus," since the equation bears striking similarity to the standard Hookean law and the units of modulus and ηω are the same. So, given any real viscoelastic material, the behavior must be described by some combination of the behaviors of two extremes of the model, the spring and the dashpot. Thus, with a phase lag of δ, the response of the material to deformation can be written

$$\sigma = \sigma_0 \sin(\omega t + \delta) \tag{1.7}$$

which can be expanded using the trigonometric equivalence for a summed angle within a sine function into

$$\sigma = E\varepsilon_0\left[\sin(\omega t)\cos(\delta) + \cos(\omega t)\sin(\delta)\right] \tag{1.8}$$

When comparing this equation to the responses of the spring and the dashpot, it can be seen that Equation 1.8 can be simplified to

$$\sigma = E'\varepsilon_0 \sin(\omega t) + E''\varepsilon_0 \cos(\omega t) \tag{1.9}$$

so that the contributions of the spring and dashpot behavior become obvious. The variable E' is called the storage modulus and it describes the elastic portion of the material's response, and can be written

$$E' = E\cos(\delta) \tag{1.10}$$

while E" is termed the loss modulus and it describes the viscous portion of the material's response, and is written as

$$E'' = E\sin(\delta) \tag{1.11}$$

The ratio of these two moduli is termed the loss tangent or simply tan(δ) and is defined as

$$\tan(\delta) = \frac{\sin(\delta)}{\cos(\delta)} = \frac{E'''}{E'} \tag{1.12}$$

The storage modulus is often used to describe the thermomechanical behavior of a polymer over a range of temperatures (such as defining E_r), while the peak of the loss tangent is often used to define T_g [2, 33, 63, 65, 84, 93, 124].

1.4.3. Photo Differential Scanning Calorimetry

Typical differential scanning calorimetry (DSC) is used to determine phase changes, crystallization, melting, and T_g in various materials by tracking the mass-specific heat flow (i.e. W/g) over given temperature range in an inert atmosphere. The DSC machine does this by measuring the heat flow into a sample in a pan while using the heat flow into an empty pan to remove the contribution of the pan material to the overall heat flow and to extract the heat flow to (or from) the sample only. PhotoDSC, on the other hand, tracks the heat flow out of a monomer during exposure to an ultraviolet source which causes the material to polymerize. It determines the heat flow from only the sample by subtracting the contribution of the incoming light which is concurrently irradiating an empty reference location.

Typically PhotoDSC studies are performed under isothermal conditions in an inert atmosphere so that various complicating effects, such as thermally-driven autoacceleration and oxygen inhibition, are negligible. Variables that can be controlled and studied include irradiation intensity, the temperature for the reaction, and the ambient atmosphere composition. Given the temporal exothermic characteristics of the polymerization alone, it is possible to determine total heat evolved by the reaction, as well as a normalized conversion rate and is useful for comparing various materials to one another in a relative sense. If more specific information such as the monomer

composition, molecular weight, and the theoretical heat of conversion of relevant bonds (i.e. C=C to C-C) is available, it is possible to determine the absolute bond conversion as a function of time and the absolute rate of polymerization.

1.4.4. Mechanical Testing

Mechanical testing in tensile mode is used to determine the stress-strain behavior of the bulk-fabricated polymers. The stress-strain behavior allows for the extraction of critical materials properties such as Young's modulus, stress and strain at failure, overall behavior of the material (brittle vs. ductile), and toughness. A polymer in the glassy state acts brittle, while a polymer in the rubbery state acts ductile as a general rule. It is often more instructive to compare, for example, the behavior of polymers in the rubbery state rather than to compare the behavior of the polymers at the same absolute temperature. The macrostate of the polymer has a very strong effect and will overshadow the other variables which are often of more interest, such as network structure. Therefore, the polymers herein were all tested at their respective T_g's in order to facilitate behavioral comparisons; testing at T_g ensures that the polymers are in a similar viscoelastic macrostate.

1.4.5. Fourier Transform Infrared Spectroscopy

In Fourier transform infrared spectroscopy (FTIR), a thin sample of material is placed between windows which are invisible in the infrared range, such as KBr or sapphire, and subjected to a beam of radiation. The amount of radiation transmitted through the sample, compared to what is incident on the sample, is recorded on the other side as a

function of wavenumber (inverse wavenumber) and compiled into a chart called a spectrum. Different chemical groups absorb infrared radiation at different wavelengths due to the unique interaction of those wavelengths with the atomic vibrations of the particular bond. The chemical groups can then be identified by their particular infrared "fingerprint" against a known set of exemplars. Even in the case of some signature overlap, the spectra of the various groups can be deconvoluted [15] because of *a priori* knowledge of the signatures of the chemical groups. The amount of radiation absorbed is proportional to the amount of groups the radiation encounters and interacts with as it traverses the thickness of the sample. It is therefore affected by both sample thickness and the concentration of bonds present in the sample. Therefore, if the sample thickness is known, then the number of moles of bonds can be determined based on the % transmittance at appropriate wavenumbers. However, samples which are too thick will absorb so much radiation that the detector is unable to obtain a spectrum of the material in question, so thin samples are used to prevent absorption saturation, which can eliminate important information about relative amounts of different groups.

FTIR is capable of scanning both solid and liquid samples, which is useful for performing "real-time" experiments where spectra are rapidly recorded at discrete points in time as a liquid monomer is polymerized under the influence of ultraviolet radiation. Using the data from "real-time" FTIR allows for highly detailed information about polymerization rates and conversion percentages, delineated by chemical group. As such, an FTIR is better able to track the polymerization of various groups within a sample than the PhotoDSC is. The PhotoDSC tracks one signal (exothermic heat flow) that describes all of the reactions taking place, but FTIR is capable of tracking the disappearance and

appearance of multiple specific chemical groups concurrently. Alternatively, spectra recorded both before and after polymerization allow overall conversion to be calculated for particular functional groups (which is still more detailed than PhotoDSC), but detailed conversion rates cannot be determined since intermediate data are missing. Final conversion plays an important role in explaining certain polymer behavior. For example, unconverted or residual monomer can often act as a plasticizer, reducing the T_g and E_r of the polymer as compared to a polymer with fully converted groups.

1.4.6. Microscopy

Both optical and electron microscopy were employed in order to qualify and quantify the pattern transfer fidelity of polymer features created with photolithography. Selected thiol-ene mixtures with median thermomechanical properties were photopatterned. The amount of shrinkage of the thiol-ene polymer systems can be quantified as compared to thermo-mechanically equivalent (meth)acrylate systems. Shapes, such as squares and circles, can be photopatterned in these various systems and the resultant dimensions measured via microscopy. The final dimensions of the polymer shapes can be used as a quantitative measure, while shape can be used as a qualitative measure (i.e. does the square still look square, or are the corners extremely rounded?), of the ability of the polymer to act as a high-fidelity photopolymer.

1.4.7. Sol-Fraction

Sol-fraction testing is a method used to determine the amount of soluble material present in a sample. A sample of polymer is massed and placed in an appropriate solvent in

which the monomer is soluble. After a portion of time (generally 48+ hours), the sample is dried in an oven, and allowed to acclimate to room conditions again before a final mass is taken. The difference between final mass and initial mass, normalized by the initial mass, is the sol-fraction percentage of the material. Additionally, extractable, non-participating impurities present in the monomer contribute to the sol fraction of a polymer. Large sol-fractions can indicate high impurity levels or low conversion coupled with low network connectivity, since more material (in monomer and oligomer form) is soluble and can be readily extracted by the solvent.

1.5. Purpose and Scope of Research

The rationale for this research stems from the interest in thiol-ene polymers due to the various advantages they posses over acrylates, especially the reduced shrinkage that has been reported. Given the current state of knowledge in the field, the kinetics of thiol-ene polymerization are well understood and many models have been developed which can accurately describe the reaction. But there is still a lack of a complete characterization of the thermo-mechanical behavior of thiol-ene and thiol-ene acrylate polymers. Because of their unique polymerization behavior, thiol-ene polymer mixtures have the potential to eliminate the choice that researchers are forced to make in photolithography – high pattern transfer fidelity vs. controlled polymer properties – and expand the range of properties that lithographically-produced polymers can exhibit.

Additionally, TPS has emerged as a powerful and versatile technique for creating polymer structures on the order of micrometer scale. However, before any devices can be properly designed for any particular mechanical role either in biomedical or MEMS

devices, the properties of the resultant polymers must be quantitatively defined. Establishing the link between the processing parameters used in TPS and the resultant properties of current polymers is a key step in expanding the use of TPS structures in functional applications. Thus, the objectives for this research have been established to address these current limitations:

1. Quantify the mechanical properties of TPS structures and understand the process-property map (as compared to bulk)

2. Understand the link between process, structure, and properties of thiol-ene/acrylate polymers for bulk behavior (e.g. shape memory) and for microscale fabrication

3. Test thiol-ene/acrylate copolymers in standard photolithographic techniques and evaluate whether soft (low elastic modulus) and rubbery polymer structures can be made with this process and material combination.

It is anticipated that the research proposed herein will have a significant impact on the understanding of thiol-ene and thiol-ene/acrylate network behavior. Additionally, the research is projected to have a large impact on polymer photolithography and MEMS by providing the first quantitative mechanical characterization of TPS-produced materials and by introducing a new class of polymer that will allow for property control in photolithography without sacrificing pattern replication accuracy. Finally, based on results from the work described herein, recommendations on future paths for research will be made.

CHAPTER 2. NANOINDENTATION OF MICROSCALE POLYMER STRUCTURES FABRICATED VIA TWO-PHOTON STEREOLITHOGRAPHY

2.1. Summary

The research started with defining the mechanical characteristics, in both the bulk form and the photopatterned form, of an exemplar material used in photolithography. Two-photon stereolithography has emerged as a novel method for fabricating true three-dimensional, submicrometer polymer structures via photopolymerization. However, characterization of the structures has been limited to microscopy and some chemical analysis. A mechanical evaluation of these structures has not been performed in the open literature. In the current study, mechanical characterization via nanoindentation was performed on two-photon stereolithography-produced polymer structures over a range of processing parameters. The properties were compared to those of bulk-photopolymerized samples of the same material. Dynamic mechanical analysis was used to characterize the thermomechanics of the bulk sample at the macroscale and to determine the polymer's state under ambient conditions. A process parameter-to-property map was created and it was found that both stage translation speed and intensity have a strong effect on the mechanical properties, with intensity exhibiting a stronger effect on both modulus and indentation hardness. It was also determined that two-photon stereolithography was capable of creating polymer structures that were stiffer and harder than those of bulk-processed polymer.

2.2. Introduction

2.2.1. Two-Photon Stereolithography

Two-photon stereolithography (TPS) [125, 126] is a polymerization method developed in the last decade which allows for the precise control of photopolymerization in three dimensions at the sub-micrometer level [55, 127-152]. In typical laser lithography, free-radical initiation depends on the integration of intensity which is essentially uniform for the light cone, and so the entire volume of the cone is polymerized. Traces in laser lithography therefore create 2D layers whose thickness is controlled by the monomer liquid thickness; so-called 2½D (or quasi-3D) structures are created by polymerizing multiple layers one on top of the other. In TPS, the initiator [127, 128, 133, 141, 153, 154] requires the energy of two photons to reach the excited state, then radicalize, and the absorbance is proportional to the squared intensity (or higher) of the light [125, 129], so polymer forms only in the very small volume surrounding the focal point of the laser where the density of photons is great enough to generate free radicals from the initiator. The exact chemistry and absorption characteristics of this photoinitiator and associated materials are certainly key to the accuracy of the technique and are the subject of substantial recent and current research [127, 128, 133, 138, 141, 145, 154-158]. True three-dimensional, sub-micrometer precise, geometrically complex polymer structures [55, 128, 137] can be fabricated by scanning the laser focal point in three dimensions, performing progressive volumetric photopolymerization of liquid monomer solutions. Acrylate resins are commonly used in two-photon processing due to their high rates of photopolymerization [55].

In order for TPS-produced polymer structures to act in any mechanically functional role, especially when integrated with silicon-based MEMS or in biomedical devices, the mechanical properties of the material must be established. However, there is a dearth of mechanical analysis of the resultant structures in the current literature, due to both the small scale of the polymers and the relative youth of the process. Thus far, characterization has been limited to qualitative estimations based on visual observations of the structural integrity of the part. Establishing the link between the processing parameters used in TPS and the resultant properties of the polymers is a key step in expanding the use of TPS materials.

2.2.2. Nanoindentation

Nanoindentation is a method for determining the mechanical properties of materials at the nanoscale [112, 113]. The penetration of the tip into the sample material, as well as the force required to obtain the penetration, are recorded throughout the loading and unloading portion of an indentation. The load-depth response, or compliance curve, of a material defines its properties. Nanoindentation relies on contact mechanics first developed by Hertz [159, 160] and by Boussinesq in order to extract the material properties from a compliance curve.

2.2.2.1. Contact Mechanics

In elastic contact mechanics, the tip of the indenter comes into contact with the surface of the specimen and penetrates the surface, deforming it in a well-studied fashion. Though initially developed by Love for the penetrations of a rigid circular [161] and conical [162]

punch into an elastic half-space, the mechanics have been adapted to include compliant indenters and also expanded by Sneddon to include penetration by an axisymmetric punch of arbitrary shape [163] and further by King [164] to include quadrilateral and triangular punches via the introduction of a geometric correction factor. For the contact between a non-rigid indenter and an elastic half-space, the indenter can be modeled as perfectly rigid by introducing a "reduced" modulus for the elastic half-space, given by:

$$\frac{1}{E^*} = \frac{(1-\nu^2)}{E} + \frac{(1-\nu_i^2)}{E_i} \tag{2.1}$$

where E^* is the reduced modulus, and E and υ are the elastic modulus and Poisson's ratio of the given material, with the *i* subscript denoting the properties of the indenter and no subscript denoting the properties of the elastic half-space. Note that the Poisson's ratio for the indented material must be assumed, and this can introduce errors. The load required to drive a conical indenter into this elastic space is given by [165]:

$$P = \frac{2E^* \tan\alpha}{\pi} h_t^2 \tag{2.2}$$

where P is the load on the punch, α is the cone semi-angle, and h_t is the depth of penetration of the indenter tip. A schematic of the important quantities for a cone indenting an elastic half-space can be found in Figure 2.1.

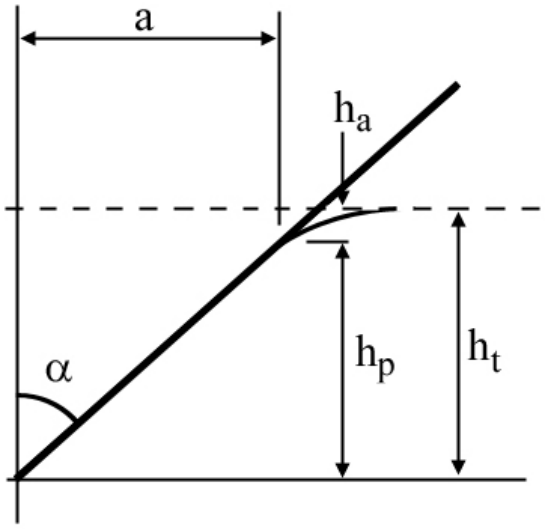

Figure 2.1. Geometry of elastic half-space and conical indenter in cut-away view. Dashed line is original specimen free surface, thick solid line is deformed specimen surface, and thick solid line is the cone edge.

Other important indentation parameters that appear in Figure 2.1 are: a, the radius of contact, h_p, the actual depth of penetration, and h_a, the distance from the specimen free surface to the circle of contact. The radius of the circle of contact, a, for a cone is related to the penetration depth, h_p, by:

$$a = h_p \tan\alpha \tag{2.3}$$

The actual penetration depth, h_p, can be determined by combination of the following two equations [113, 163], noting that h_t is the measured indentation depth:

$$h_t = h_a + h_p \tag{2.4}$$

$$h_a = \varepsilon \frac{P}{S} \tag{2.5}$$

where ε is a geometrical factor related to the indenter geometry (ε=1 for flat punch, ε=0.75 for a parabaloid of revolution, or ε=0.72 for a cone), P is the applied load and S is the measured stiffness (initial slope of unloading curve). While the above analysis was developed for an axisymmetric indentation cone, it can be applied non-axisymmetric indenter tips (such as the triangular Berkovich tip) due to geometric similarities by introducing geometry and intercept correction factors as mentioned earlier.

2.2.2.2. Nanoindentation Description and Procedure

A typical nanoindentation test consists of a surface-find segment, a loading phase, a hold segment (optional), and an unloading phase. The surface-find segment essentially consists of initiating an indentation with high force sensitivity, and once the indenter senses a force above a certain threshold, the indenter tip is considered to be in contact with the specimen surface. Figure 2.2 shows a schematic of results from a representative nanoindentation test, displaying load (P) versus depth (h). The important features of the graph are that the loading curve (upper portion) shows elastic-plastic deformation, while the unloading portion of the curve (lower right-hand side) exhibits purely elastic deformation in reverse, to a final residual depth of h_r. The reason that the lower portion of the curve is not a straight line (denoted by dP/dh) is because the contact area is constantly changing during load removal, due to the geometry of the indenter tip. The distance h_e on the graph is the elastic recovery depth of the material. Note that h_p on the graph can be determined by taking the initial slope of the unloading curve – called *contact stiffness, S* (i.e. dP/dh) – and extrapolating it from peak load, P_t, to zero load. Also, note that h_t is the total penetration depth at peak load.

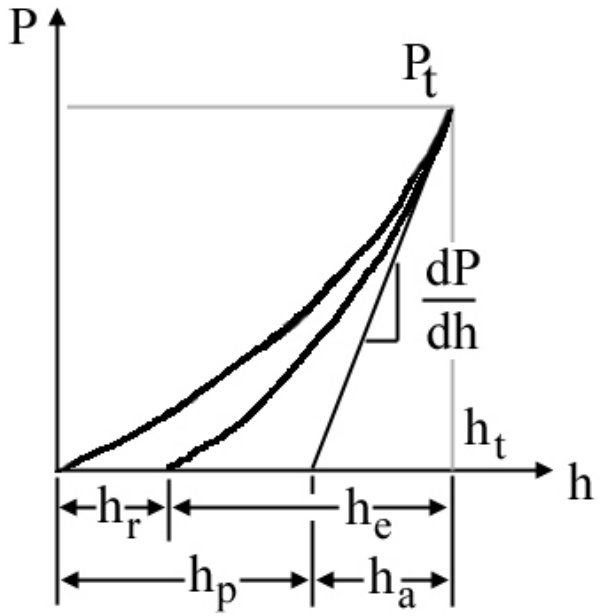

Figure 2.2. Typical load vs. depth indentation compliance curve. Evident is elastic-plastic loading and elastic unloading. P is load and h is penetration depth.

Variations on this simple cycle can be added for various investigations. Adding a small sinusoidal displacement to the overall displacement of the tip (a procedure called Continuous Stiffness Measurement, or CSM, by MTS Systems, Inc.) during loading can reveal both material properties as a function of depth and viscoelastic behavior in polymers [166, 167]. Polymeric viscoelastic behavior includes material storage effects, which are evident in the damping which occurs between applied load and resultant displacement. The CSM technique is also a much more accurate way to find the specimen free surface, since the harmonic stiffness undergoes a sharp and dramatic change at surface contact [112], whereas the force change is more gradual and it is harder to define the surface by conventional methods. Partial unloading during the load sequence can also yield depth-sensitive material property information, but the CSM technique is a more advanced method for attaining these results. Holding the indenter tip

at the maximum force and recording the resulting displacement change as a function of time can reveal the effects of creep in polymeric [168, 169] and metallic systems. Adding a small hold segment to the unloading portion of the cycle at low load can allow later data compensation for thermal drift in the material/indenter. Other types of tests that a properly equipped nanoindenter can run include ramp-loading scratch tests to determine film-substrate adhesion as well as atomic force microscope (AFM)-like surface feature measurements.

There are many different tips available for nanoindentation, such as Berkovich – an equilateral three-sided pyramid, Vickers – an "equilateral" four-sided pyramid, Knoop – a four-sided pyramid with long and short axes, cube-corner, spherical, and conical indenters. Different tips are used for different studies. The Berkovich tip is perhaps the most common, because it is easiest to create a sharp point on a three-sided pyramid (whereas a line-point is almost inevitable in a four-sided Vickers tip). On the other hand, the Knoop indenter has the unique property that elastic material recovery occurs mostly on the short axis, while the long axis remains nearly unrecovered during the unloading process. Researchers can use this unique property to determine anisotropic elastic properties of indented materials.

A critical parameter for nanoindentation testing is the projected area-to-depth ratio of the indenter tip. Vickers and modified Berkovich indenters have the same ratio by design. Post processing uses this "area function" ($A(h) = 24.5h^2$ for ideal Berkovich, Vickers, and equivalent cone indenters) to compute the mean contact pressure (or indentation hardness, $H=P_t/A$) as a function of load and depth. However, before any investigations

can be performed, the tip shape must be calibrated. Typically, the tip is indented into a known reference material (i.e. fused silica SiO_2, nominal modulus E=72 GPa) a number of times to different depths, and then a tip area function is computed. The area function typically follows the form:

$$A = C_1 h_p^2 + C_2 h_p + C_3 h_p^{\frac{1}{2}} + C_4 h_p^{\frac{1}{4}} + \ldots + C_8 h_p^{\frac{1}{128}} \tag{2.6}$$

where h_p is the depth of penetration from the circle of contact, as before, and C_1-C_8 are constants determined from the indentations of the calibration sample. Following the approach of Oliver and Pharr [112, 113], once the material is indented and the compliance curve is obtained, the modulus of the material can be determined from the formula:

$$E^* = \left.\frac{dP}{dh}\right|_{h_{\max}, P_{\max}} \frac{1}{2\beta}\sqrt{\frac{\pi}{A}} \tag{2.7}$$

along with Equation 2.1. The geometry correction factor, β=1.034 for Berkovich indenters based on finite element simulations of flat ended punches with triangular cross-sections [164], accounts for the lack of an axisymmetric geometry.

2.2.2.3. Importance of Nanoindentation

Nanoindentation is an important technique because it allows investigators to examine materials in ways that were impossible before. Due to the small indentation scales, investigators can now probe the response of near-surface molecules, which may have

different responses than bulk molecules due to free-surface energy and other surface interaction contributions. Even the response of small volumes of material at high resolution can be compared to the bulk material response obtained with normal indentation techniques. Also, researchers can exploit this particular aspect of nanoindentation to characterize thin films. Thin films are typically on the order of hundreds of nanometers to hundreds of micrometers thick, so nanoindentation is particularly suited to determining the properties of these films without including properties of the substrate. In addition to testing the material properties of the films themselves, nanoindenters can be instrumented to perform force-ramp nano-scratch tests, which allows investigators to determine the quality of adhesion between the film and the substrate. Furthermore, the small size of the indenter tip itself allows for more testing flexibility. Researchers can test the properties of single grains in a metal alloy, or even micron-scale structures [170, 171] and individual components of MEMS devices. Nanoindentation is also particularly suited to research for this small-scale aspect; prototype materials fabricated in laboratories are often created in small quantities at great expense, so the smaller material volumes required for nanoindentation evaluation can be a great fiduciary benefit over the larger volumes required for typical indentations.

A feature of nanoindentation that is equally as important as testing at small depths and small scales is the fact that nanoindentation is a depth-sensing indentation. This allows for the introduction of new techniques such as CSM, which allows investigators to determine material properties as a function of depth; this depth-dependent measurement is not feasible using standard indentation techniques. CSM also allows researchers to evaluate viscoelastic material properties, which are especially critical in characterizing

polymer systems and structures. Finally, nanoindentation is more of a self-contained testing and evaluation technique, as the material properties are determined almost instantaneously. Nanoindentation does not rely on another step, such as optical examination for the determination of the size of the residual impression, to characterize the material in question. This can lead to a quicker iterative process as results are generated during the test, rather than after a second or third step.

2.2.2.4. Critical Technologies

2.2.2.4.1. MTS Nanoindenter XP®

Any nanoindenter is instrumented only to output raw force and displacement data. The majority of the material property determination occurs in post-processing of this raw data, based on the analysis methods described earlier. Here, the driving technology in the Nanoindenter XP® by MTS Systems, Inc. will be described in some detail to provide a basic understanding of the underlying mechanisms and measurement techniques of this particular indenter. Obtaining force and displacement at such small scales by this method is by no means unique; many other competing companies have invented variations on nanoindentation instrumentation to obtain data at such scales.

The very heart of the Nanoindenter XP® by MTS NanoSystems, Inc. is a device called the Nano Mechanical Actuating Transducer, or NMAT. A schematic view of the NMAT can be found in Figure 2.3, with the various components labeled and color-coded.

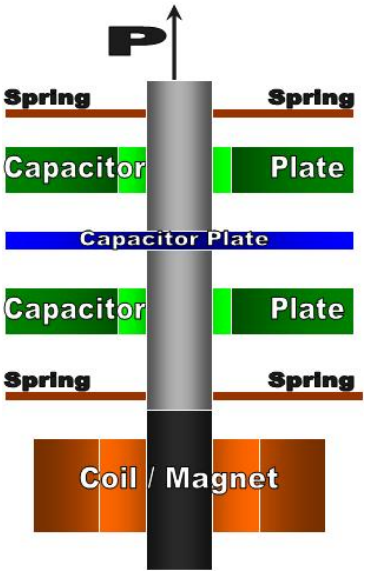

Figure 2.3. Side cut-away view of components of nanoindenter transducer.

The NMAT has two salient features which can be seen in the above figure, namely the capacitive displacement sensor and the coil/magnet assembly. The capacitive sensor consists of three plates, the two stationary outer ones (with holes for the indenter shaft) forming a sandwich for the third mobile plate, which is connected to the indenter shaft. The capacitive sensor is highly sensitive to plate separation changes and is the displacement sensor for the nanoindenter; it purportedly has a resolution of better than 0.01 nm, though the displacement noise floor for this is reported to be about 0.2 nm. This is a more accurate measure of the practical resolution of the machine, and is usually obtained under ideal laboratory conditions. In service, the NMAT is inverted from the images shown, and the "free end" of the shaft (where P, the load, is indicated in Figure 2.3) is connected to the indenter tip; the capacitive sandwich measures the displacement caused by the coil/magnet combination at the base of the NMAT. The coil and magnet combination at the base of the indenter shaft is connected to a high precision current source. The current from the source, which is constantly monitored by the software,

creates a magnetic field within the coil and provides a motive force for the magnetized end of the indenter shaft. Overall, this coil and magnet, along with the high-precision current source, provides a force resolution of 50 nN. The springs which are evident in Figure 3.1 are for supporting and guiding the indenter shaft. As such, the springs are designed to be thin and highly flexible in the axial travel direction, while they are stiff in the lateral/transverse direction to prevent undesirable and potentially damaging sideways motion of the indenter shaft. This device is not designed to measure or withstand torsion.

The NMAT can be run in several modes to achieve different testing methods. However, due to the construction of the NMAT device, the MTS Nanoindenter XP® is a force-resolved/ load-controlled instrument. The only mode which does not require feedback from the capacitive sensor is the standard indentation technique, in which the NMAT records the force induced by the magnetic coil and the resultant displacement. Also, holding the indenter tip at the maximum force and recording the resulting displacement for creep testing does not require feedback. One mode that requires feedback is the "displacement" version of the creep test. The tip is held at a constant displacement by the force-coil, which uses feedback information from the displacement sensor to maintain the tip position. The indenter then measures the force relaxation as a measure of creep behavior. Another method that requires feedback from the capacitive sensor includes the CSM/sinusoidal loading technique. The current source and coil need information from the displacement sensor in order to determine when to locally retract or extend the indenter tip. Finally, a standard method which requires feedback is the maximum displacement test, in which the condition for the end of the loading phase is when a certain depth is reached, as opposed to when a certain load is reached.

There is also a low-load accessory for the Nanoindenter XP® called the Dynamic Contact Module (DCM). Due to its high resonant frequency, low damping coefficient, and increased dynamic frequency, this module is less sensitive to environmental noise [165]. This allows for incredible theoretical displacement resolution of 0.0002 nm and a load resolution of 1 nN, which is appropriate for detecting surface forces on the atomic scale.

Typically, the noise level of the displacement sensor is controlled by the impedance of the transducer, and allows for much higher resolution than possible with strain gauges. Generally, the resolution is also limited by the thermal stability of the transducer elements themselves. Displacement transducers of comparable resolution have been patented by various companies, such as Hysitron [172, 173]. Other types of indenters (such as the CSIRO "UMIS®" [174]), which use high-quality linear variable differential transformers, report displacement resolutions of 0.03 nm (with a 0.05 nm noise floor) and force resolution of 500 nN (750 nN noise floor). By implementing an environmental chamber, which includes insulation against environmental and electromagnetic noise, thermal barriers, and vibration isolation tables, high-resolution data can be obtained in the laboratory. AFM users rely on similar safeguards to obtain their data.

2.2.2.4.2. Nanoindenter Tips

Many different companies produce nanoindenter tips. Typically, nanoindenter tips are made of diamond or sapphire, though they can be fabricated from quartz, silicone, tungsten, steel, and tungsten carbide. Though the fabrication methods (e.g. grinding) for the different types of materials and shapes (Berkovich, Vickers, spherical, etc.) varies, all nanoindenter tips must meet the requirements of the international calibration standard

ISO/IEC 17025.1 and the dimensions and angles must comply with the ISO 14577 (part 2) standard. This latter standard defines internationally accepted micro and nanoindenter tip tolerances and machine calibration, whereas the first part of the standard defines the acceptable procedures. For example, a unique method recently investigated [175, 176] for achieving AFM tip-like sharpness on a diamond nanoindenter tip is the focused ion beam milling technique. AFM imaging has been used to quantify the size and shape of nanoindenter tips (the area function), and the image data have been used as a comparison to standard area function calibration procedures, such as indenting a fused silica sample [177].

2.2.2.5. Error Sources

In nanoindentation errors can, in general, come from two places; there are sample/ material-related errors, which often result from the assumptions made in the nanoindentation analysis, and instrument-related errors. Instrument errors are often simply resolved by performing the proper calibrations before executing the experiments. However, based on discussions in the literature, some possible instrument errors have yet to be resolved in an acceptable fashion.

2.2.2.5.1. Sample-related

2.2.2.5.1.1. Pile-up

As seen in Figure 2.1, nanoindentation analysis assumes that the surface of the material responds in a typical elastic fashion, and deflects downwards with the indenter tip. However, it has been found by some investigators that in some rare cases that the

material actually climbs the indenter tip. This is termed "pile-up" and generally only occurs when the material has both a high E/σ_y and does not exhibit any work hardening [112]. Pile-up behavior will greatly change the actual area of contact of the indenter, and this will introduce major errors if it the normal assumption of a depressed surface is made. So far, researchers have had limited success in determining the proper way to account for pile-up in various materials [178].

2.2.2.5.1.2. Creep

Many polymer systems exhibit some form of creep, or force/displacement relaxation. Ignoring this behavior in the testing phase can lead to unexpected results in the data analysis phase. The contact stiffness, and therefore elastic modulus, is derived from the initial unloading data, which assumes that the contact area is roughly constant while the material elastically recovers part of its initial shape. However, in systems that exhibit creep, the material continues to deform for a short time even after the loading is reversed. This leads to a "nose" in the compliance curve [179], and can result in negative values for the contact stiffness. To combat this behavior, researchers typically include a hold segment in the experiment, where the indenter tip is held at a constant force for a period of time. Thus, the material has time to reach a quasi-equilibrated state where the viscous portion has relaxed so that when the tip is retracted, the material elastically recovers in the usual manner.

2.2.2.5.1.3. Surface Contact Uncertainty

Surface roughness, extreme sample compliance, and surface forces/adhesion can become sources of error in nanoindentation. In both cases, it becomes difficult to determine when exactly the indenter tip comes into contact with the actual surface. Large asperities can impact the indenter tip on a face long before the tip actually reaches the true nominal free surface of the specimen. Also, asperities increase the contact surface area of the indenter in much the same way as in pile-up behavior.

Very compliant materials pose a problem for nanoindenters from a resolution standpoint. Most nanoindenters rely on a change in force level to indicate contact with a material, and compliant materials may not provide a large enough resistance to the indenter tip for the indenter to recognize that contact has been achieved. The newer CSM technique changes the contact criterion to that of a harmonic stiffness change, and this can be a more accurate way to determine the initial contact with a complaint material. However, when establishing the experimental surface datum, both methods require some small penetration into the surface, and this initial surface penetration must be taken into account when performing subsequent experiments.

In some cases, materials may have surface forces or exhibit adhesion, and this causes errors because this material behavior departs from the Hertzian assumptions of nanoindentation. This in essence amounts to something like pile-up, but can also include additional forces and behaviors that would affect the compliance curve, as the retracting tip would actually "pull" the material back upwards, rather than simply allowing the material to elastically recover, per the usual.

2.2.2.5.1.4. Residual Stresses

The analysis procedures mentioned previously all assume that the material surface is initially free of stresses. Certain processing or material preparation techniques can leave residual stresses within an experimental sample, however. These stresses typically change the strain level at which material yield will occur. Some researchers, such as Roberts et al. [180] have determined ways to evaluate the residual stresses in materials using nanoindentation, though this is a specialized case and is not very common.

2.2.2.5.1.5. Poisson's Ratio: Error Propagation

Solving Equations 2.1. and 2.7 for the elastic modulus of the sample yields:

$$E = \frac{(1-\nu^2)}{\left[\frac{2\beta}{S}\sqrt{\frac{A}{\pi}} - \frac{(1-\nu_i^2)}{E_i}\right]} \tag{2.8}$$

where S = dP/dh (the contact stiffness), β is the geometric correction factor, A is the tip area, E_i is the indenter modulus of elasticity, υ_i is the indenter Poisson's ratio, and υ is the Poisson's ratio of the sample. Using standard root-sum-squares error propagation procedures to find the fractional uncertainty in E based on the uncertainty in the Poisson's ratio, we arrive at the equation

$$\frac{u_E}{E} = \sqrt{\left[\nu \frac{d(\ln E)}{d\nu}\right]^2 \left[\frac{u_\nu}{\nu}\right]^2} \tag{2.9}$$

where from Eqn. 2.8 we know that

$$\ln(E) = \ln(1-\nu^2) - \ln\left[\frac{2\beta}{S}\sqrt{\frac{A}{\pi}} - \frac{(1-\nu_i^2)}{E_i}\right] \tag{2.10}$$

The fractional uncertainty in E is then

$$\frac{u_E}{E} = \left[\frac{2\nu^2}{(1-\nu^2)}\right] * \left[\frac{u_\nu}{\nu}\right] \tag{2.11}$$

Now, for example, assuming that υ is 0.3 (a general value for polymers) and that there is a 25% uncertainty in the Poisson's ratio (which is larger than typically acceptable), we will obtain a rather "worst-case" estimate of the fractional uncertainty in the elastic modulus of the sample. Using Eqn. 2.11, we find that the fractional uncertainty in the sample elastic modulus is less than 5%. Therefore, supplying an educated guess for a value for the Poisson's ratio based on general knowledge of the material will yield a relatively reliable sample elastic modulus.

2.2.2.5.2. Instrument-Related

2.2.2.5.2.1. Noise and Resolution

As with all measurement techniques, there are error sources related to machine resolution and noise. There are limits to the level of force and displacement that can be accurately measured by a nanoindenter. Variations below this resolution limit are unable to be discerned, and this can lead to error propagation. Along this vein, nanoindenters are also

quite susceptible to environmental noise due to the resolution scale of the forces and displacements. This environmental noise is often of the magnitude and frequency that it hinders data analysis (especially when implementing the CSM technique), and, in rare cases, is enough to entirely disrupt the experiment. Environmental chambers and vibration isolation tables are often employed to combat the effects of noise.

2.2.2.5.2.2. Thermal drift

Thermal drift occurs when there is a thermal mismatch between the indenter, sample, and environment. Often, the effects of thermal drift manifest themselves in much the same way as those of creep. Dimensional changes due to tip or sample heating or cooling can alter applied forces, contact areas, or tip displacements. These contributions will certainly affect the resulting measurements for elastic modulus and indentation hardness. On a positive note, thermal drift can often be differentiated from creep in a certain fashion – introducing a hold segment at low load in the unloading portion (when creep is much less likely to occur) can reveal thermal drift contributions. The data for the entire experimental run can then be corrected based on the data gathered from the thermal drift characterization.

2.2.2.5.2.3. Tip area function

Calibrating the indenter tip is one of the most critical steps towards obtaining meaningful results from a nanoindentation. Typically, the area function for the tip is calibrated on a sample of fused silica using multiple indentations of various final depths. Due to the nature of indentations, errors in this area function are most prominent at small indentation

depths, where the area function depends heavily on initial loading data, which itself can be wrong due to uncertainties in initial tip-to-surface contact. Also, due to the small cross-sectional area of sharp tips at small penetrations, area errors tend to be proportionally larger. General errors in the tip area function will present themselves throughout the indentation however, so proper calibration is critical.

The area function calibration is technically only valid up to the depth to which it penetrates the fused silica sample. A more robust, though less accurate, fit can be obtained by using only positive coefficients, which allows the fit to be applied to depths deeper than the calibration depth. Certain material systems, such as polymers, are much more compliant than the fused silica. Since nanoindenters are typically force-resolved devices, at maximum load, the indenter tip penetrates further into a softer material. Therefore, though the area function for the tip was calibrated up to a certain depth using the fused silica, the tip penetrates much further into the polymer and the area function is then extrapolated to cover the increased depth. There is still some discussion as to whether this approach is valid.

2.2.2.5.2.4. Instrument Compliance

Proper instrument calibration also includes a step for accounting for the compliance of the load frame of the nanoindenter. The frame of the machine itself can deflect under load, as depicted in Figure 2.4. The displacement transducer within the machine has no way of differentiating between frame deflection and sample penetration; frame deflection can introduce false sample penetration values, which will significantly alter the material properties derived from the ensuing data. Again, using a fused silica calibration standard

and calibration techniques specific to each machine, researchers can account for the compliance of the load frame, and eliminate the component of the machine deflection from the force-vs.-displacement data for the indentation experiment.

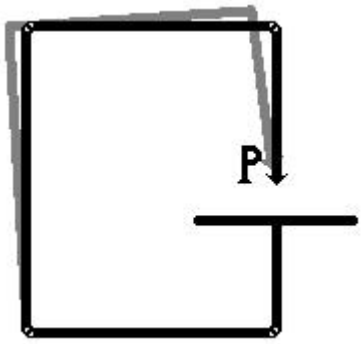

Figure 2.4. Exaggerated deflection of compliant load frame.
Black frame is in relaxed state, grey is loaded state.

2.3. Experimental

2.3.1. Materials

The monomer used, as-received, was the propoxylated glyceryl triacrylate SR9020 (Sartomer Corp.), the structure of which is shown in Figure 2.5.

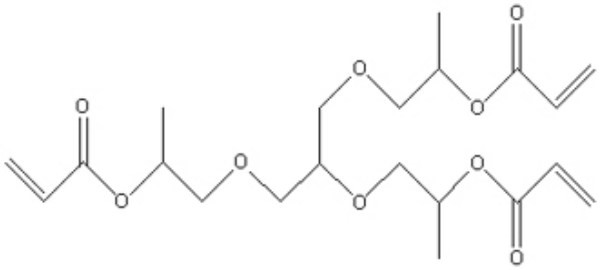

Figure 2.5. Chemical structure of SR9020

Bulk-polymerized samples used 2,2-dimethoxy-2-phenylacetophenone at a concentration of 0.1 wt% as an ultraviolet photoinitiator. For TPS, the photoinitiator used was E,E-1,4-bis[4-(di-*n*butylamino)styryl]-2,5-dimethoxybenzene (DBASB), at a concentration of 0.1 wt%. DBASB is an extremely effective two-photon photoinitiator which exhibits a maximum absorption cross-section at 730 nm of 900 GM (1 GM=10^{-50} cm^4·sec/photon). The exposure conditions tested are listed in Table 2.1.

Table 2.1. Exposure conditions for SR9020 structures.

Stage Speed (mm/s)	**Power (mW)** (before objective)						
80	20	30	40	60	80		
40	10	20	30	40	60		
20	10	20	30	40	60		
10	5	10	15	20	30	40	
1	5	7.5	10	12.5	15	20	30

2.3.2. Methods

Three bulk-polymerized sheets were created by injecting the monomer/initiator solution into a mold consisting of two slides separated by 1 mm spacers and secured with binder clips and exposing the mold to a UVP Blak-Ray® 365nm UV light (intensity ~8 mW/cm^2) for 5 minutes. Prior to injection, the slides were thoroughly cleaned with acetone.

Samples for dynamic mechanical analysis (DMA) were obtained by excising a portion of the polymer sheet with a razor blade and polishing the edges with 800- and then 1200-grit silicon-carbide sandpaper, to arrive at final specimen dimensions of approximately 20 mm x 4.5 mm x 1 mm. A TA Instruments Q800 DMA was used to obtain the storage

modulus (E') and loss factor (tan δ) curves in tensile mode. The samples (n=2) were cooled to 0 ºC, equilibrated for 2 minutes, and then ramped at a rate of 2 ºC/min to 240 ºC. The frequency was set to 1 Hz, the force track was set to 150%, and the strain level was set to 0.1%. T_g was determined by the peak of the tan(δ) curve, E_r was defined as the lowest point in the storage modulus curve, and E_{room} is the storage modulus at room temperature. All DMA values are reported as arithmetic mean ± difference to maximum or minimum.

Two-photon stereolithography was performed with a Spectra-Physics Tsunami Ti:Sapphire oscillator operating at 730 nm and a repetition rate of 82 MHz with 80 fs pulses. The apparatus consisted of a 10x expansion telescope which was used to effectively overfill the Nikon NA = 1.4, 60 oil immersion plan apochromat objective that focused the laser into the monomer. A microscope slide treated with 3-(trimethoxysilyl)propyl methacrylate (an adhesion promoter) was used as a substrate. The monomer solution was contained in a cell bounded by the adhesion-promoted microscope slide and a coverslip, separated by a 50 μm thick Teflon spacer-washer. The structures were bars of varying length but were all 20 μm wide (in 50 nm lateral steps), as seen in Figure 2.6, and 18 μm tall (60 layers using 300 nm steps). This spacing was chosen to ensure sufficient overlap of the polymerized voxels created by the two-photon technique [181]. The bars were fabricated by translating the slide via a computer-controlled Newport XPS 3D positioning stage while the laser focus stayed fixed. Following exposure, the slide was rinsed twice in methanol for a total of fifteen minutes in order to wash away the residual unexposed monomer and develop the solidified structures.

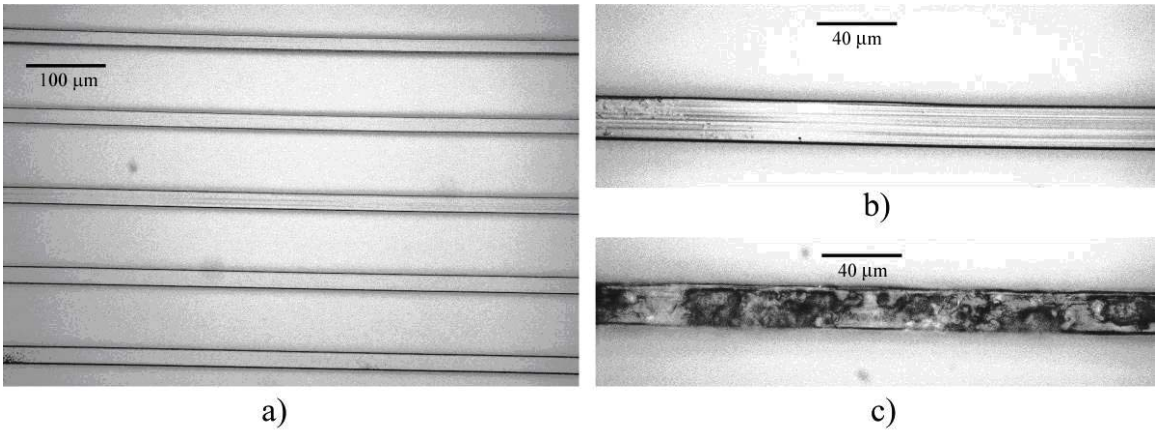

Figure 2.6. Optical micrographs of two-photon polymerized bars.
(a) 20x of bars in parameter array (b) 50x of excellent bar (c)50x of damaged bar.

Nanoindentation was performed on a Nanoindenter XP® (MTS NanoInstruments) with the dynamic contact module (DCM) column outfitted with a diamond Berkovich tip and utilizing the continuous stiffness measurement (CSM) technique for accurate surface contact determination [112]. The parameters for all of the indentations were: a maximum depth of 1500 nm, an indentation strain rate of $\left|0.05\ s^{-1}\right|$, a harmonic frequency of 45 Hz, and a harmonic amplitude of 2 nm. The tip was calibrated using an SiO_2 standard with five positive coefficients. The TPS materials were indented to ~10% of the overall thickness (~1800-2000 nm) to obtain the maximum amount of data, which is beyond the range of an accurate fit to SiO_2, given that the indenter was not capable of penetrating the SiO_2 more than 400 nm. Therefore, a robust, all-positive coefficient fit to SiO_2 can be used beyond the calibration range, but such a fit is inherently less accurate.

2.4. Results

DMA revealed (Figure 2.7) that the T_g of SR9020 was 78.6±1.77 °C and that the transition was broad (~90 ºC) as determined by tan(δ). It further showed that E_r was

235.7±1.45 MPa. The modulus of the material at room temperature, or the conditions where nanoindentation was performed, was 1858.5±43.5 MPa.

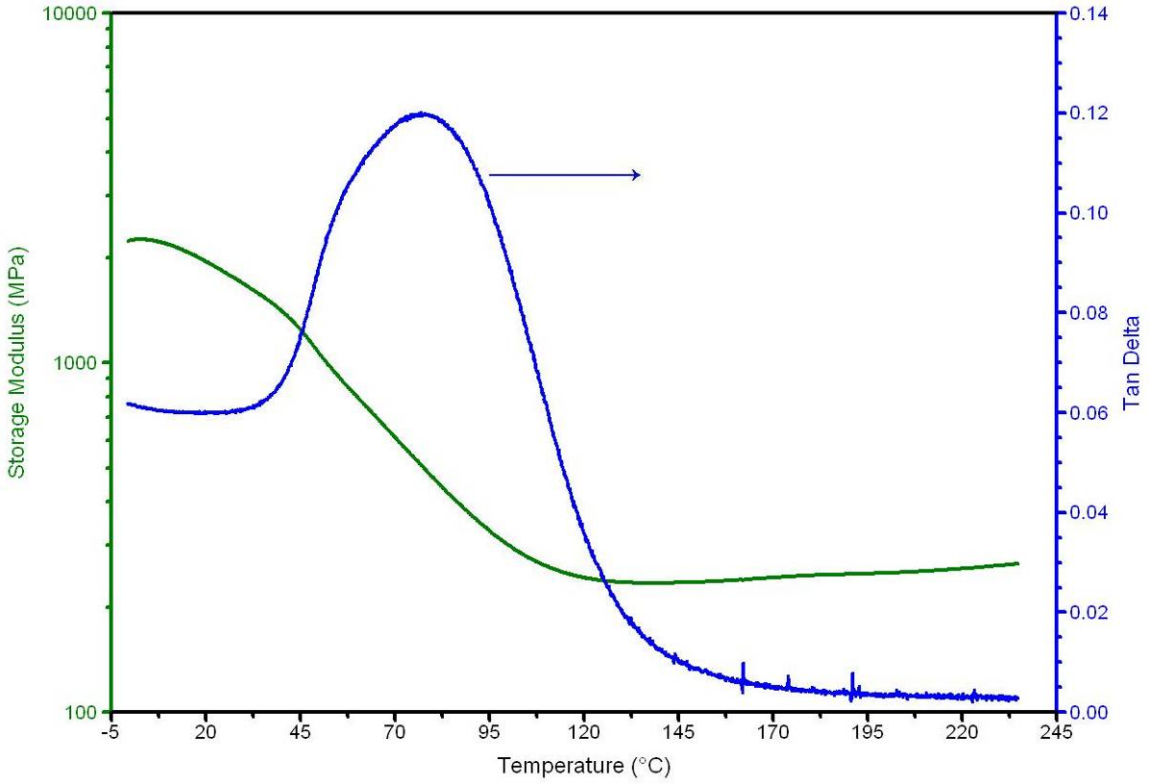

Figure 2.7. Results from dynamic mechanical analysis of SR9020

One exposure condition from the first sample was underexposed and did not result in a structure that was able to be indented: 80mm/s with 20 mW**.** The exposure conditions from the first sample which hindered indentation due to a cratered surface (Figure 2.6c) caused by excessive polymerization heat evolution and resultant local monomer boiling were: 1 mm/s with 20 and 30 mW, 20 mm/s with 60 mW, and the majority of the 10 mm/s and 40mW bar.

The load-depth (or compliance) curves for various selected materials are shown in Figure 2.8. The low depth detail can be seen in the inset – all of the materials begin with a negative load-displacement behavior; the deepest-to-shallowest return to zero load matches with the lowest-to-highest maximum load during indentation order, with the exception of the reversal of the 10 mm/s and 20 mm/s materials and the bulk material, which exhibited the shallowest return to zero load.

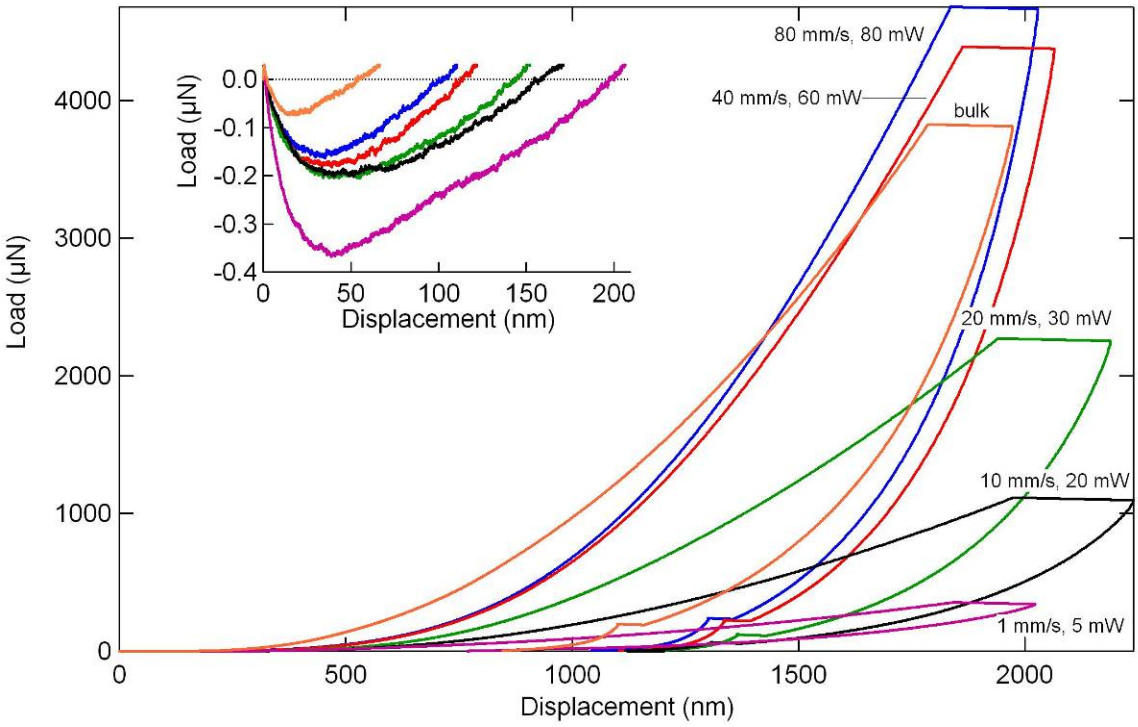

Figure 2.8. Compliance curves for representative processing conditions. Inset: low depth detail highlighting 'adhesive' behavior.

Due to the load-controlled, depth-feedback construction of the MTS Nanoindenter XP, the indentation depths exceeded the desired input. However, modulus data from the CSM technique did not indicate an increase in modulus beyond the "rule-of thumb" 10% penetration depth, so any unload modulus value at 11 or 12% depth is still representative

of the polymer material and does not incorporate any substrate effects. Thus, the slope of the unload portion of the compliance curve was used to calculate the elastic modulus in the typical fashion [113], and is shown in Figure 2.9 as a function of both input power and stage translation speed. The modulus for the 80 mm/s and 80mW condition was the highest at 1.395 GPa, and the lowest modulus was 29.85 MPa for 10 mm/s and 5 mW. The modulus of the bulk-polymerized sample is indicated by a horizontal gray line, and is 1003±13.63 MPa. The general shape for a given speed is a linear decrease with wattage, and there are two distinct regions with different slopes. Power settings above 20 mW result in a slope of ~23 MPa/mW; at power settings of 20 mW and below, the slope is a little less than half of that at ~10 MPa/mW.

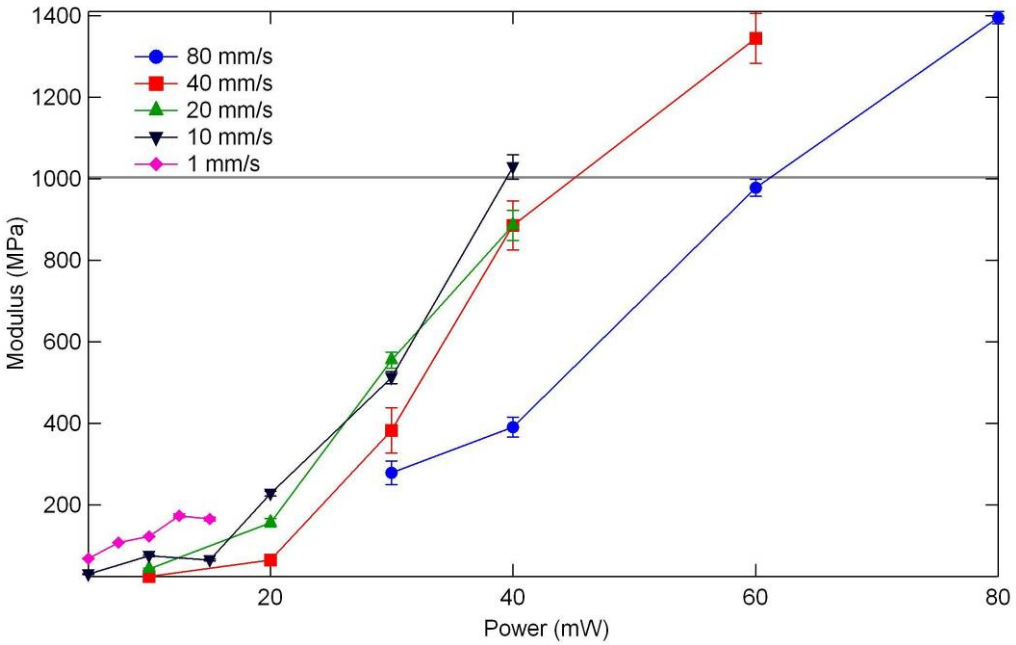

Figure 2.9. Graph of unload modulus, grouped by exposure condition. Horizontal gray line indicates bulk-polymerized modulus from nanoindentation.

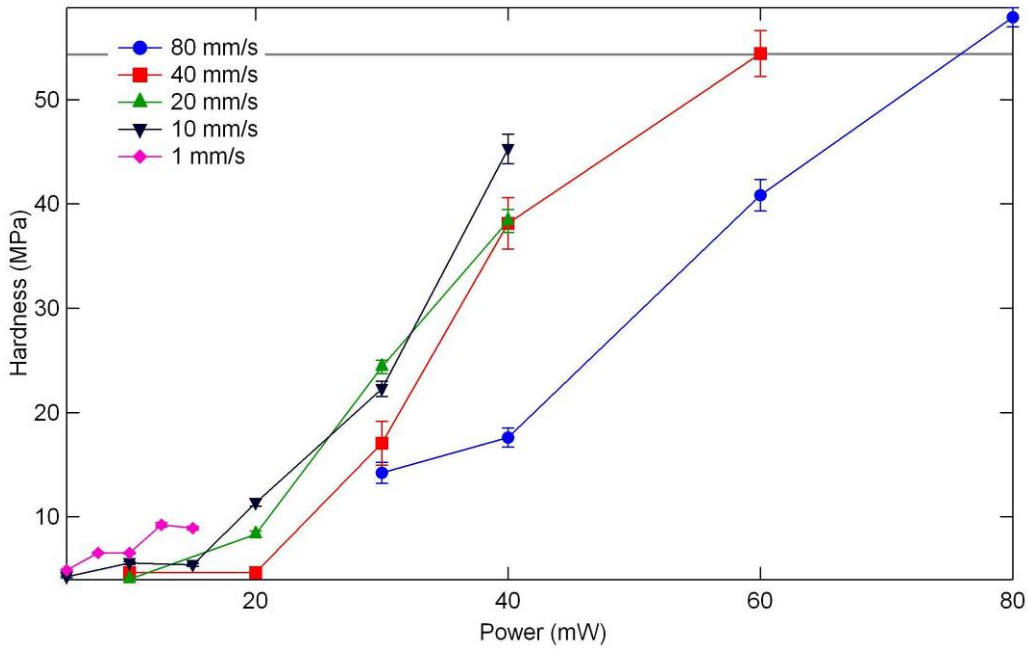

Figure 2.10. Graph of indentation hardness at maximum load (quasistatic). Horizontal gray line indicates indentation hardness of bulk-polymerized material.

Figure 2.10 summarizes the quasistatic indentation hardness values for each material at maximum load. The maximum indentation hardness was 57.9 MPa for 80 mm/s and 80 mW while the lowest value was 4.26 MPa for 10 mm/s and 5 mW. The indentation hardness of the bulk-polymerized sample was 53.4±0.965 MPa, and is denoted in the figure by a horizontal gray line. The general trends for the hardness vs. power are similar to that for the modulus vs. power with the same threshold power of 20 mW and rough ratio between the slopes of the two regions (0.921 MPa/mW in higher power region: 0.426 MPa/mW in lower power region).

Figure 2.11 shows the same data from Figure 2.9 except the exposure parameters have been collapsed into a single parameter – dose. The modulus values, when graphed against dose (calculated as $dose = Power^4 / v$), show a nonlinear saturation behavior as

the dose is increased. The indentation hardness data exhibit similar trends when plotted against dose in this fashion (not shown).

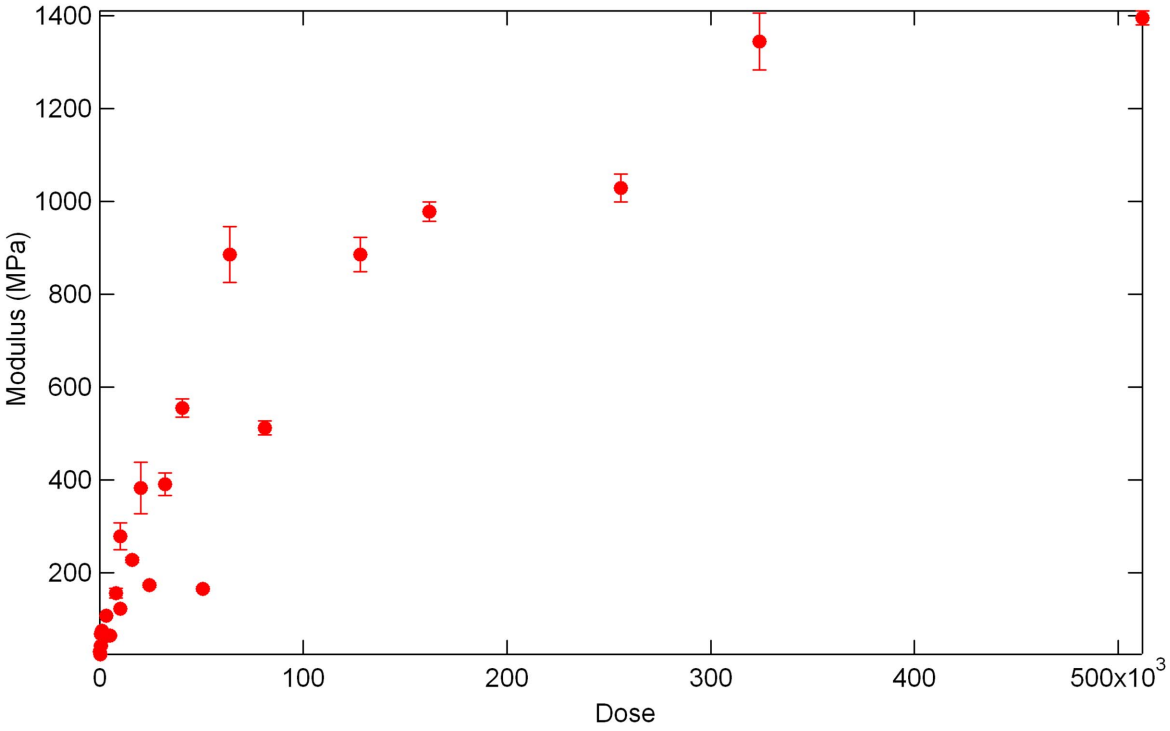

Figure 2.11. Elastic modulus vs. dose for SR9020 structures, using n=4 photons for multi-photon dose calculations.

2.5. Discussion

From information obtained from DMA, it is apparent that, as anticipated from the structure of the monomer, the general structure of SR9020 is a highly crosslinked three-dimensional network polymer. The transition from glassy to rubbery is very broad as evidenced by the breadth of the tan(δ) and the onset point is not sharply defined by the storage modulus. However, it is clear from tan(δ) and the magnitude of the storage modulus that SR9020 is still in its glassy state at room temperature.

The SR9020 exhibits a seemingly adhesive behavior at first contact, where the tip is pulled into the surface during initial penetration and denoted by a negative load-depth relationship (Figure 2.8). There is a relationship between initial compliance and the depth at which the load returns to zero. More compliant materials tend to return to zero load more quickly and reach a smaller maximum negative load than less compliant materials. However, the consequences of this behavior on the bulk response are thought to be minimal because even the deepest return to zero load takes place in 2/3 of the first layer and the maximum negative load is less than 0.1% of maximum load during indentation.

The TPS materials showed a more compliant behavior at low depths and less compliant behavior at larger depths during loading than the bulk material, denoted by the lower and then higher load compared to the bulk material for various depths (Figure 2.8). This behavior is indicative of the sequential and layered construction of the bars created by two-photon processing. The indenter encounters little resistance at low penetration depths as few layers are encountered, but as more layers are penetrated, the interaction between layers becomes more pronounced and the indenter encounters the true "bulk" behavior of the material. Upon unloading, sufficient layers are penetrated that the response is indicative of the bulk of the material itself and not of the surface layers.

Power (or intensity) has more of an effect on the modulus and hardness of the SR9020 created via TPS than translation speed does (Figure 2.9 and Figure 2.10). Halving the power results in greater decreases in modulus than doubling the speed does, for example. This can be expected, given the power-law dependence of dose on intensity for a multi-

photon process ($dose \propto I^n t = I^n / v$ where n is the number of photons). The general trends for modulus and hardness as speed and power are changed follow accepted behavior for standard processing - low speeds and high powers both result in a higher applied dose. The modulus vs. dose relationship is shown in Figure 2.11 for a 4-photon process*, indicating that there is saturation behavior for the network behavior relative to dose as dose is increased. A higher dose generally translates to higher conversion, and higher conversion in this case leads to a more fully crosslinked network. Under the same testing conditions, materials with high crosslink density will be stiffer and harder than the equivalent chemistry with less dense crosslinking.

Additionally, though the bulk-polymerized material has reached maximum conversion *given its polymerization conditions*, it is less stiff and slightly softer than some materials polymerized and more fully converted using the conditions for TPS as shown in Figure 2.9 and Figure 2.10. This apparent discrepancy of variable maximum conversion and crosslinking density of the materials can be attributed to the fact that in photopolymerization, intensity as well as dose plays an important role in overall conversion. At equivalent dosages, it is typical for higher intensities to result in higher conversion levels in acrylates [47, 183, 184] due to increased heat evolution and enhanced molecular mobility, which is critical in the later diffusion-limited stages of acrylate polymerization.

---

* A 4-photon process has been identified for this initiator-material system in previous work [182]. Though a two-photon process still radicalizes the initiator, it has been proposed that a 4-photon process causes an ionization process which eventually radicalizes both the dye (initiator) and acrylate molecule in a more statistically significant process. Nanoindentation results support the hypothesis of a 4-photon process.

There are essentially two regions in both the modulus vs. speed and the hardness vs. speed graphs. These two regions in each graph are differentiated by the trendline slopes, and are separated by the 20 mW threshold. It is possible that below this power setting, there is insufficient heat generation to promote diffusion in the gelled network, given the thermal characteristics of the monomer and polymer. Overall conversion would be relatively lower, so that small increases in power result in small increases in overall conversion. However, above this setting, the polymerization rate is high enough to generate a sufficiently large exotherm to allow for higher conversions, such that small increases in power generate much larger exotherms and conversion is greatly increased. It is anticipated that because the overall dose affects the conversion as well, a study which uses finer power steps around 20 mW would determine the particular threshold power setting based on platform translation speed.

2.6. Conclusions

Nanoindentation is a very versatile method for determining the characteristics of a broad range of materials. It has opened the door to a world of new studies, including thin film adhesion studies and micron-scale structure testing. Researchers have used nanoindentation to measure properties of biological materials, such as the wax layer on pitcher plants and the mandible of an ant. However, nanoindentation analysis is based on some assumptions which eliminate certain groups of materials from the basic procedures. Strongly adhesive materials which artificially recover due to adhesion to the tip during retraction instead of purely elastic recovery, non-work hardening metals which pile-up excessively, and rough materials with irregular and large asperities are all currently not

well-suited for nanoindentation because of the errors that are introduced and not accounted for in the assumptions. Given the material studied, the aforementioned errors do not apply, even though the material does exhibit a very weak "adhesive" response during initial contact. Nanoindentation suffers from a range of errors, many of which have been resolved, and others which have begun to be quantified by research efforts around the world.

A basic processing parameter space has been defined by determining which conditions which showed underdevelopment or excessive heat evolution. Furthermore, the research provides the first mechanical characterization of polymer structures created via two-photon stereolithography, especially as compared to typical bulk photopolymerization processing. A processing parameter-to-property map has been developed, and it is possible to obtain stiffer and harder materials with two-photon processing than with standard UV bulk photopolymerization. However, additional testing around the 20 mW threshold for various translation speeds would improve the definition of the threshold. Alternative complementary forms of chemical analysis, such as Fourier transform infrared spectroscopy, would elucidate the relationship between acrylate conversion and modulus for these parameters. It should be noted that SR9020 shows some unexpected, possibly adhesive effects upon initial loading regardless of polymerization method, indicating a strong need to investigate the surface energy of this material specifically before its implementation in nanoscale/microfluidic devices where surface interactions dominate.

CHAPTER 3. SYNTHESIS AND THERMOMECHANICAL BEHAVIOR OF (QUA)TERNARY THIOL-ENE(/ACRYLATE) COPOLYMERS

3.1. Summary

Having characterized the thermomechanical properties of an exemplar material in both bulk and photopatterned form, the next step was to determine the properties of another class of polymer with the potential for high quality photopatterning with thermomechanical property tunability. Therefore, the objective of the work described in this chapter was to characterize and understand the structure-to-thermomechanical property relationship in thiol-ene and thiol-ene/acrylate copolymers in order to complement the existing studies on the kinetics of this polymerization reaction. A series of forty-one distinct three- and four-part mixtures were created with systematically varied functionality, chemical structure, type and concentration of crosslinker. The resulting polymers were subjected to dynamic mechanical analysis, Fourier transform infrared spectroscopy, and tensile testing at their glass transition temperature, T_g, to quantify to quantify and understand their thermomechanical properties. The copolymer systems exhibited a broad range of T_g (-40 to 43 °C), rubbery modulus - E_r (<0.1 to 35 MPa) and failure strain (20% to >500%). Dynamic mechanical analysis revealed that the addition of thiol or –ene crosslinker resulted in increased crosslink density, marked by an increase in E_r and accompanied by an increase in T_g. The addition of a difunctional high T_g acrylate to several three-part systems increased the resultant T_g and E_r. FTIR spectroscopy showed that the addition of the acrylate to the mixture results in some unconverted –ene functional groups due to a competitive reaction scheme. Sol-fraction

testing uncovered a strong link between mass loss and monomer purity, with some relation to network size and conversion. Finally, higher crosslink densities generally result in higher stress and lower strain at failure. The tunability of the thermomechanical properties of these copolymer systems is discussed in terms of inherent advantages and limitations in light of pure acrylate systems.

3.2. Introduction

For the better part of a century, (meth)acrylates have formed a versatile class of polymers that play a major role in military and commercial products, as well as in industrial and academic research. Acrylates are popular because of their relatively low cost, ready availability, ease of monomer synthesis and polymer manufacture and processing, rapid polymerization kinetics, optical clarity, toughness, potential biocompatibility [64, 85-87], and the broad range of achievable properties [84]. Photopolymerization of acrylates, in particular, is popular because of its relatively low energy requirements, capacity to be performed at ambient temperatures, and rapid speed [45-54]. Photolithography has featured acrylates, almost to the exclusion of other materials, since the very inception of the technique, due mostly to the acrylates' rapid curing kinetics and partly to the other aforementioned benefits. Typically, highly functional acrylate monomers are used to insure rapid polymerization and pattern fidelity; these highly crosslinked networks shrink less than networks formed from monomers with lower functionality. As a direct result of the high crosslink density (or low molecular weight between crosslinks) and monomer chemistry, these networks exhibit glassy behavior at ambient temperatures - e.g. high stiffness and low ductility. Acrylates are also used for shape memory applications [63,

65, 93], because the glass transition temperature (T_g) and rubbery modulus (E_r) can be tailored independently to suit a particular application. There is another class of polymer, called thiol-ene, that is also readily photopolymerizable and may be well suited to shape memory applications, complementing, and perhaps partially replacing the use of pure (meth)acrylates while expanding the range of achievable properties.

However, before the thiol-ene polymers can be translated into any application, such as shape memory use or photolithography, a more rigorous understanding of the system behavior in bulk form is necessary. The majority of the studies on thiol-ene and thiol-ene/acrylate systems have focused on the reaction kinetics [2-5, 15, 16, 20-24, 33, 37, 98], while few have studied the thermo-mechanical properties of the resultant material in great detail [29, 33, 34, 36, 111]. A rigorous process-to-thermo-mechanical property study of thiol-ene/acrylates was performed by the Hoyle group [37], who studied the effect of acrylate structure on the properties of various ternary copolymers composed of one trithiol, one tri-ene, and one of a selection of (meth)acrylates. The current study describe in this chapter aimed to more thoroughly define the thermomechanical properties of a (qua)ternary thiol-ene/acrylate system with systematically varied functionality, chemical structure, type and concentration of crosslinker. Additionally, this study aimed to determine the behavior of the systems at equivalent macromolecular states, whereas the aforementioned study was solely performed at room temperature, irrespective of the polymers' T_g's, in an effort to identify a polymer system with optimal impact resistance at ambient temperature. Since the thermo-mechanical properties of a material are a critical parameter in the design of a device, the goal of the research detailed in this chapter was to photopolymerize a series of thiol-ene monomer mixtures with

systematically varied crosslinker concentration to determine the effect of this parameter on the properties of the copolymer. Additionally, the effect of adding a high T_g diacrylate at selected concentrations to chosen thiol-ene base systems was investigated to determine the effect that the acrylate has on the overall group conversion and resultant properties of the quaternary copolymer. In essence, the results of this study will complement the results of earlier polymerization kinetics studies by providing the second half of the thiol-ene(/acrylate) polymerization process-property map.

3.3. Experimental

For clarity of presentation, the polymer composition labeling is centered around the equivalence of functional groups and is broken into two parts – the thiol functional group component, $t_f$mol%, and the –ene functional group component, $e_f$mol% - each totaling 100% and insuring a stoichiometric ratio of the functional groups. Acrylate functional groups, when added, are indicated by $a_f$mol%; terminology and labeling for compositions including acrylates differ slightly from the ternary mixtures and will be explained appropriately.

3.3.1. Materials

Forty-one monomer mixtures (shown in Table 3.1) were made of various combinations of three or four of the five monomers whose chemical structures and abbreviations are shown in Figure 3.1, with the exception of one composition consisting entirely of Bisphenol A ethoxylate diacrylate, M_n=512 [BPAEDA(512)]. 2,2-dimethoxy-2-phenylacetophenone (DMPA) was used as the UV photoinitiator. The naming

convention used herein highlights the critical parameter of the study – the concentration of crosslinker. All ternary mixtures used DMPA as the photoinitiator at a concentration of one initiator molecule per 1,000 –ene groups, or +0.1 $e_f$mol% (the plus is included to denote that it is additive, not substitutive for the –ene functionalities). DMPA acted as the photoinitiator in quaternary mixtures as well, but at a concentration of one initiator molecule per 1,000 –ene *and* acrylate groups (+0.1 e_f+$a_f$mol%). The pure BPAEDA(512) reference sample contained DMPA at one part per 1,000 acrylate groups (+0.1 $a_f$mol% or +0.1 wt%). All materials were obtained from Sigma Aldrich and were used as received.

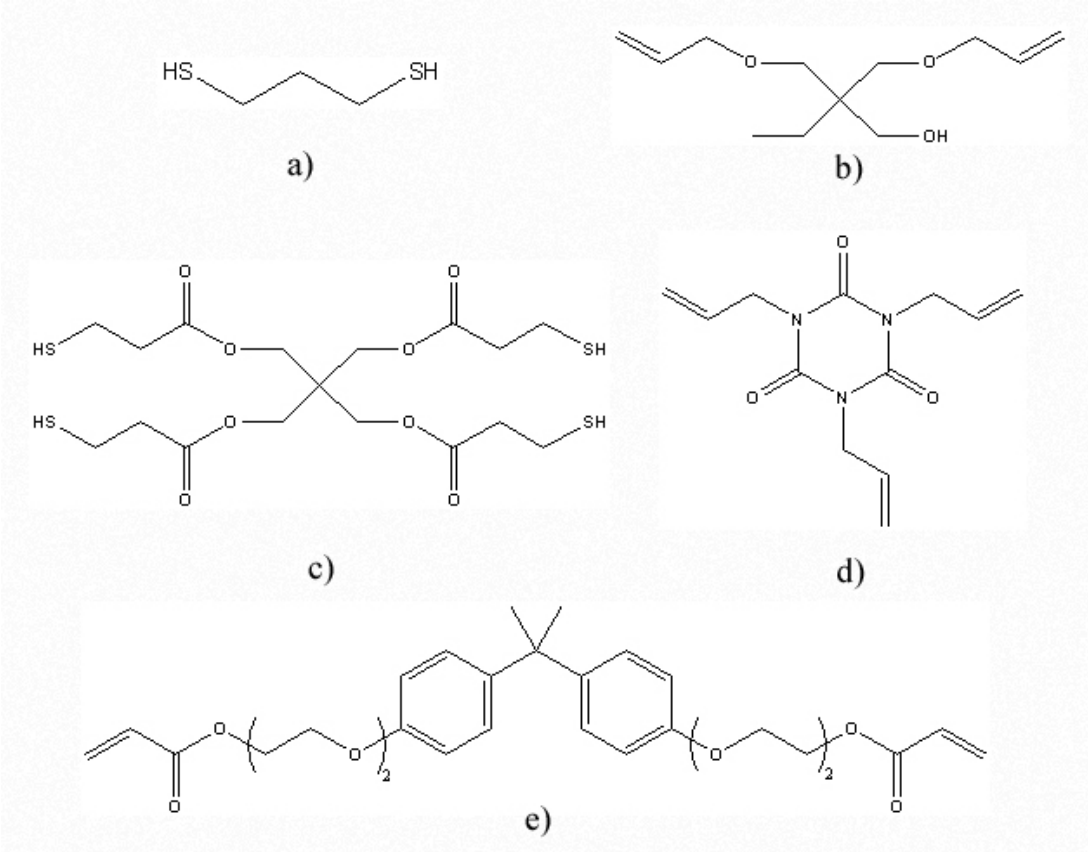

Figure 3.1. Chemical structures of studied monomers.
a) 1,3-propanedithiol (PDT), b) trimethylolpropane diallyl ether (TMPDAE), c) pentaerythritol tetrakis(3-mercaptopropionate) (PETMP), d) 1,3,5-triallyl-1,3,5-triazine-2,4,6(1H,3H,5H)-trione (TATATO), e) Bisphenol A ethoxylate diacrylate, M_n 512 (BPAEDA(512))

Table 3.1. Monomer mixtures used in study

		$t_f$mol%		$e_f$mol%		$a_f$mol%
Mix	**Mix Name\Chemical**	PDT	PETMP	TMPDAE	TATATO	BPAEDA(512)
1	10PETMP	90	10	100	-	-
2	13.33PETMP	86.67	13.33	100	-	-
3	16.67PETMP	83.33	16.67	100	-	-
4	20PETMP	80	20	100	-	-
5	30PETMP	70	30	100	-	-
6	40PETMP	60	40	100	-	-
7	50PETMP	50	50	100	-	-
8	60PETMP	40	60	100	-	-
9	70PETMP	30	70	100	-	-
10	80PETMP	20	80	100	-	-
11	90PETMP	10	90	100	-	-
12	100PETMP	-	100	100	-	-
13	10P+25BPAEDA(512)	90	10	100	-	+25
14	10P+50BPAEDA(512)	90	10	100	-	+50
15	10P+75BPAEDA(512)	90	10	100	-	+75
16	50P+25BPAEDA(512)	50	50	100	-	+25
17	50P+50BPAEDA(512)	50	50	100	-	+50
18	50P+75BPAEDA(512)	50	50	100	-	+75
19	90P+25BPAEDA(512)	10	90	100	-	+25
20	90P+50BPAEDA(512)	10	90	100	-	+50
21	90P+75BPAEDA(512)	10	90	100	-	+75
22	10TATATO	100	-	90	10	-
23	20TATATO	100	-	80	20	-
24	30TATATO	100	-	70	30	-
25	40TATATO	100	-	60	40	-
26	50TATATO	100	-	50	50	-
27	60TATATO	100	-	40	60	-
28	70TATATO	100	-	30	70	-
29	80TATATO	100	-	20	80	-
30	90TATATO	100	-	10	90	-
31	100TATATO	100	-	-	100	-
32	10T+25BPAEDA(512)	100	-	90	10	+25
33	10T+50BPAEDA(512)	100	-	90	10	+50
34	10T+75BPAEDA(512)	100	-	90	10	+75
35	50T+25BPAEDA(512)	100	-	50	50	+25
36	50T+50BPAEDA(512)	100	-	50	50	+50
37	50T+75BPAEDA(512)	100	-	50	50	+75
38	90T+25BPAEDA(512)	100	-	10	90	+25
39	90T+50BPAEDA(512)	100	-	10	90	+50
40	90T+75BPAEDA(512)	100	-	10	90	+75
41	100BPAEDA(512)	-	-	-	-	100

3.3.2. Methods

Polymer sheets were created by injecting monomer solution into a mold consisting of two slides separated by 1 mm spacers and secured with binder clips and exposing the mold to a UVP Blak-Ray® 365nm UV light (intensity ~8 mW/cm^2) for 5 minutes. Prior to injection, the slides were thoroughly cleaned with acetone; for the 10PETMP mixture, RainX was applied to the slides to act as a release agent, due to the tacky nature of the finished polymer. A minimum of three sheets (or slides) of each mixture were polymerized.

Samples for dynamic mechanical analysis (DMA) were obtained by excising a portion of the polymer sheet with a razor blade and polishing the edges with 800- and then 1200-grit silicon-carbide sandpaper, to arrive at final specimen dimensions of approximately 20 mm x 4.5 mm x 1 mm. A TA Instruments Q800 DMA was used to obtain the storage modulus (E') and loss factor (tan δ) curves in tensile mode. The samples ($n \geq 2$) were cooled to -100 ºC, equilibrated for 2 minutes, and then ramped at a rate of 2 ºC/min to 120 ºC. The frequency was set to 1 Hz, the force track was set to 150%, and the strain level was set to 0.1%. T_g was determined by the peak of the tan(δ) curve, and E_r was defined as the lowest point in the storage modulus curve.

Samples for Fourier-transform infrared (FTIR) spectroscopy ($n \geq 2$) were scanned in monomer form, polymerized under the UV light for 5 minutes as per the aforementioned procedure, and then scanned again to determine overall group conversion. The solutions were injected between sapphire windows with a gap thickness of 2 μm and scanned at 16 scans per spectrum with a resolution of $4cm^{-1}$ on a Varian FTS-7000 FTIR. Final group

conversions were calculated using the ratio of the polymer to monomer absorbance peak area at each group's signature wavenumber [2]: 1640 cm^{-1} for the vinyl group, 2570 cm^{-1} for thiol, and 3085 cm^{-1} for the allyl ether C=C bond,. Note that the contribution of the allyl ether to the –ene signal was accounted for by using the peak at 3085 cm^{-1}, thereby allowing separation of the –ene and acrylate group conversions.

Sol-fraction testing was performed by cutting 5 mm x 5 mm x 1 mm samples of six specific mixtures (n=3) and taking the dry mass of each. The samples were subsequently soaked in 2 mL of acetone for 48 hours to swell the networks and wash out excess monomer and other impurities. The samples were then dried in an oven at 60 °C for 72 hours, then allowed to acclimate to room conditions for an additional 72 hours. The masses of the samples were then measured again, and the mass loss was calculated using the difference between the masses prior to and following the acetone soak and drying periods.

Tensile testing samples ($n \geq 3$) were excised from the polymer sheets by an ASTM D638 type V punch. The edges of the samples were polished with 800-grit silicon-carbide sandpaper to remove visible defects. The samples were strained at their respective T_g's at a rate of 1 mm/min (strain rate: ~0.21 sec^{-1}) until failure on an MTS Instruments Insight 2 mechanical load frame with a 100N load cell. The experimental temperature was maintained by a Thermcraft, Inc. model LBO-14-8-5.25-1X-J8249_1A thermal chamber outfitted with liquid nitrogen cooling. The samples and equipment in the chamber was allowed to equilibrate for ten minutes at the testing temperature prior to test commencement. A laser extensometer was employed to measure the strain in the gage

section of the sample, marked with adhesive-backed reflective tape. Sample experiments were run to ensure that the tape did not affect the samples' deformation behavior and mechanical response. However, for a full and accurate comparison among all samples, crosshead displacement is used for strain determination; laser extensometer data are unavailable for tests at subzero temperatures due to condensation on the reflective tape and thermal chamber window, which prevented proper and accurate readings.

3.4. Results

The first step in the characterization was dynamic mechanical analysis (DMA). Figure 3.2 shows the progression of the storage modulus as the concentration of the PETMP crosslinker in a ternary mixture is increased from 10 $t_f$mol% to 100 $t_f$mol%. Figure 3.3 shows the same progression graph for the ternary mixtures ranging from 10 $e_f$mol% TATATO to 100 $e_f$mol% TATATO. In both figures, notably, the rubbery modulus increases several orders of magnitude and the temperature for the onset of the glass transition shifts higher as more crosslinking agent is added.

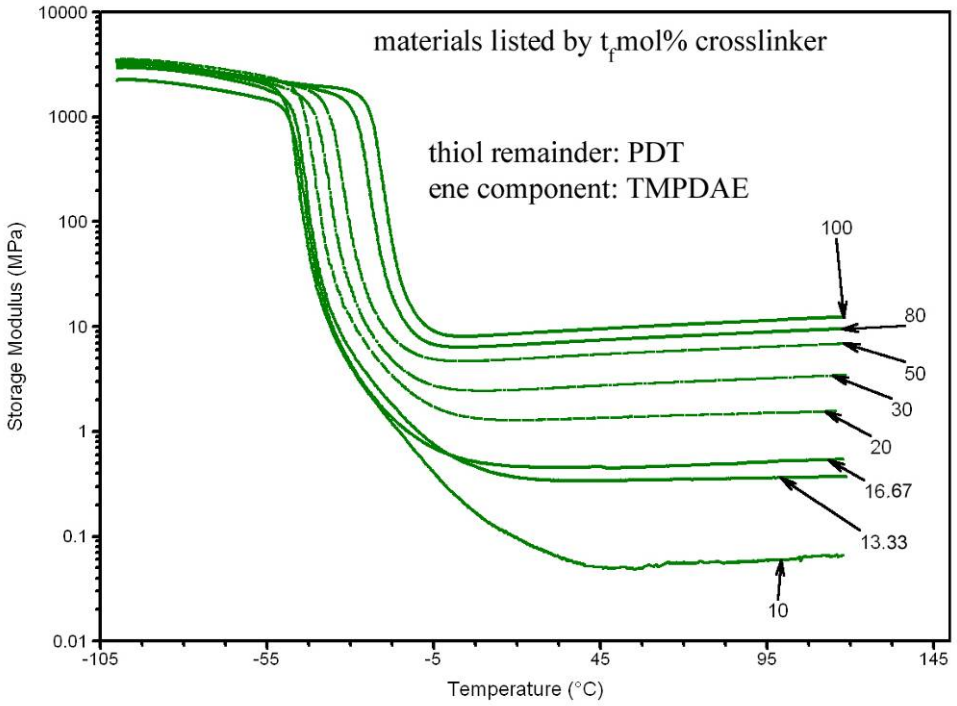

Figure 3.2. Progression of storage modulus for thiol-crosslinked ternary mixtures, by $t_f$mol% crosslinker.

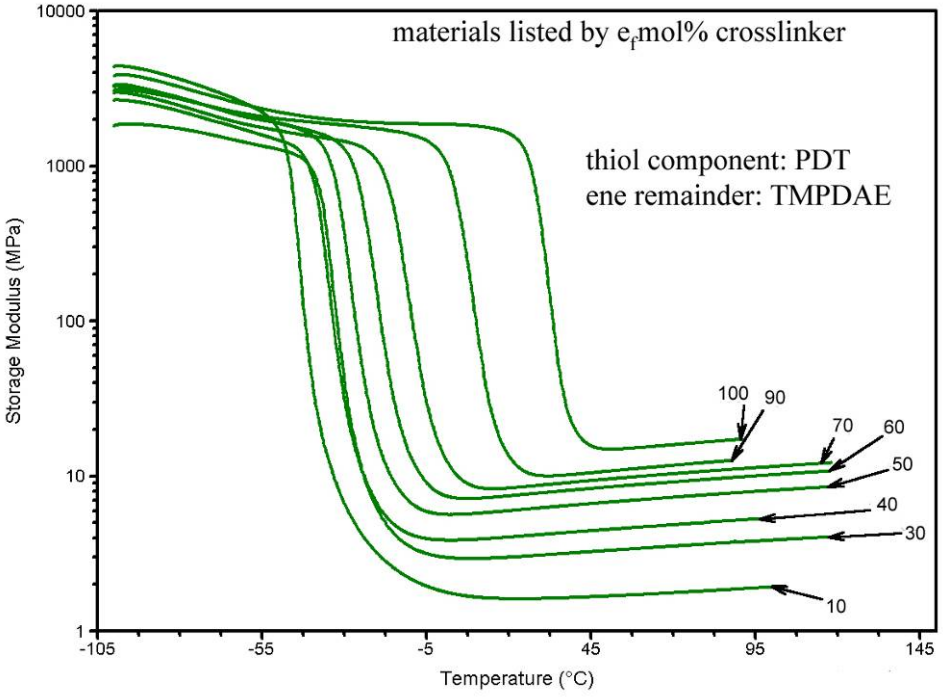

Figure 3.3. Progression of storage modulus for -ene-crosslinked ternary mixtures, by $e_f$mol% crosslinker.

Figure 3.4 summarizes the T_g values for both types of ternary mixtures, as defined by the peak of the tan(δ) curve. For PETMP crosslinked mixtures, the T_g increases from -40.2 ºC at the lowest concentration of PETMP to -16.0 ºC at 100 $t_f$mol% PETMP. The T_g increases from -39.3 ºC at the lowest concentration of TATATO to 35.3 ºC at 100 $e_f$mol% TATATO. Figure 3.5 summarizes the rubbery modulus values extracted from Figure 3.2 and Figure 3.3 for both types of ternary mixtures. The rubbery modulus increases from 54.2 kPa at the lowest PETMP concentration to 8.65 MPa at 100 $t_f$mol% PETMP, and from 1.62 MPa at the lowest TATATO concentration to 14.6 MPa at 100 $e_f$mol% TATATO.

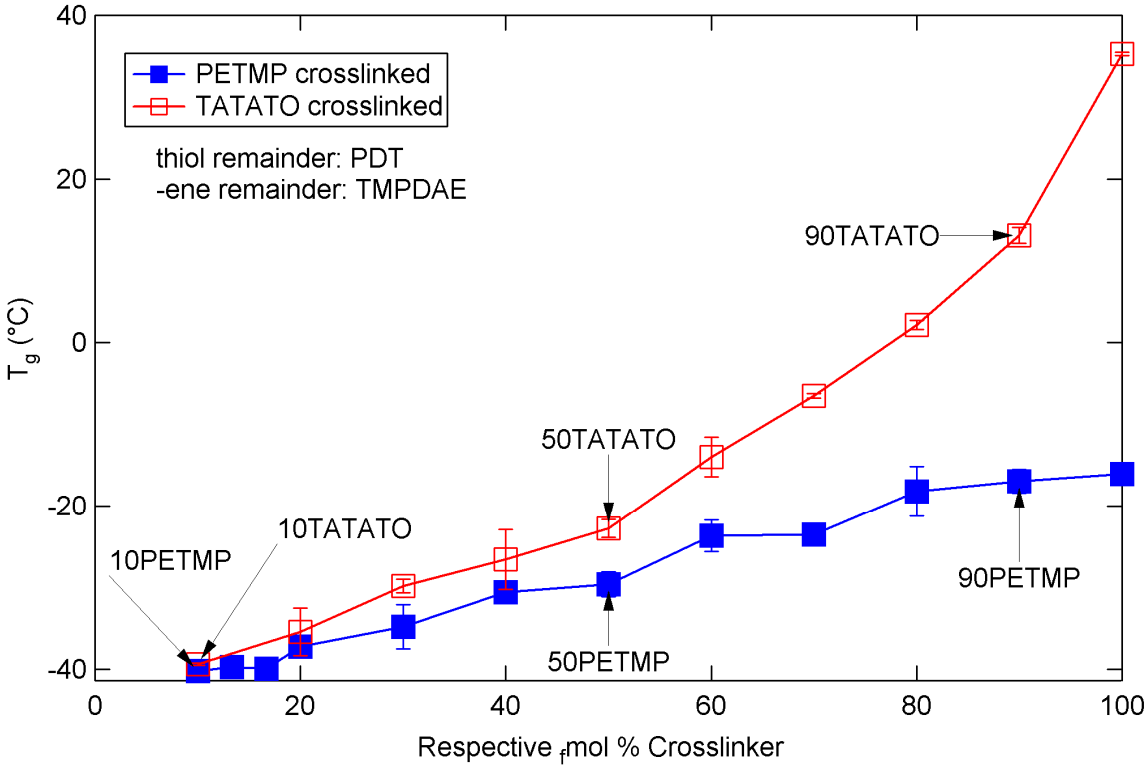

Figure 3.4. Glass transition temperatures for various ternary mixtures of TMPDAE and PDT with either PETMP or TATATO.

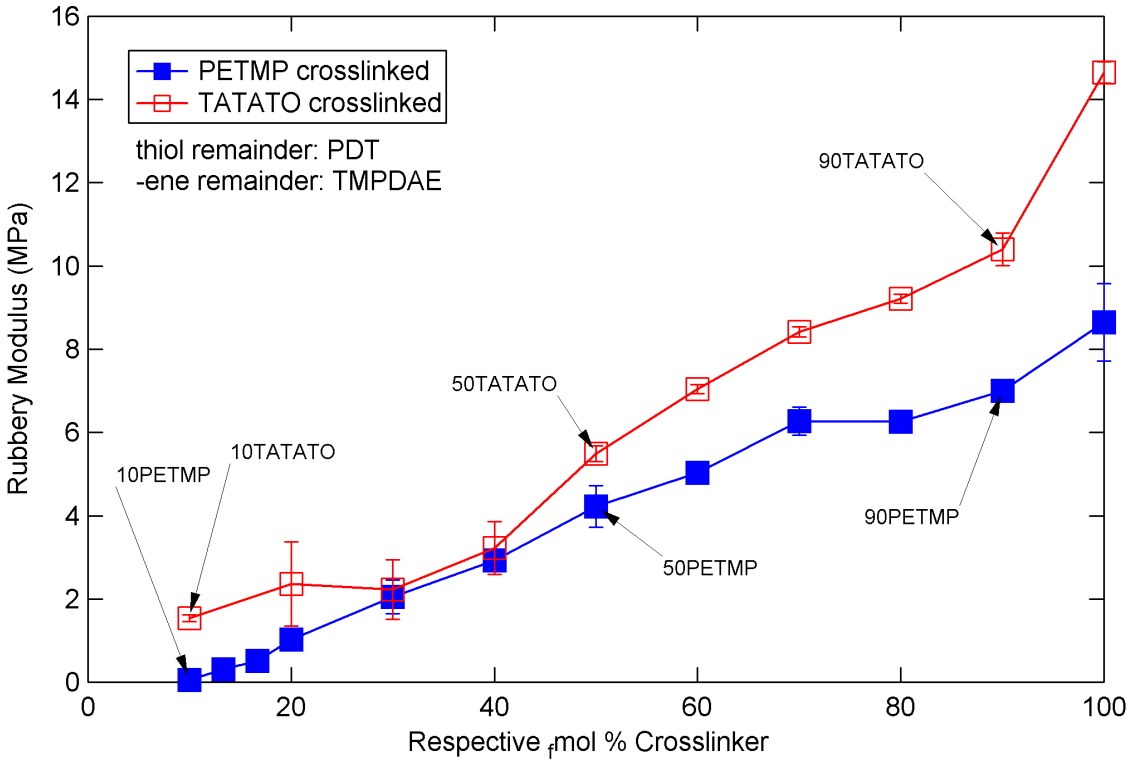

Figure 3.5. Rubbery moduli for various ternary mixtures of TMPDAE and PDT with either PETMP or TATATO.

From these results, six mixtures were chosen for determination of the effect of acrylate addition – one low (10 $_f$mol%), one medium (50 $_f$mol%), and one high (90 $_f$mol%) amount of crosslinking for both ene and thiol crosslinkers. 100 $_f$mol% crosslinker mixtures were excluded to help maintain somewhat similar chemistries in the base systems, i.e. all ternary systems, instead of a mixture of ternary and binary copolymers. The T_g values for the six selected base systems along with the three added concentrations (+25, +50, and +75 $_f$mol%) of BPAEDA(512) and pure BPAEDA(512) are shown in Figure 3.6 and the rubbery moduli are shown in Figure 3.7. Both the T_g and the E_r demonstrate a monotonic increase as BPAEDA(512) is added for all of the studied mixtures.

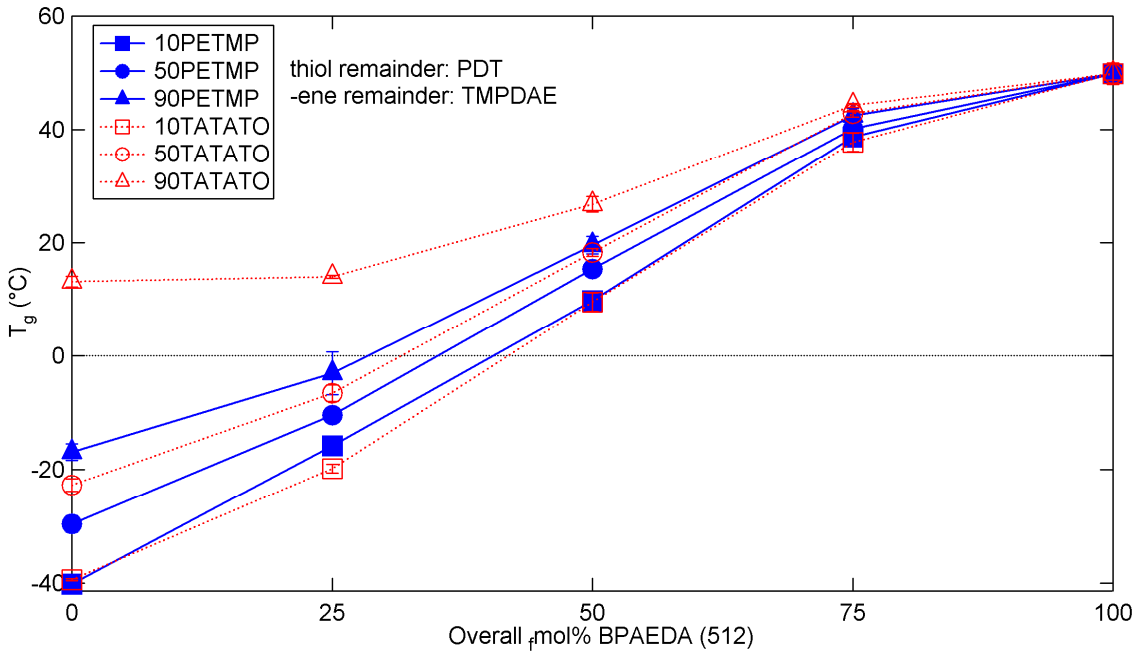

Figure 3.6. Glass transition temperatures for (qua)ternary mixtures of thiol-ene/acrylate mixtures with various concentrations of acrylate added to the base thiol or –ene crosslinked system.

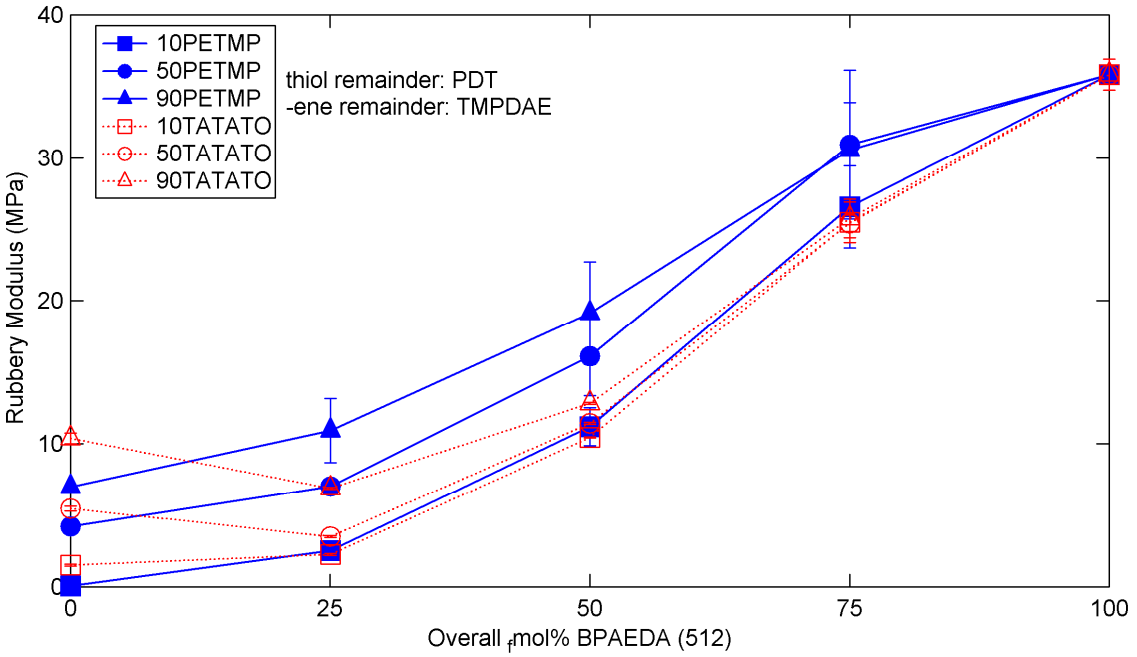

Figure 3.7. Rubbery moduli for (qua)ternary mixtures of thiol-ene/acrylate mixtures with various concentrations of acrylate added to the base thiol or –ene crosslinked system.

The copolymers were characterized with FTIR spectroscopy to determine final conversion of the functional groups in the monomer mixtures. Figure 3.8 shows representative FTIR spectra for a monomer and the resulting polymer with the relevant peaks labeled along with an example area used to determine the conversion, and the conversion calculations for the C=C stretch at 1640 cm^{-1}. Percent conversion was calculated as one minus the ratio of the polymer peak area to the monomer peak area. FTIR was performed for sixteen monomer mixtures, consisting of all six base systems mentioned above, the six base systems +25 $_f$mol% BPAEDA(512) the three PETMP base systems +75 $_f$mol% BPAEDA(512), and pure BPAEDA(512). The thiol groups always converted fully, whereas the C=C stretch band and the allyl band indicated varying levels of conversion depending on the mixture composition.

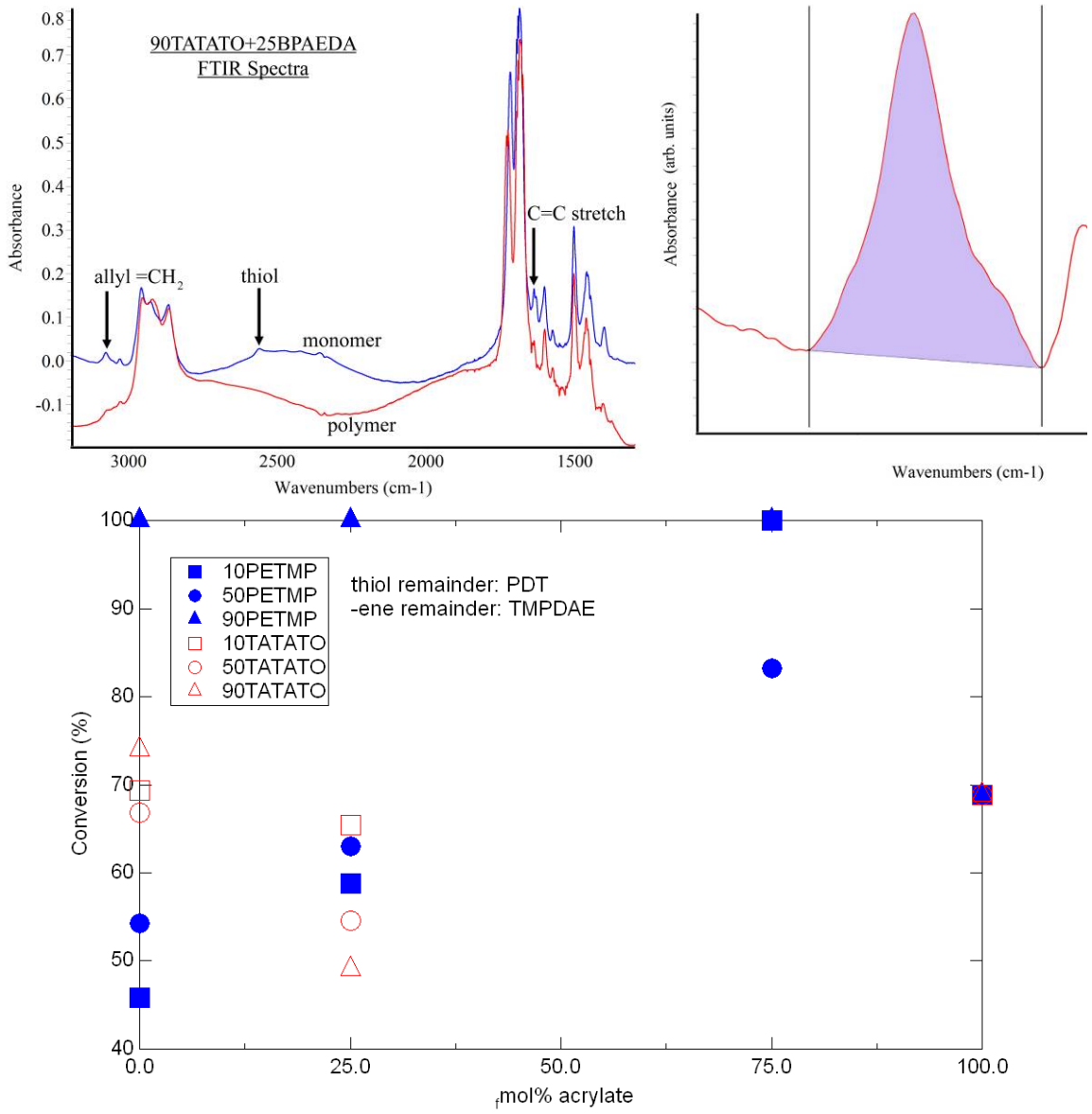

Figure 3.8. (top left) Example FTIR spectra (top right) sample area used for peak calculation and (bottom) C=C conversion for various mixtures.

Sol-fraction mass loss is shown in Figure 3.9. 10TATATO mixtures lost the most mass, followed by 50TATATO mixtures. 90TATATO mixtures lost the least mass. In all three mixture bases, the addition of acrylate resulted in a larger mass loss. 10TATATO lost 11.3% of its initial mass while the addition of the acrylate caused the new mixture to lose 15.6%, a 38% increase in mass loss. 50TATATO lost 2.77% of its initial mass but

50TATATO+25BPAEDA(512) lost 7.87%, a 184% increase. 90TATATO lost 0.80% of its initial mass while the same base mixture with added acrylate lost 3.81%, an increase of over 375%.

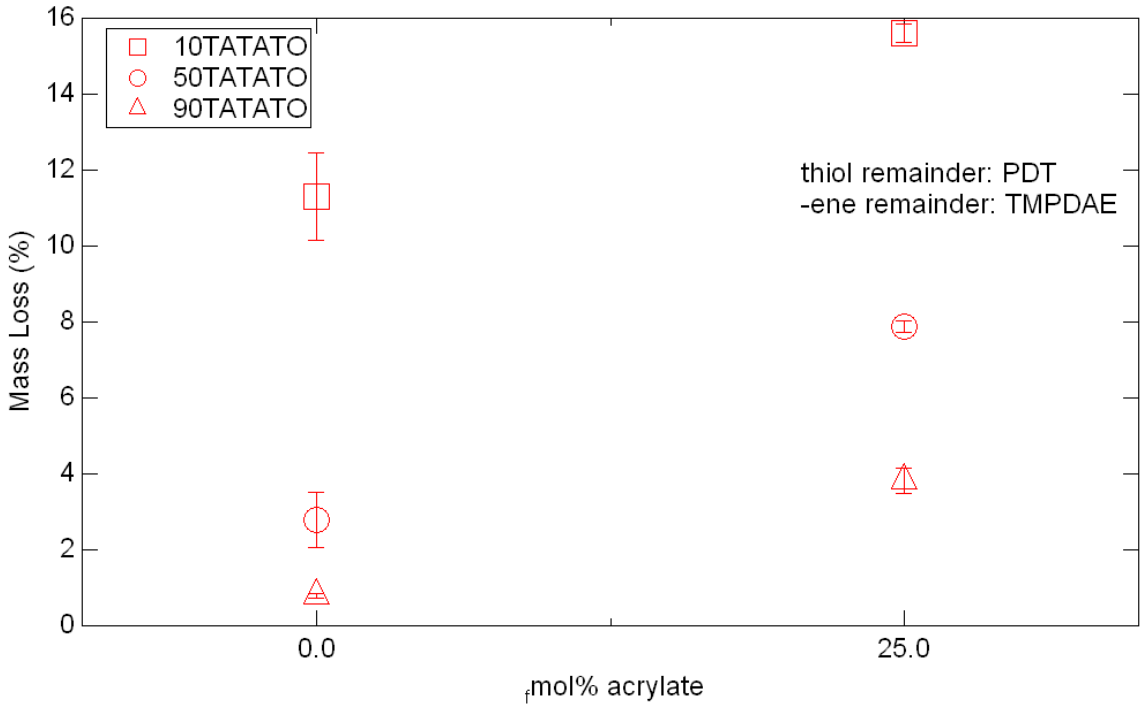

Figure 3.9. Sol-fraction mass loss for six tested mixtures.

The final characterization technique used was mechanical testing of tensile strain-to-failure of the polymers. The compositions tested were the same ones shown in Figure 3.6 and Figure 3.7. Figure 3.10 shows some representative stress-strain curves for the twenty-five selected mixtures. Failure by fracture is denoted by the 'x' in the figure. Figure 3.11 and Figure 3.12 show stress and strain at failure, respectively, for the twenty-five compositions. In general, the failure stress increases as the concentration of PETMP/TATATO and/or BPAEDA(512) increases in the mixture, while the failure strain decreases.

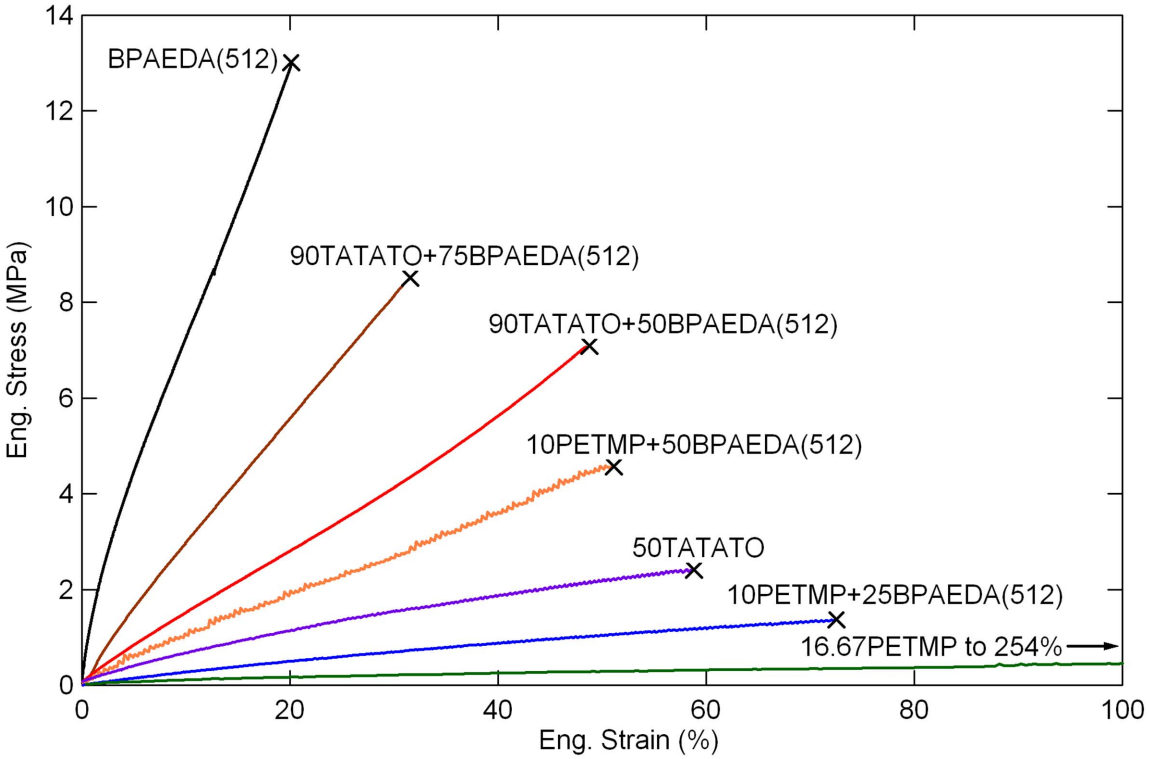

Figure 3.10. Stress-strain behaviors for various thiol-ene/acrylate mixtures.

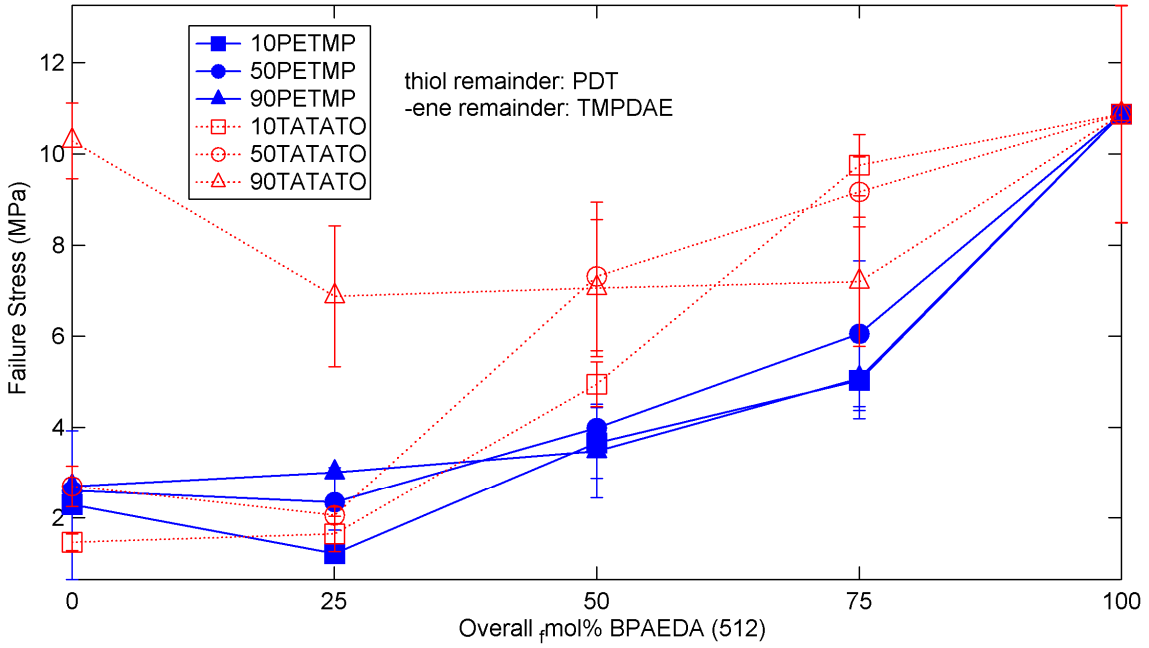

Figure 3.11. Failure stress for (qua)ternary mixtures of thiol-ene/acrylate with various concentrations of acrylate added to the base thiol or –ene crosslinked system.

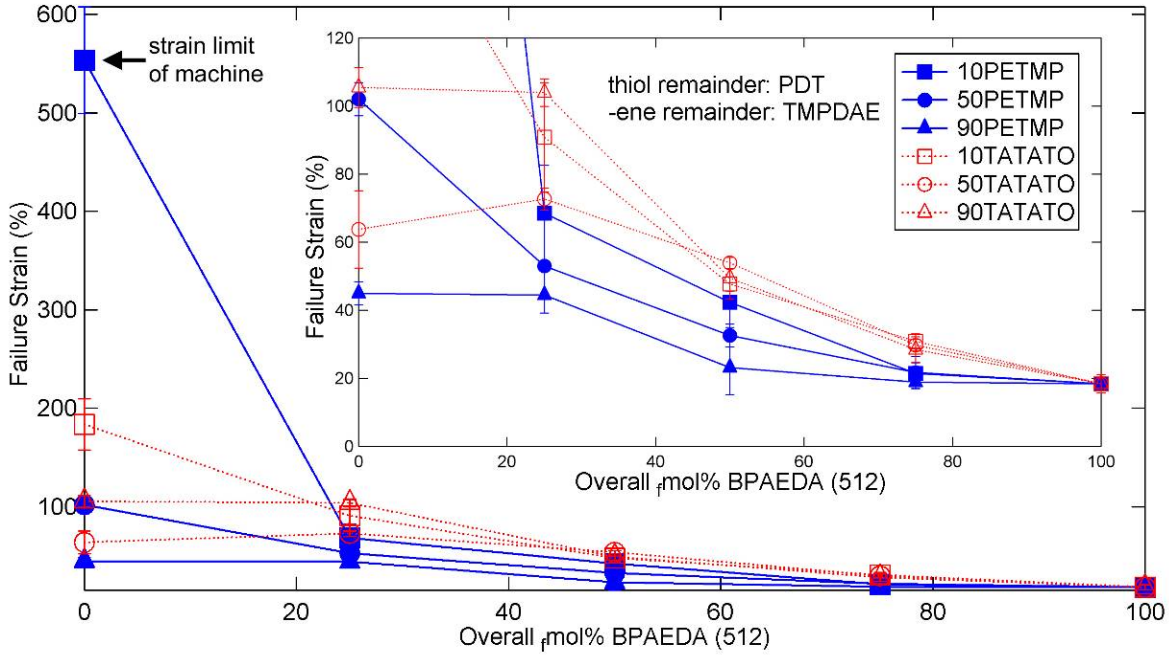

Figure 3.12. Failure strain for (qua)ternary mixtures of thiol-ene/acrylate with various concentrations of acrylate added to the base thiol or –ene crosslinked system. Inset: low strain detail.

3.5. Discussion

As evident in Figure 3.2, copolymers with high concentrations of PETMP behave as a typical thermoset network – a rubbery plateau region featuring a linear increase after reaching the "rubbery modulus" minimum just after the transition. The material labeled 10PETMP behaves as a lightly-crosslinked elastomer at the very verge of the thermoset-thermoplastic limit, featuring a rubbery modulus two orders of magnitude lower than 100PETMP. Compositions featuring lower concentrations of PETMP did not yield materials solid enough for handling, and so were excluded from the study; TATATO-crosslinked mixtures were made with matching crosslinker concentrations so that appropriate comparisons could be made and proper conclusions could be deduced. To determine if there was a PETMP concentration threshold for the switch from the elastomeric behavior of 10PETMP to the thermoset behavior of 20PETMP, two

additional intermediate compositions, namely 13.33PETMP and 16.67PETMP were synthesized and subjected to DMA testing. The results reveal that there was a smooth transition between the two behaviors.

There are two concurrent effects, which contribute to the resulting T_g values of networks formed by various compositions of chemically different monomers, called the "copolymer effect" and the "crosslinking effect." [185-188] The copolymer effect can raise or lower the T_g of a network, depending on the chemical rigidity of the monomers being added and subtracted, with more rigid structures corresponding to a higher T_g [186, 187]. The crosslinking effect, on the other hand, serves solely to raise the T_g as additional chemical crosslink points hinder the mobility of the network. The separation of the two effects is not important for this study since it is the aggregate effect that concerns the networks' behavior, though the magnitudes of the contributions of the two effects for various copolymers have been determined in previous studies [186, 189]. DMA testing reveals that both PETMP and TATATO have a crosslinking effect on the network, though TATATO appears to also exhibit a copolymer effect, as will be discussed further in the following paragraph. The crosslinking effect can be observed in the increases in both the rubbery modulus and the glass transition temperature as the crosslinker concentration is increased (Figure 3.2 to Figure 3.5). Both of these increases can be attributed to an increased crosslink density, and, in the case of TATATO-containing mixtures, to monomer rigidity. Ideal rubber theory [94] states that the rubbery modulus is inversely proportional to the average molecular weight between crosslinks

($\overline{M}_c$), or directly proportional to the crosslink density, and this has been demonstrated to hold true for non-ideal (meth)acrylate networks as well [93].

As shown by Figure 3.4 and Figure 3.5, at the same concentration of crosslinking agent, TATATO-containing mixtures have a higher T_g and E_r than PETMP-containing mixtures. This can be expected given the structures of the crosslinkers – TATATO has a lower molecular weight per functional group and fewer functional groups per molecule than PETMP, and TATATO has a 6-membered ring core structure whereas PETMP consists of four longer, flexible "arms" connected at the center. The TATATO structure, therefore, will both increase T_g due to its core rigidity and raise rubbery modulus more than PETMP due to lower $\overline{M}_c$ at the same functional group concentration. Another contributing factor to TATATO mixtures' exhibition of higher T_g's and E_r's than those exhibited by PETMP mixtures (which is more evident at higher crosslinker concentrations as the properties diverge further) stems from the necessity for thiol and –ene functional group equivalence. As either crosslinker is added, some difunctional monomer with the same functional group must be removed in proportion. Thus, as PETMP concentration increases in the mixtures, PDT concentration is reduced; as TATATO concentration increases, TMPDAE concentration decreases. PDT is replaced by a more flexible PETMP molecule, but this flexibility is counterbalanced by PETMP crosslinking and resulting network hindrances. TMPDAE, itself more flexible than PDT due to its larger number of unhindered bonds between functional groups, is replaced by an even stiffer cycle-cored TATATO - which has fewer bonds between functional groups in addition to acting as a crosslinker. Therefore, the trends, difference, and divergence of

the properties of the two ternary mixture types shown in Figure 3.4 and Figure 3.5 can be explained when one considers that in PETMP mixtures the less flexible difunctional monomer is replaced by a more flexible crosslinker, while in TATATO mixtures the more flexible difunctional monomer is replaced by the least flexible monomer (which also acts as a crosslinker).

Except for 100TATATO, all of the ternary mixtures have T_g values which, being subambient, render such materials incapable of functioning in typical off-the-shelf shape memory applications. To remedy this situation[†] and increase the application space for these copolymers, a high-T_g monomer was added in the form of BPAEDA(512). However, the addition of BPAEDA(512) leads to a conflict in terms of E_r and T_g. A high T_g is desired so that the deformed state of the shape memory device is stable under ambient conditions, but a low E_r is desired since a low modulus generally translates to a larger deformation limit [93]. A low E_r would further increase the customizability of the network because the stress-strain behavior could be tuned by the introduction of different monomer chemistries. In the thiol-ene mixture, the acrylate can homopolymerize, adding a step to the reaction scheme shown in Figure 1.4. BPAEDA(512) can act as an -ene and react with a thiol radical, thereby competing with TMPDAE and/or TATATO. Additionally, primary radicals from DMPA can initiate the BPAEDA(512) and create a carbon-centered acrylate radical. In either case, the carbon-centered acrylate radical can

[†] Efforts in this work to raise T_g using stiffer difunctional monomers, without excessive crosslinking (highly crosslinked shape memory polymers do not demonstrate adequate deformation levels), were unsuccessful and require further study.

then abstract a hydrogen and propagate the thiol-ene reaction, or it can initiate more BPAEDA(512), forming a carbon-backbone acrylate chain.

The incorporation of BPAEDA(512) via the thiol-ene reaction raises the T_g of the polymer by the copolymer effect since BPAEDA(512) simply acts as a linear chain "extender," while the homopolymerization route raises T_g and E_r by both the copolymer and the crosslinking effect. Figure 3.6 and Figure 3.7 show these anticipated effects when BPAEDA(512) is added. The drop in E_r in the TATATO+25BPAEDA(512) quaternary mixtures compared to the acrylate-less ternary TATATO mixtures is most likely a plasticization effect caused by the larger amounts of dangling chain ends and residual monomer, which is confirmed by FTIR scans of the mixtures showing a lower conversion of –ene groups (Figure 3.8). Larger reductions in E_r for these six mixtures correspond to greater drops in the overall C=C bond conversion. In the mixtures where TATATO is the crosslinker and BPAEDA(512) is added, the vinyl groups from the two monomers compete for reaction with the thiol groups, so some residual monomer is expected, given the competitive reaction scheme. The effects of this competition are most prevalent in the TATATO+25BPAEDA(512) mixtures because of the relatively low concentration of acrylate groups. Mixtures with higher concentrations of BPAEDA(512) have a significantly larger amount of pure acrylate network within the copolymer, simply because of the relative scarcity of thiol groups available for the typical thiol-ene reaction. These mixtures with larger acrylate networks certainly have some residual monomer and dangling chain ends, but these are percentagewise much smaller and so exert less of a negative effect on the resulting network properties than in the +25BPAEDA(512) copolymers.

Sol-fraction testing was used to determine the amount of soluble monomer that could be extracted from the networks based on the conversion data from FTIR. However, it was found that impurities dominated the response of the networks instead of overall conversion. As can be seen from a comparison of the pure base mixtures (0 $_f$mol% acrylate) in Figure 3.9, mixtures with larger amounts of TMPDAE showed increased mass loss over those with larger amounts of the TATATO crosslinker. This increased mass loss is most likely the non-participating impurities associated with the TMPDAE monomer, which is only 90% pure as-received, while TATATO has a purity of 98%. However, the addition of acrylate to all of these systems increases the mass loss due to additional unconverted monomer being extracted, in agreement with the reduced conversion detected by FTIR. Large percentagewise increases in mass loss correlate well with large drops in conversion and large reductions in E_r. FTIR analysis cannot detect the presence of the non-participating impurities at the selected wavenumbers of interest, so the reverse order of the mass loss magnitudes for +25$_f$mol% acrylate compared to C=C conversion further supports the theory that impurities dominate the materials' sol-fraction behavior.

It is interesting to note that the mass loss from sol-fraction testing shows an inverse relationship with rubbery modulus, since higher mass losses are associated with lower rubbery moduli, or lower crosslink densities (and larger network openings). It is plausible that some unconverted bonds are termini for oligomers of various sizes, the larger of which cannot fit through the tighter networks. Alternatively, it is possible that many of the unconverted bonds detected by FTIR are on pendant, but attached chains which are not soluble but do not contribute to the network strength. However, without

any further characterization of the eluent, it is difficult to conclude if the inverse relationship between mass loss and E_r truly exists or is merely an artifact of the increased impurity level associated with increased amounts of TMPDAE.

The stress-strain behavior of some sample mixtures is shown in Figure 3.10, where failure by fracture is denoted by an x. The stress and strain at failure for the tested mixtures are summarized in Figure 3.11 and Figure 3.12. 10PETMP stretched the entire length of the thermal chamber and reached equipment limits before failure, further confirming its large strain behavior. The other base mixtures exhibited trends in strain and stress at failure which are consistent with results concerning (meth)acrylate networks [93], which found that higher concentrations of crosslinker reduce strain at failure but increase stress at failure. This behavior can be explained by considering the crosslink density, as implied by the DMA data discussed previously. Higher concentrations of crosslinker restrict the macromolecular motion of the network but increase the network's load-carrying capacity. Additionally, increased crosslink density generally means increased network heterogeneity [93, 188, 190], and with heterogeneity comes increased probability of a stress concentration arising due to a densely crosslinked area, causing a premature failure as compared to an ideally homogeneous network with the same overall crosslink density. The deviation of the 90TATATO and 90TATATO+25BPAEDA(512) from the trends in stress and strain at failure can be attributed to the structure of TATATO. Both of these copolymers have rubbery moduli below about 10 MPa, which was determined by Safranski et al. [84] to be a threshold below which monomer chemistry plays a strong role in the (meth)acrylate network toughness and stress-strain behavior. They demonstrated that ringed members within a monomer allow the polymer

to exhibit much higher toughness characteristics than polymers lacking rings; with the inclusion of a large amount of ring-cored crosslinker in 90TATATO and 90TATATO+25BPAEDA(512), the enhanced strength and deformation characteristics can be expected.

Since strain and stress at failure are strongly related to the network structure and the density of crosslinking, it is instructive to graph these against the molecular weight between crosslinks $\overline{M}_c$, which is proportional to T/E_r. Figure 3.13 and Figure 3.14 show these data along with data from Ortega et al. [93], where T represents the temperature at which E_r is measured. The trend for strain vs. $\overline{M}_c$ is nearly linear, which agrees with previous results peroxide-vulcanized rubbers by Morell and Stern in Treloar [94]. Additionally, these data also correspond quite well with the data from Ortega et al. [93] concerning (meth)acrylate networks, in which the data were also obtained by deforming the samples at a temperature at the peak of tan(δ). The data for stress vs. $\overline{M}_c$ also corresponds very well with that from the (meth)acrylate study. This indicates that though there are important chemical implications as a result of the difference in the polymerization reactions, the overall mechanical effect of crosslinking a polymer results in similar system behaviors at T_g – highly crosslinked (low T/E_r) polymers have a higher stress at failure due to the increased load carrying capacity of the crosslink points while lightly crosslinked materials (high T/E_r) have little strength but significant deformability.

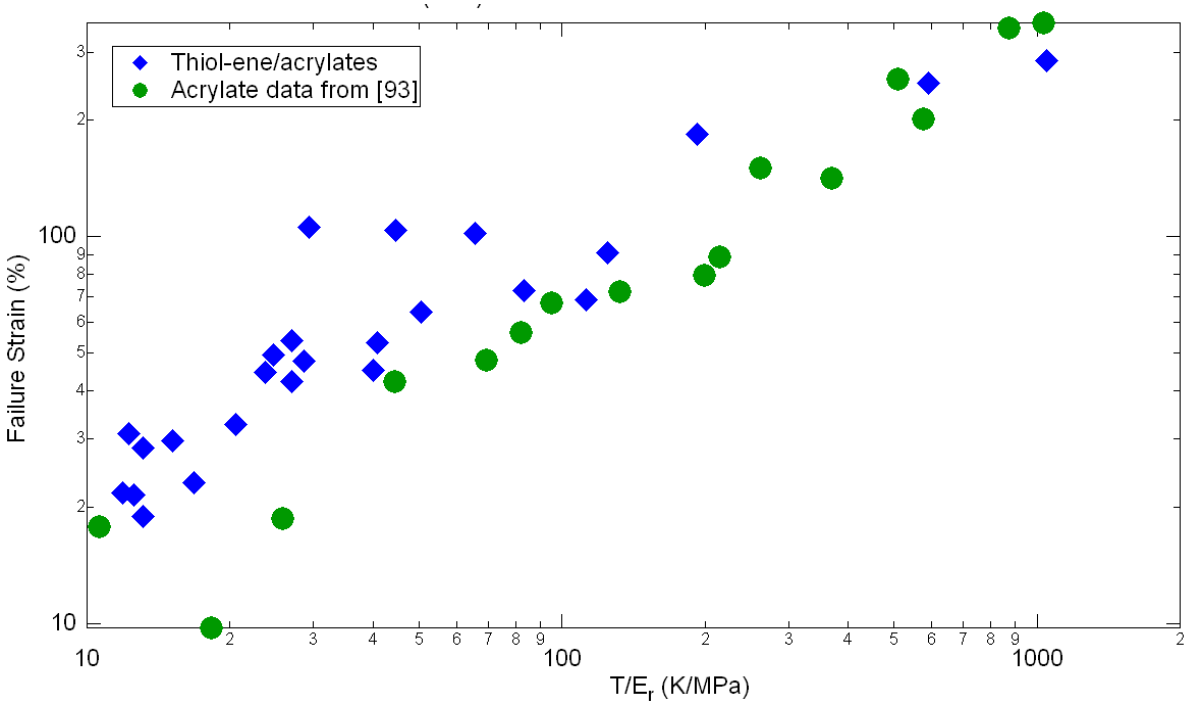

Figure 3.13. Failure strain versus "molecular weight between crosslinks" following results of reference [93] for (qua)ternary mixtures of thiol-ene/acrylate with various concentrations of acrylate added to the base thiol or –ene crosslinked system.

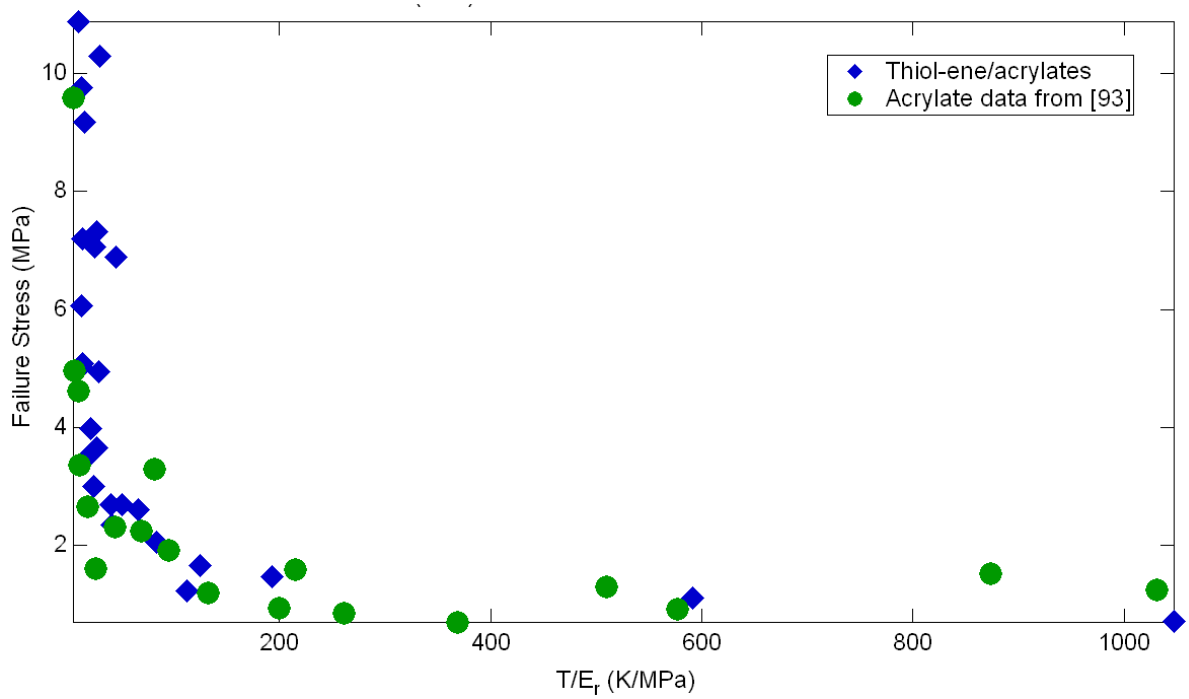

Figure 3.14. Failure stress versus "molecular weight between crosslinks" following results of reference [93] for (qua)ternary mixtures of thiol-ene/acrylate with various concentrations of acrylate added to the base thiol or –ene crosslinked system.

Figure 3.15, plotting strain at failure vs. E_r, highlights a major optimization tradeoff inherent to polymer design – the nonlinear and diminishing sensitivity of failure strain to rubbery modulus. Similar to the results from the (meth)acrylate study [93], strain at failure at low crosslink densities (or low E_r) is highly sensitive to rubbery modulus, but at higher modulus values the failure strain value changes much less. For example, an increase of the rubbery modulus from ~0.5 MPa to ~2.5 MPa results in a reduction of strain at failure from about 250% to about 100%, but an increase of the rubbery modulus from 10 MPa to 12 MPa results in minimal change in strain to failure.

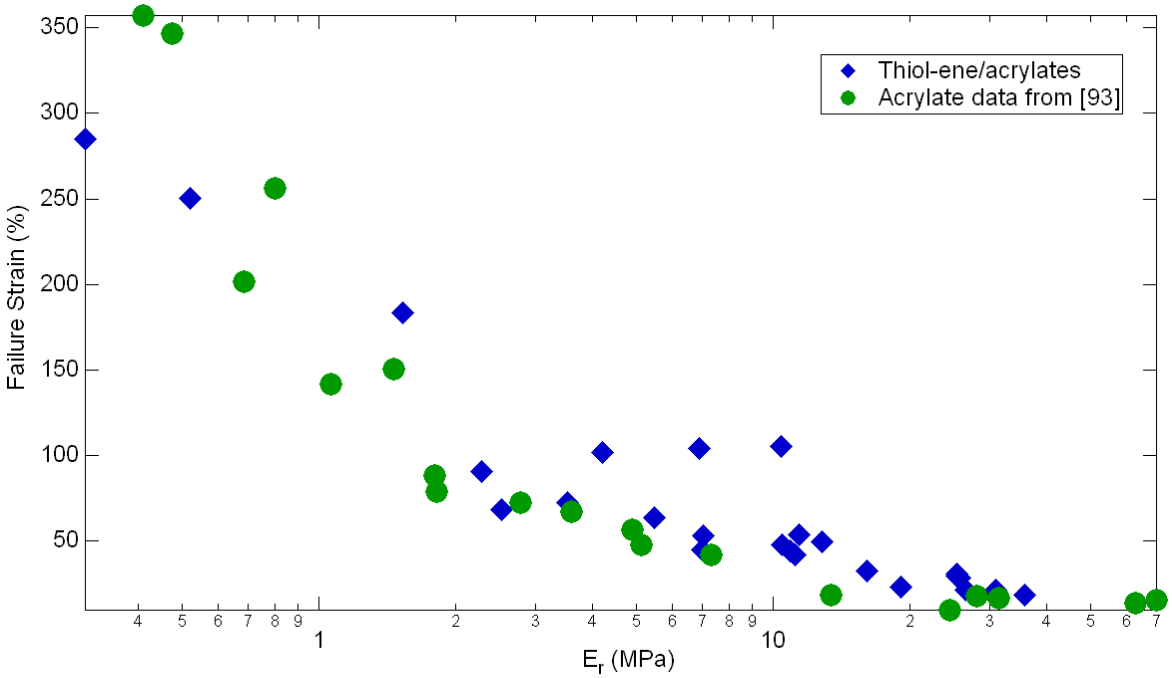

Figure 3.15. Failure strain versus rubbery modulus following results of reference [93] for (qua)ternary mixtures of thiol-ene/acrylate with various concentrations of acrylate added to the base thiol or –ene crosslinked system.

3.6. Conclusions

Thiol-ene polymers are a versatile class that can incorporate acrylates to gain some of the benefits of acrylates while simultaneously avoiding some of the drawbacks of acrylates. The copolymer systems studied herein exhibited a broad range of tunable thermomechanical properties, such as T_g (-40 to 43 °C), E_r (<0.1 to 35 MPa), and failure strain (20% to >500%). Dynamic mechanical analysis revealed that the addition of thiol or –ene crosslinker increased T_g and E_r. Copolymers exploiting TATATO as a crosslinker exhibited higher T_g and E_r values than those with PETMP at the same concentration of crosslinker functional groups, due to the difference in the chemical structures.

The addition of BPAEDA(512) increased T_g and E_r due to both the copolymer and the crosslinking effect, except for three TATATO+25 $_f$mol% BPAEDA(512) mixtures. These three mixtures exhibited lower E_r values due to dangling chains, the plasticization effect of residual monomer, and the competition of BPAEDA(512) and TATATO for thiyl radicals as confirmed by FTIR studies. FTIR spectroscopy shows that the addition of BPAEDA(512) to the mixture results in some unconverted –ene functional groups. The strict requirement for functional group equivalence in thiol-ene polymers is a limitation that can, to some degree, be alleviated by the addition of a homopolymerizing –ene such as an acrylate. Kinetic studies of the reaction can reveal the precise ratio of thiol:ene:acrylate needed to eliminate virtually all unreacted monomer.

Sol-fraction testing elucidated the probable dominance of impurities on mass loss in solvent, but further testing is necessary for full characterization. Swelling behavior can

describe the amount of pendant unreacted chains present in the network as compared to bonds on extractable and mobile monomer or oligomer. Additional elemental analysis, such as nuclear magnetic resonance (NMR), of the related eluents could help determine the fraction of extracted monomer/oligomer as compared to impurities present, assuming that the impurities in the TMPDAE monomer could be characterized or determined based on the production reaction scheme.

Higher crosslink densities, caused by large concentrations of BPAEDA(512) and/or PETMP/TATATO, generally result in higher stress and lower strain at failure as determined by tensile testing at T_g. These tensile results are in strong agreement with previous studies performed on (meth)acrylate systems. This work shows that various desired thermomechanical properties can be obtained by careful selection and mixing of various thiol-ene and acrylate monomers, but there are certain boundaries and tradeoffs that must always be taken into consideration.

The thermomechanical behavior of thiol-ene/acrylates and (meth)acrylate systems have excellent agreement at their respective T_g's and (meth)acrylate systems cover a broad range of achievable T_g values. Additionally, the mechanical properties of the two system types are quite similar at equivalent crosslink density. Therefore, future studies will investigate the other purported benefits of thiol-ene/acrylates as compared to (meth)acrylates to determine whether thiol-ene/acrylate systems occupy an application space that is outside the realm of (meth)acrylate systems' capabilities.

CHAPTER 4. PHOTOPATTERNING OF THIOL-ENE/ACRYLATES

4.1. Summary

The previous chapter covered the investigation of the structure-to-thermomechanical property relationship for bulk thiol-ene(/acrylate) copolymers. The next research step was to determine whether the reported benefits of the thiol-ene step reaction, such as low shrinkage, would translate into high fidelity pattern transfer for thiol-ene/acrylate materials with tunable mechanical properties and low-to-moderate crosslinking. Current common photoresists and photolithographic polymers are materials designed for their photocuring properties instead of their mechanical properties. However, the limited range of mechanical properties that result restrict the design and application space for non-silicon-based microdevices. Thiol-ene/acrylates copolymers are materials which exhibit a unique blend of properties which could make them suitable for photolithography while maintaining mechanical property tunability. Five thiol-ene and acrylate monomer blends were compared in a photopolymerization rate study tracking heat flow, while dynamic mechanical analysis was performed on two thiol-ene acrylate system and one binary acrylate blend. Factorial design photopatterning studies with photomasks were performed on the two exemplar thiol-ene acrylate systems and compared to that of the binary acrylate which is thermomechanically equivalent to one of the thiol-ene/acrylate exemplars. The thiol-ene/acrylate exemplars showed rapid polymerization, low-to-moderate shrinkage and low heat evolution with excellent patternability; the equivalent binary acrylate showed extreme shrinkage and did not replicate the mask pattern in a controllable fashion.

4.2. Introduction

Photolithography using patterned transparent/opaque masks is standard practice in the semiconductor industry for the fabrication of integrated circuits and printed circuit boards [40, 41, 191] and has emerged as a popular technique for the creation of complex microscale structures for direct polymer microdevice fabrication [192-201] or for sacrificial photoresist patterning for non-polymeric microdevices and microelectromechanical systems [40, 41, 201-207]. (Meth)acrylates are one of the most commonly used polymers in photolithography [201, 208, 209]. The (meth)acrylates typically used for photolithography are highly branched [210-213], incorporate fillers of some form [214, 215], or are mixed with other non-(meth)acrylate monomer solutions [216], because these types of systems exhibit high polymerization rates and low shrinkage. The rapid polymerization and low shrinkage of the highly branched (meth)acrylates in particular is a result of the high concentration of functional groups present in the monomer solution. This high concentration leads to high final crosslink densities, which, in turn, limits the range of achievable properties for these polymers; the polymers are typically glassy or very stiff rubbers. Acrylates with lower functionalities (i.e. mono- and di-), which are typically used in mixtures to adjust the polymer's thermomechanical properties, have notoriously poor micropatternability due to much higher shrinkage magnitudes than those of more highly functionalized monomers, and they polymerize relatively slowly [217]. Seminal works on the photopatterning of hydrogels [218, 219] show that lightly crosslinked (meth)acrylate networks can be patterned moderately well at the scale necessary for their application, though the monomers were specifically chosen for their low polymerization shrinkage and not for

their thermomechanical properties. A more commonly used methacrylate hydrogel material chosen for its behavior in solution does not pattern as well at smaller scales [218, 220].

Typical photoresist materials, such as the widely used negative-tone epoxy photoresist SU-8, are highly crosslinked [213, 221] and/or are commercially available materials with little customizability [202, 222-224]. These photoresists typically require a long and complicated set of steps for preparation prior to and post-exposure to develop the desired structures [191, 213], the resolution of which are very sensitive to the preparation parameters. Direct fabrication of microdevices with hyperbranched acrylates can be performed up to eight times faster than with typical negative-tone photoresists, such as SU-8, and the resultant acrylate structures can have an internal stress 3-8 times lower than those composed of photoresist; the higher internal stress in the photoresist can result in corner cracking and delamination [213].

Unlike the (meth)acrylate polymerization reaction, the thiol-ene reaction is a free-radical, step-growth polymerization reaction [2, 19, 21-23, 25, 97]. Since it is a free-radical scheme, it benefits from the ability to be performed at ambient temperatures, at low cost, rapid and solvent-less polymerization, and can be spatially and temporally controlled [25, 45-55]. Due to the step-growth nature of the thiol-ene reaction, these materials exhibit less shrinkage, a later gel point, and reduced residual internal stress as compared to typical (meth)acrylate networks, which are created by chain-growth reactions. Furthermore, the thiol-ene reaction exhibits the distinctive capability to cure rapidly

without photoinitiator and the reaction has shown limited susceptibility to oxygen inhibition [13, 97, 98].

The materials studied and suggested herein can be adapted to various photolithography techniques including standard photomasking techniques [191] and two-photon stereolithography [125, 126, 147, 225]. As has been suggested by Cramer et al. [197, 198], these materials can be used in the CLiPP multilayer photomask-based polymer microdevice fabrication process; the iniferter-mediated "living" thiol-ene polymerization reaction necessary for CLiPP has been studied [25] and some basic macroscale photolithography was demonstrated. Additionally, the materials studied herein are merely representative of thiol-ene/acrylates, a larger class of photopatternable copolymers. Many other potential photopatternable thiol-ene(/acrylate) copolymers were investigated in the previous chapter. It was demonstrated that thiol-ene/acrylates were substantially thermomechanically equivalent to (meth)acrylate networks. The research discussed in this chapter aimed to determine the attractiveness of thiol-ene/acrylate copolymers over pure(meth)acrylate networks for photopatterning at small scales, which results from the difference in the polymerization reaction schemes.

4.3. Experimental

For clarity of presentation, the polymer composition is centered around the equivalence of functional groups and is broken into two parts – the thiol functional group component, $t_f$mol%, and the –ene functional group component, $e_f$mol% - each totaling 100% and insuring a stoichiometric ratio of the functional groups. In the quaternary mixtures, acrylate functionalities, $a_f$mol %, was added to the thiol-ene base system such that the

overall concentration of acrylate functional groups is indicated by the number preceding the acrylate name. 2,2, dimethoxy-2-phenylacetophenone (DMPA) acted as the photoinitiator in all of the mixtures, including the quaternary mixtures, at a concentration of one initiator molecule per 1,000 –ene *and* acrylate groups (+0.1 e_f+$a_f$mol%). The only exception is that DMPA was used at a concentration of 0.1 wt% for the Sartomer monomer. All materials were obtained from Sigma Aldrich and were used as received.

Initial screening studies were performed with a standard benchtop UV source to determine the ability of this material to be photopatterned, especially as compared to equivalent (meth)acrylate networks. The experiments based on the initial screening studies were designed as 2^3 factorial experimental series, described more fully below. The important input parameters for the experiments were exposure time, layer thickness, and development time. The selected developer was acetone because the monomer mixtures were partially insoluble in other common solvents, such as ethanol, methanol, and 2-propanol.

4.3.1. Materials

The materials used in this study (Figure 4.1) consisted of several pure monomers, as well as two quaternary thiol-ene/acrylate mixtures and one binary acrylate mixture. The pure materials were SR9020 (Sartomer Corp.), BPAEDA(512), and PEGPEA(236). The binary acrylate mixture was designed to be thermomechanically equivalent to 50TATATO+50BPAEDA(512) and was composed of 30.2 $a_f$mol% (31.9 wt%) BPAEDA(512) and 69.8 $a_f$mol% (68.1 wt%) PEGPEA(236). The BPAEDA(512) component was kept from the other mixtures to maintain some level of chemical

consistency among the different copolymers, and a binary system was chosen for simplicity. The PEGPEA(236) was chosen for its thermomechanical properties. The compositions of the thiol-ene/acrylate mixtures are listed in Table 4.1.

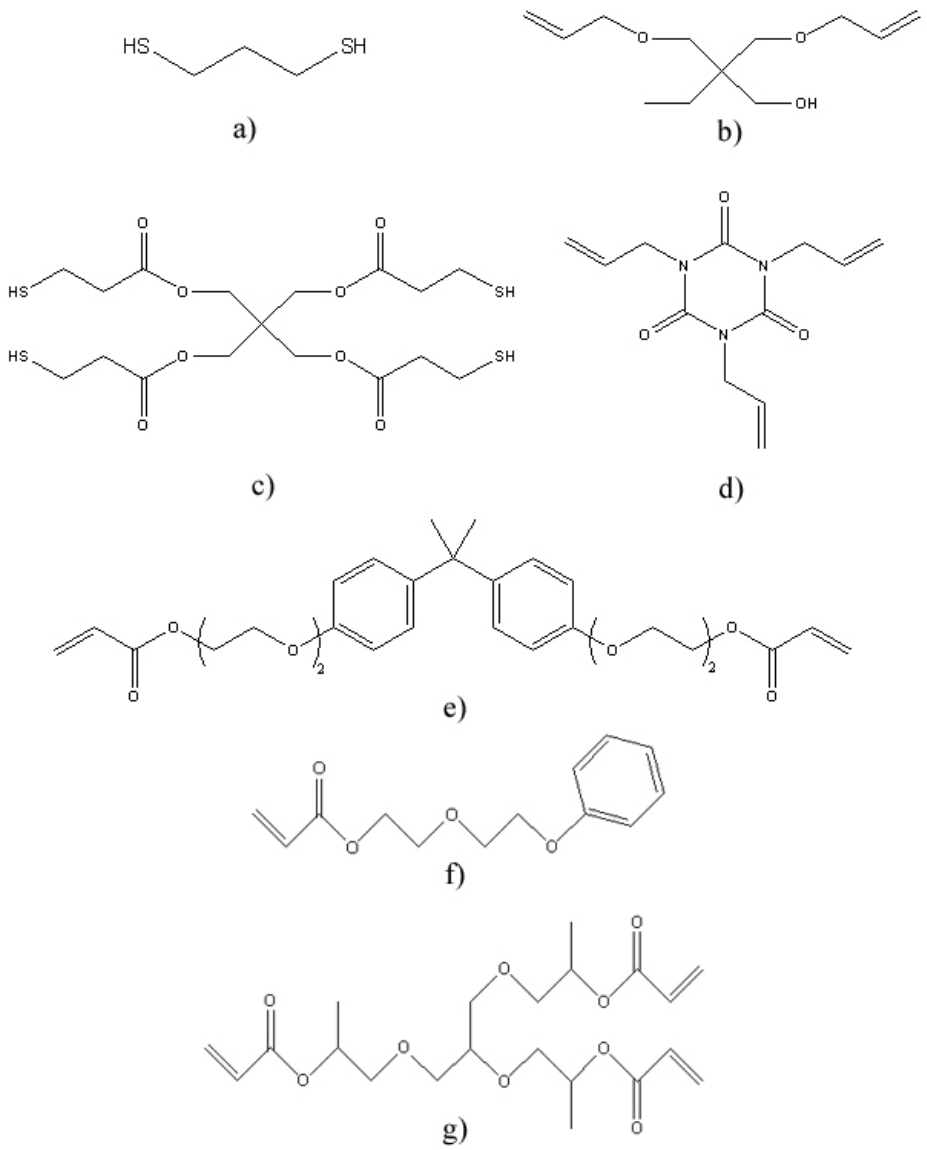

Figure 4.1. Chemical structures of studied monomers.
a) 1,3-propanedithiol (PDT), b) trimethylolpropane diallyl ether (TMPDAE), c) pentaerythritol tetrakis(3-mercaptopropionate) (PETMP), d) 1,3,5-triallyl-1,3,5-triazine-2,4,6(1H,3H,5H)-trione (TATATO), e) Bisphenol A ethoxylate diacrylate, M_n 512 (BPAEDA(512)), f) poly(ethylene glycol) phenylether acrylate, M_n 236 (PEGPEA(236)), g) SR9020

Table 4.1. Thiol-ene/acrylate mixtures used in study.

		$t_f$mol%		$e_f$mol%		$a_f$mol%
Mix	Mix Name\Chemical	PDT	PETMP	TMPDAE	TATATO	BPAEDA(512)
1	10PETMP+25BPAEDA(512)	90	10	100	-	+25
2	50TATATO+50BPAEDA(512)	100	-	50	50	+50

4.3.2. Methods

Polymer sheets were created by injecting monomer solution into a mold consisting of two 50 mm x 75 mm slides separated by 1 mm spacers and secured with binder clips and exposing the mold to a UVP Blak-Ray® 365nm UV light (intensity ~4-8 mW/cm^2) for 5 minutes. Prior to injection, the slides were thoroughly cleaned with acetone. A minimum of three sheets (or slides) of each mixture were polymerized.

Samples for dynamic mechanical analysis (DMA) were obtained by excising a portion of the polymerized sheet with a razor blade and polishing the edges with 800- and then 1200-grit silicon-carbide sandpaper, to arrive at final specimen dimensions of approximately 20 mm x 4.5 mm x 1 mm. A TA Instruments Q800 DMA was used to obtain the storage modulus (E') and loss tangent (tan δ) curves in tensile mode. The samples ($n \geq 2$) were cooled to -100 ºC, equilibrated for 2 minutes, and then ramped at a rate of 2 ºC/min to 120 ºC. The frequency was set to 1 Hz, the force track was set to 150%, and the strain level was set to 0.1%. The glass transition temperature, T_g, was determined by the peak of the tan(δ) curve and the rubbery modulus, E_r, was defined as the minimum of the storage modulus curve.

A TA Instruments differential scanning calorimeter (DSC100) with a photocuring assembly (PCA) was used for polymerization speed studies. An Exfo Novacure 2100

exposure system provided the ultraviolet radiation via a dual 5 mm diameter light guide. The intensity was tuned to 8 mW/cm^2 to mimic the conditions under the Blak-Ray lamp used for DMA and initial photopatterning studies. A sample pan was placed on the sample pedestal and one drop (~15 mg) of monomer solution was pipetted into the pan. The reference pedestal was left empty to allow the contribution of incoming energy from the light source to be removed from the heat flow calculations. The sample chamber was closed and purged with nitrogen to eliminate any oxygen that might inhibit the polymerization reaction. The experiments were performed under isothermal conditions at 25 °C with a constant nitrogen purge rate of 5 mL/min. After two minutes of purging the chamber, the light source shutter was opened and the heat flow due to the exothermic polymerization reaction was tracked until the heat flow was less than 0.1% of maximum heat flow. Post-exposure, the mass of the resultant polymer was obtained and used to normalize the heat flow data. The data for conversion percentage is normalized to the maximum conversion (area under the mass-normalized heat flow vs. time curve) attainable by each individual mixture in the photoDSC, not to the full conversion of all the bonds in the mixture.

The hard contact method (direct liquid contact) was used for the micropatterning experiments. Patterned polymers were created by injecting the desired monomer solution between the borosilicate glass substrate and the photomask, which were separated by spacers. The spacers were precision steel shims with thicknesses either 76.2 μm or 508 μm, and were used to control the monomer layer thickness and the thickness of the resulting polymer structures. The photomask was either a photofilm [203] (UV-opaque ink on a flexible, transparent polymer sheet with a resolution of 5 μm) or a chrome-on-

soda lime photomask with a resolution of 5 μm. For the initial screening studies, the micropatterning setup was then exposed to a UVP Blak-Ray® 365nm UV light (intensity ~8 mW/cm^2) for 10 to 30 seconds, depending on the desired conditions. Post-exposure, the structures were developed in acetone for 10-60 seconds.

Two 2^3 factorial design experiment matrices [226] were designed, with the first stage (Table 4.2) being a well-controlled screening study where the parameters were chosen from previous screening studies without a collimated source. The second stage matrix (Table 4.3) was designed based on the results of the first stage screening experiments. The samples were prepared in the same fashion as in the screening studies, except that the samples were placed in low density polyethylene specimen bags (thickness 101.6 μm) to reduce the smell from the thiol component in the cleanroom environment where the experiments took place. These experiments were performed using an Optical Associates Inc. 300 series mask aligner, with the experimental conditions as listed in Table 4.2 and Table 4.3. The intensity of the light source at 365 nm was 13.3 mW/cm^2, but the specimen bag reduced the intensity by ~10% to 11.9 mW/cm^2.

Table 4.2. 2^3 factorial design experiment matrix for screening study.

Test #	Thickness (μm)	Dose (mJ/cm^2)	Development (sec)
1	508	144	60
2	76.2	144	60
3	508	72	60
4	76.2	72	60
5	508	144	30
6	76.2	144	30
7	508	72	30
8	76.2	72	30

Table 4.3. 2^3 factorial design experiment matrix for second-level study.

Test #	Thickness (μm)	Dose (mJ/cm^2)	Time (sec)
1	508	85.5	75
2	76.2	85.5	75
3	508	58.5	75
4	76.2	58.5	75
5	508	85.5	45
6	76.2	85.5	45
7	508	58.5	45
8	76.2	58.5	45

An optical microscope was used to examine and characterize the final polymer structures. Optical micrographs of the structures were used to determine the ability of the copolymer to be photopatterned and to determine the main and interaction effects of the various conditions from the 2^3 factorial design study. Micrographs of the photomasks/films were used as controls for sizing and geometry. A Hitachi S-3500H SEM was used for additional images of oblique views of the structures and for sidewall profile determination. Samples were prepared for the electron microscope by sputter coating with a thin (15-30 nm) layer of gold. The image processing software ImageJ from the National Institutes of Health [227] was used to determine quantitative values for various features of the polymer structures based on images from both optical and electron microscopy.

4.4. Results

DMA testing revealed (Figure 4.2) that 50TATATO+50BPAEDA(512) had a T_g of 18.3 °C and an E_r of 11.43 MPa. The binary acrylate system 30.2BPAEDA(512)69.8PEGPEA(236) had a T_g of 17.6 °C and E_r of 13.13 MPa. The 10PETMP+25BPAEDA(512) mixture had a T_g of -16 °C and E_r of 2.5 MPa.

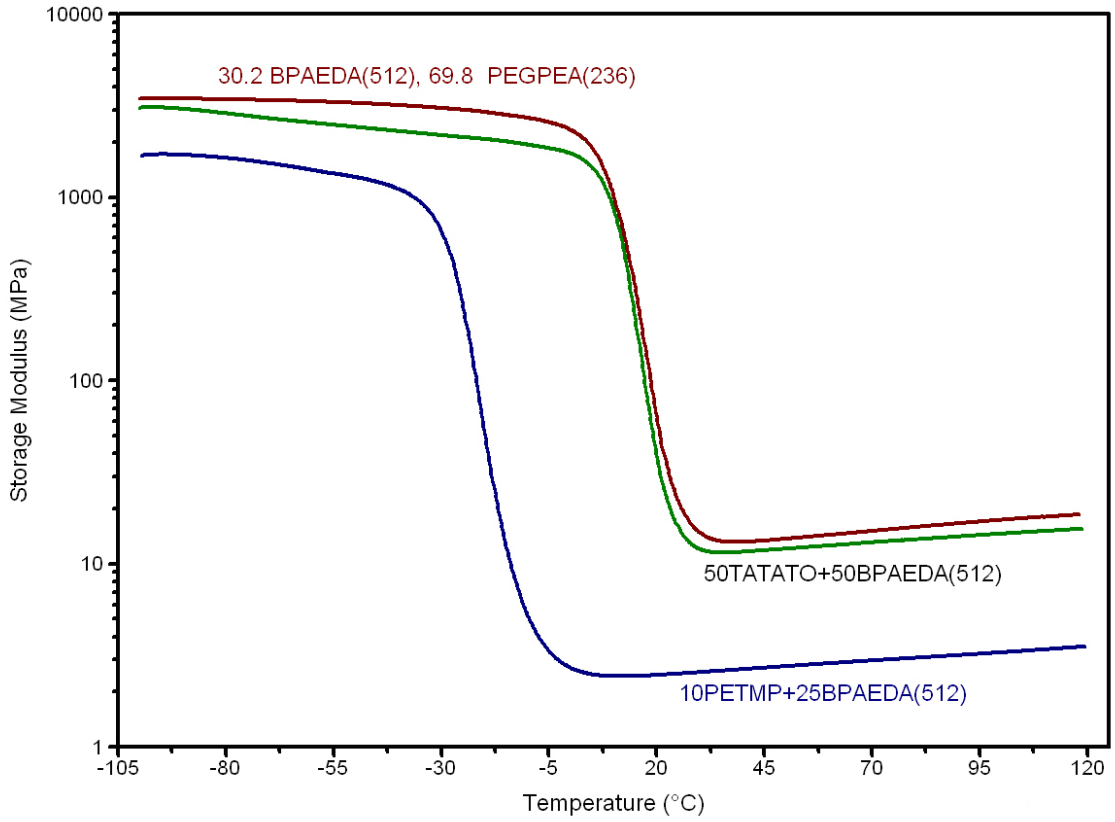

Figure 4.2. DMA curves for 50TATATO+50BPAEDA(512), 30.2BPAEDA(512)69.8PEGPEA(236) and 10PETMP+25BPAEDA(512).

PhotoDSC testing of the different monomers, as seen in Figure 4.3 and Figure 4.4, revealed the exotherm of the polymerization reaction and normalized conversion speed for each material. The total heat flow for the tested materials (n=3) is listed in Table 4.4 in descending exotherm magnitude.

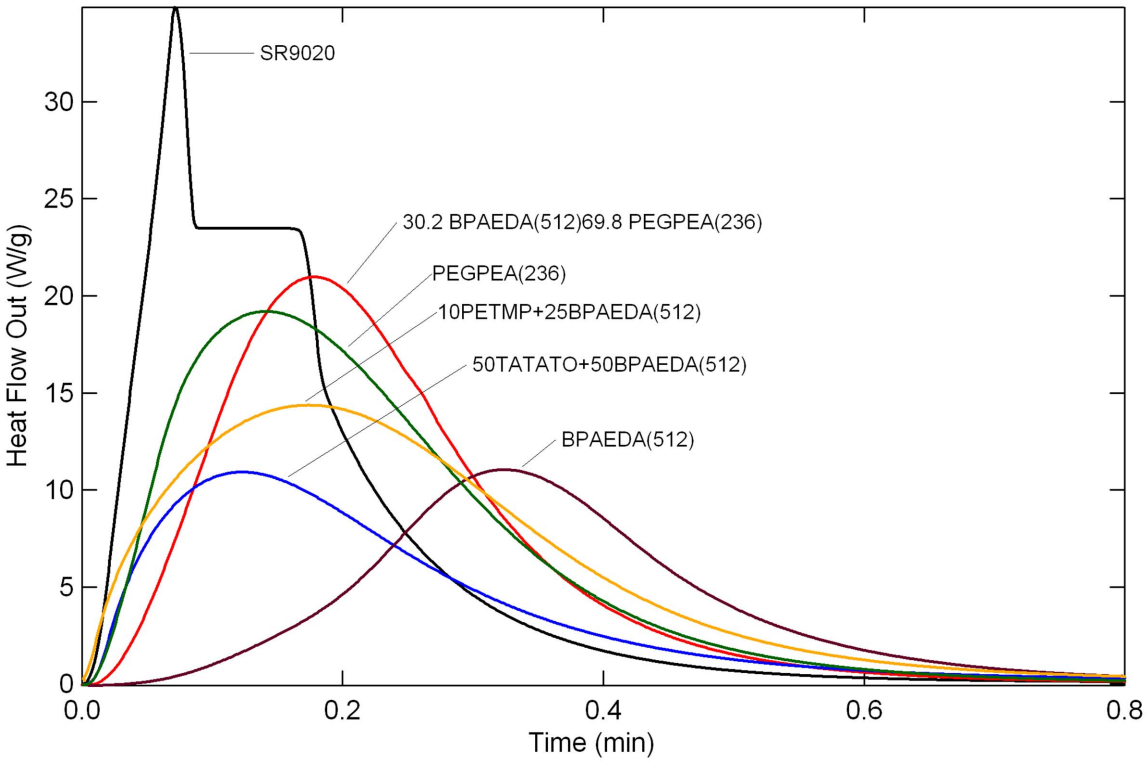

Figure 4.3. PhotoDSC heat flow curves for studied materials.

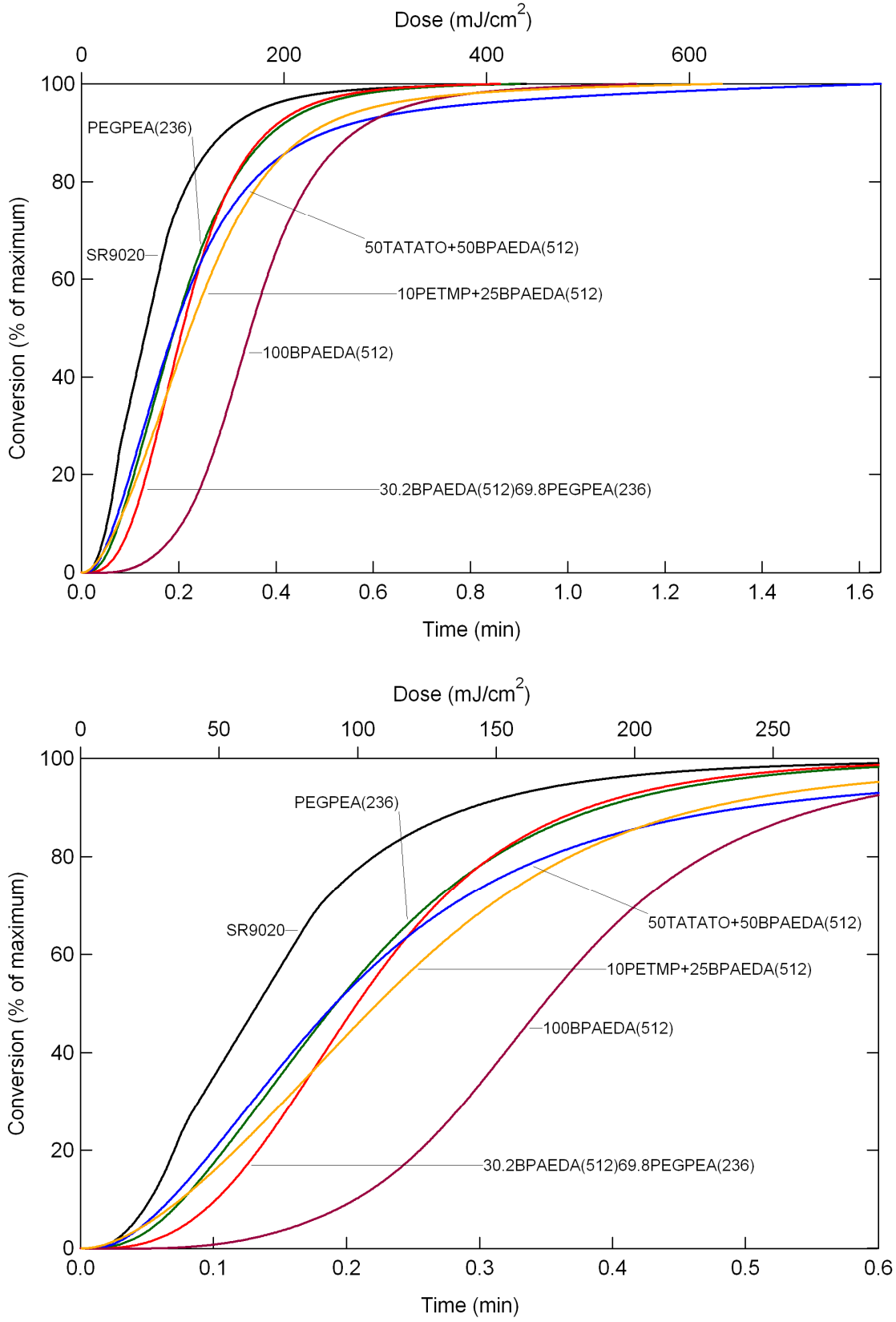

Figure 4.4. (Top) Conversion vs. time and dose curves full scale and (bottom) low dose detail for studied materials.

Table 4.4. Total exotherm for polymerized materials.

Material	Avg. Total Exotherm (J/g)	Std. Dev. (J/g)
SR9020	327.9	13.1
PEGPEA(236)	319.7	0.7
10PETMP+25BPAEDA(512)	300.1	3.0
320.BPAEDA(512)69.8PEGPEA(236)	297.6	4.1
BPAEDA(512)	202.1	8.6
50TATATO+50BPAEDA(512)	190.9	5.1

Converting the mass-normalized heat flow vs. time curves into conversion curves reveals that the Sartomer triacrylate, SR9020 was the first to reach 50% conversion in 7.8 seconds (62.4 mJ/cm^2), followed by 50TATATO+50BPAEDA(512) and PEGPEA(236) in 11.5 seconds (92 mJ/cm^2), 30.2BPAEDA(512)69.8PEGPEA(236) in 12.5 seconds (99.8 mJ/cm^2), 10PETMP+25BPAEDA(512) in 13.4 seconds (107.2 mJ/cm^2), and finally pure BPAEDA(512) in 20.9 seconds (167 mJ/cm^2). However by the time 98% of maximum conversion is reached for each material, the order changes significantly: SR9020 reaches 98% in 30 seconds (240 mJ/cm^2), 30.2BPAEDA(512)+69.8PEGAPEA(236) and pure PEGPEA(236) in 36 seconds (288 mJ/cm^2), 10PETMP+25BPAEDA(512) and pure BPAEDA(512) in 47 seconds (376 mJ/cm^2), and finally 50TATATO+50BPAEDA(512) in 67 seconds (536 mJ/cm^2).

Preliminary screening studies using the standard Blak-Ray UV source revealed that an exposure of 20 seconds (~80-160 mJ/cm^2) was sufficient to create structures that remained on the substrate without causing crosslinking in the unexposed regions of the mask. The studies also revealed, after optical microscopy (Figure 4.5) and post-processing of the images with ImageJ, that 50TATATO+50BPAEDA(512) shrank <1%

while the 30.2BPAEDA(512)69.8PEGPEA(236) shrank 35-37%. Figure 4.6 compares the internal and external corner patterning of 50TATATO+50BPAEDA(512) compared to 30.2BPAEDA(512)69.8PEGPEA(236), with the photomask for the feature provided for reference.

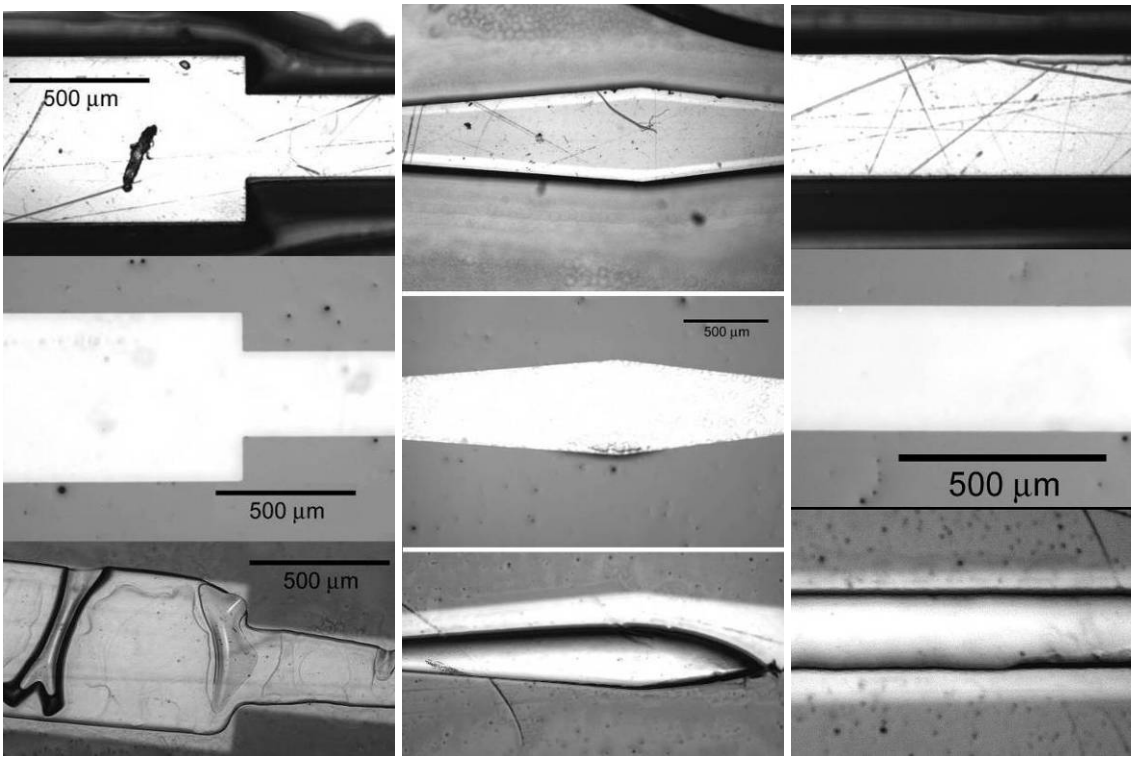

Figure 4.5. Comparison of photopatterning of (top) 50TATATO+50BPAEDA(512), (middle) photomask (bottom) 30.2BPAEDA(512)69.8PEGPEA(236). Scale bars are 500 µm. Surface damage is transferred scratches from the photomask, and wrinkling is a result of delamination and shrinkage while developing in acetone.

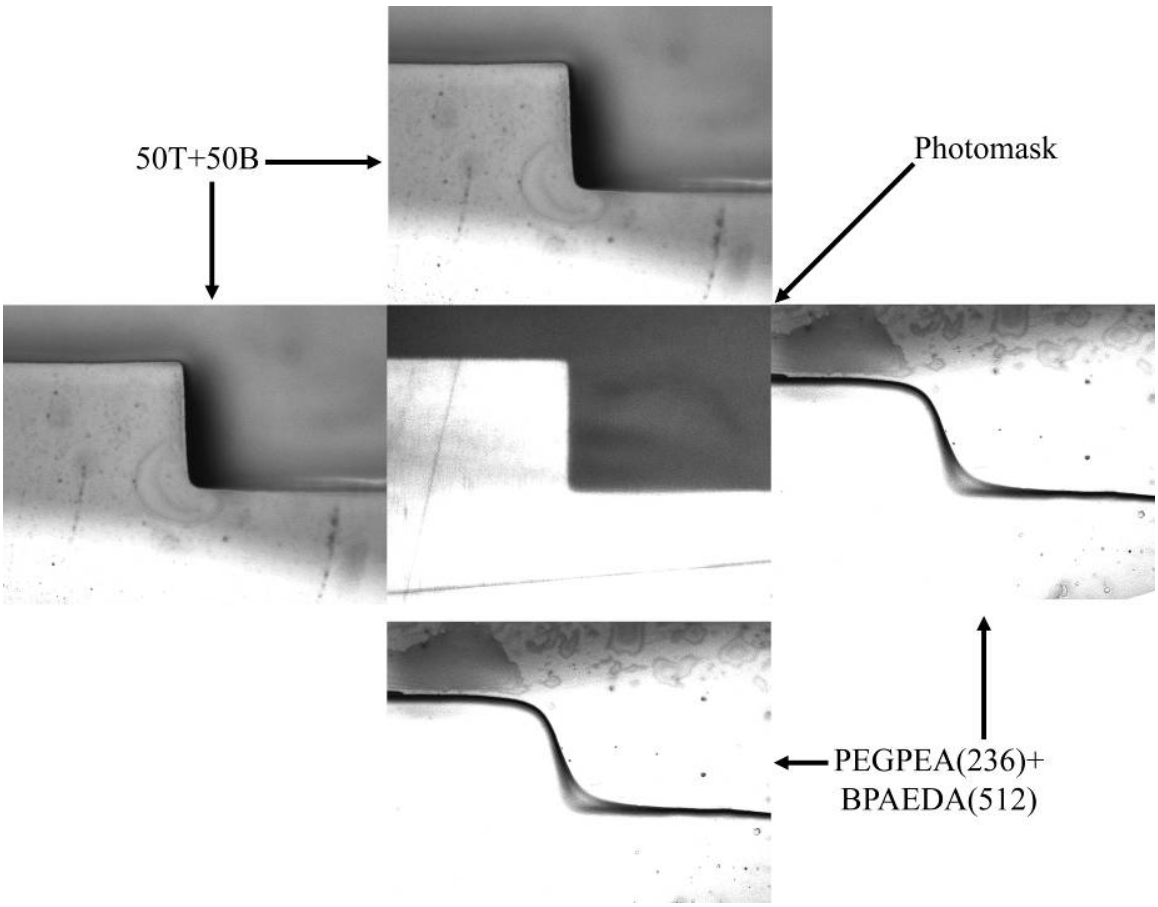

Figure 4.6. Internal and external corner patterning comparison between 50TATATO+50BPAEDA and 30.2BPAEDA(512)69.8PEGPEA(236), with photomask as reference.

Figure 4.7 shows additional patterning capabilities of 50TATATO+50BPAEDA by displaying various polymer structures. Figure 4.8 shows the patterning of 10PETMP+25BPAEDA(512), which shrank ~11%, compared to the actual photomask. Additional inspection under an optical microscope also revealed that, as with other photopatternable materials, source collimation is essential to the quality of the patterning through the height of the structure - the standard UV source used was unable to maintain sufficient fidelity throughout the thickness of the layer.

Figure 4.7. Additional photopatterned structures made with 50TATATO+50BPAEDA(512).
Scale bars are (top) 500 µm (middle) 200 µm (bottom) 40 µm.

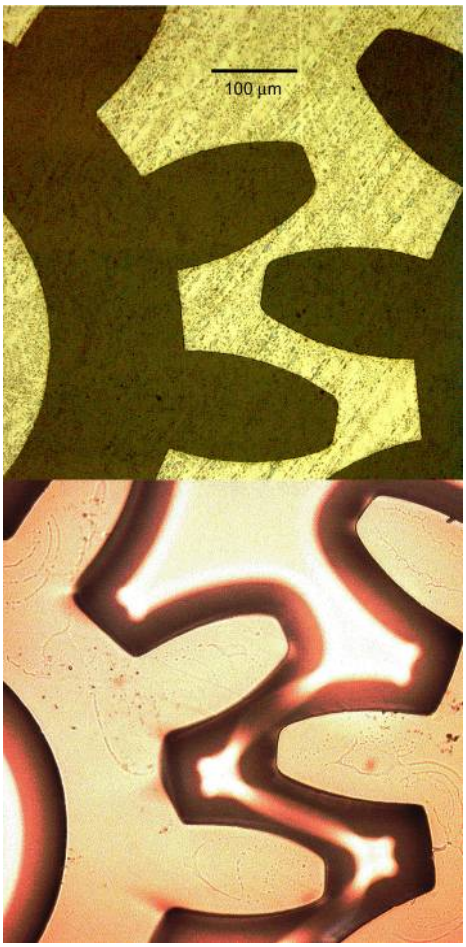

Figure 4.8. Optical microscopy images of (top) photomask and (bottom) resultant photopatterning of 10PETMP+25BPAEDA(512).
Scale bar is 100 µm.

The results of the first round of 2^3 factorial design study (Table 4.2) are compiled in Table 4.5. Figure 4.9 shows some representative structures from these tests.

Table 4.5. Results of first round of 2^3 factorial design study.

Test #	Results and Notes
1	Overexposed
2	Delamination occurred during washing
3	Underdeveloped near larger groups of close-together structures
4	Overdeveloped with some delamination
5	Underdeveloped, wavy features after development
6	Underdeveloped, excess monomer not washed away
7	Underdeveloped, excess monomer not washed away
8	Underdeveloped with some delamination

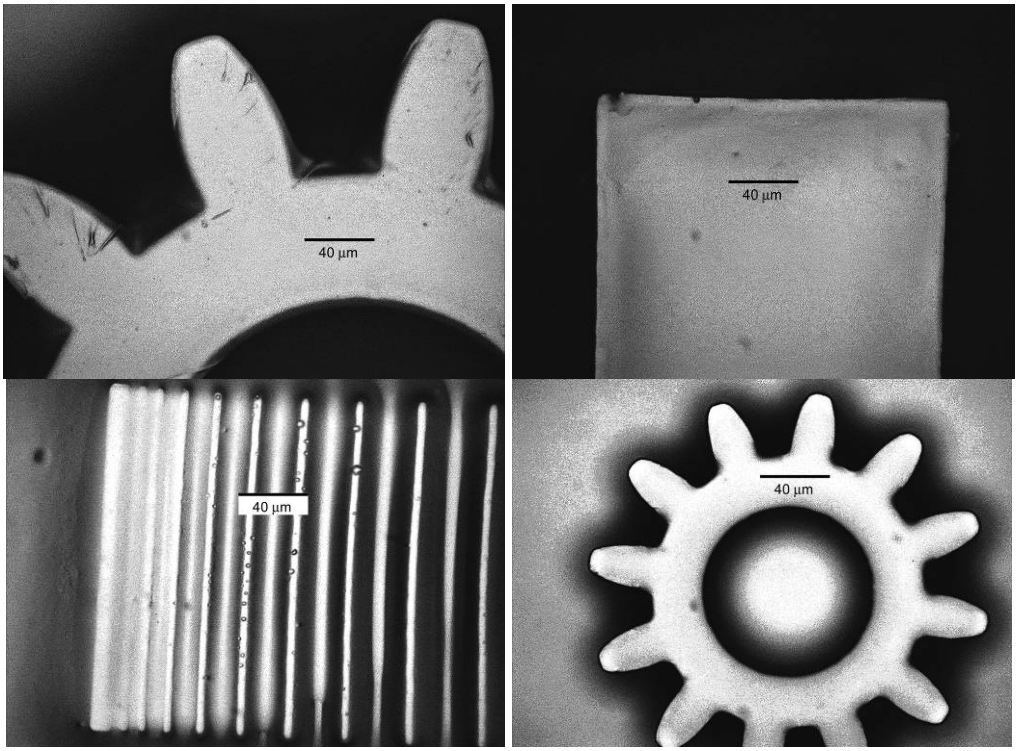

Figure 4.9. Optical micrographs of structures from first factorial design study. Test # (clockwise from top left) 2, 3, 8, 6. Scale bars are 40 µm.

Table 4.6 shows the compiled observations and results from the second round of 2^3 factorial design study.

Table 4.6. Results from the second round of 2^3 factorial design study.

Test #	Results and Notes
1	Underdeveloped in regions of high structure density, especially near substrate
2	Slight underdevelopment in narrow channels
3	Underdeveloped in regions of high structure density
4	Strong delamination in some areas
5	Underdeveloped generally
6	Underdeveloped generally
7	Underdeveloped generally
8	Underdeveloped generally

Figure 4.10 shows SEM images of some features from the second factorial design study which were underdeveloped. Figure 4.11 shows electron microscope images of well-

developed structures from the same study. ImageJ processing on these structures revealed that the sidewall/divergence angle was ~5-6° using the collimated source.

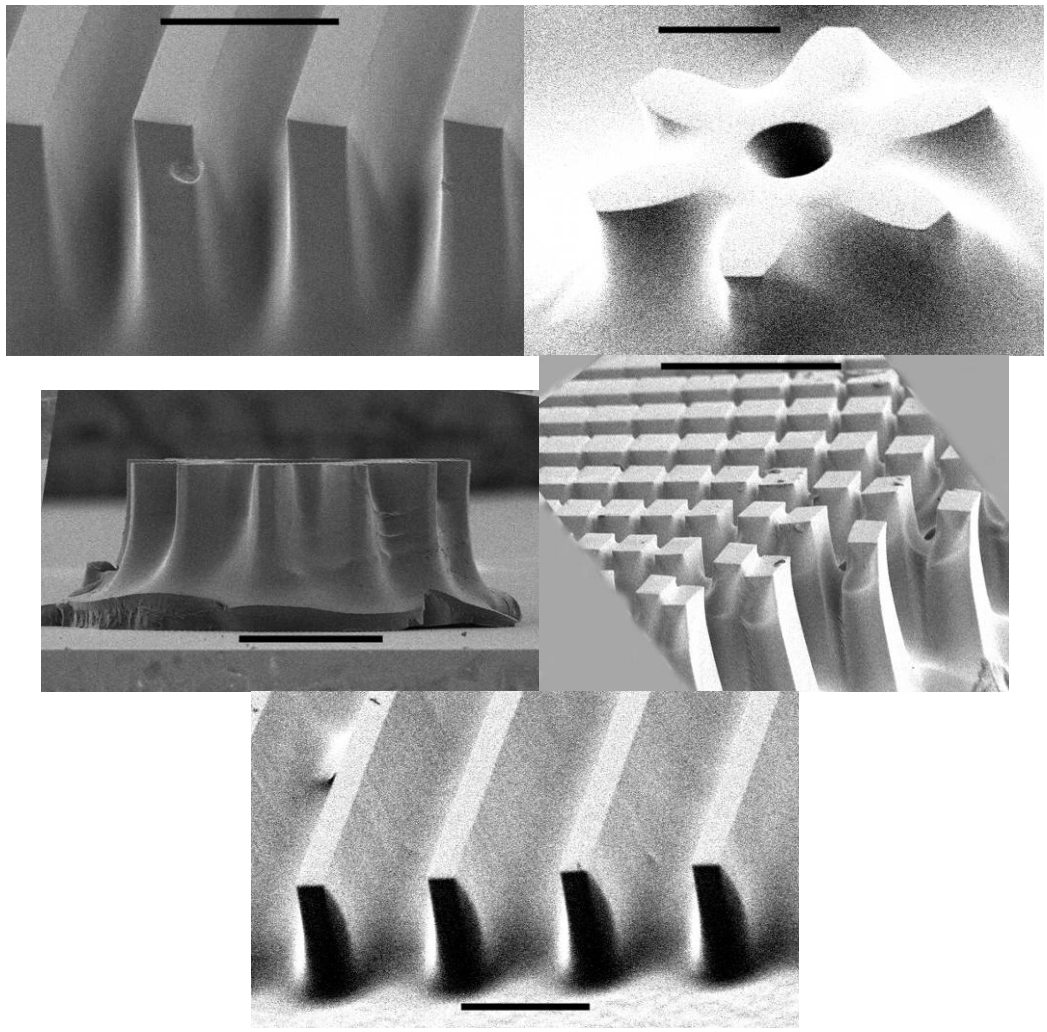

Figure 4.10. Underdeveloped features from second level factorial design study. Test # - scale bar length (μm), clockwise from top right: 3-200-gear in monomer, 1-500-rectangular columns, 2-200-tall rectangles, 1-500-side view of gear, 1-250-tall rectangles in monomer.

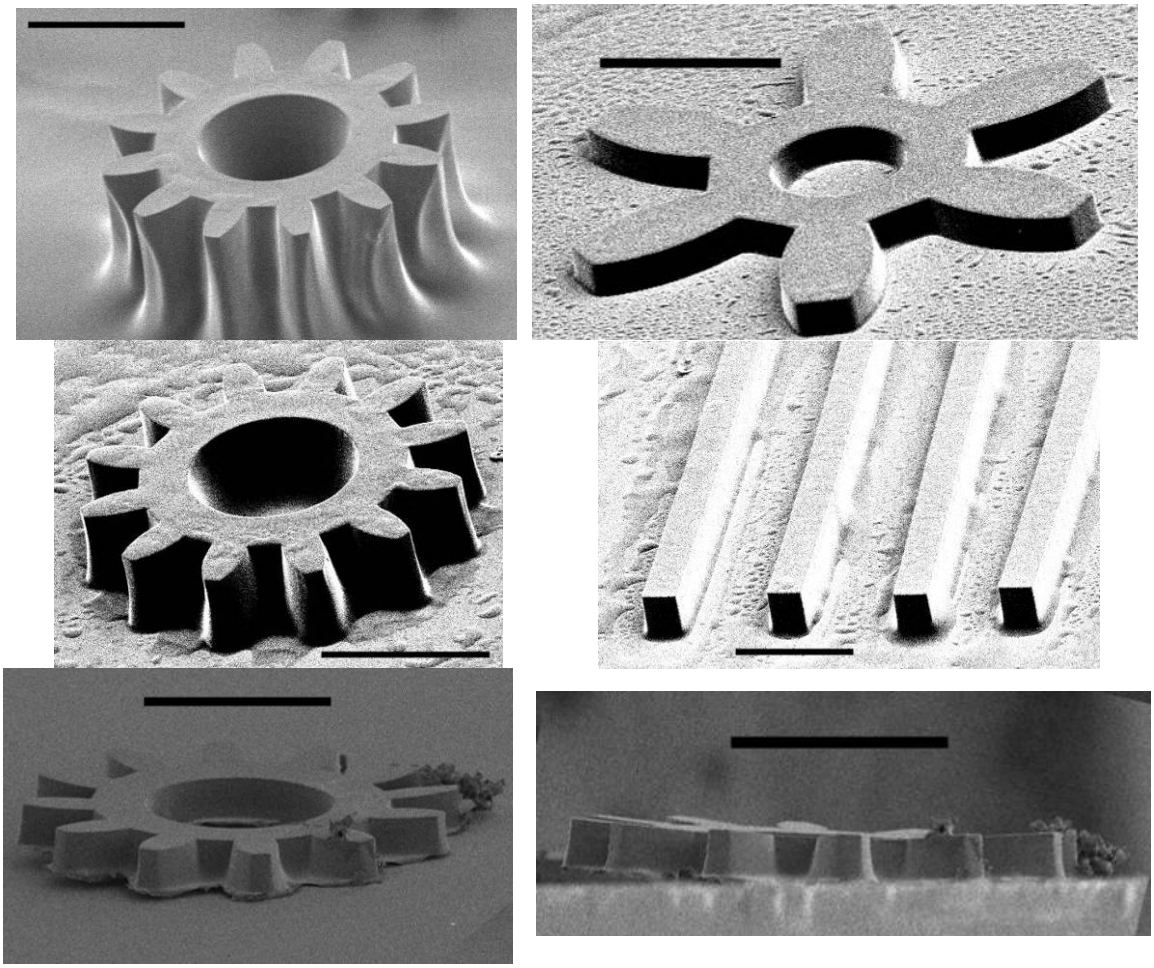

Figure 4.11. Well-developed structures from second factorial design study. Test # - scale bar length (μm): (left column from top) 1-500, 4-250, 4-500 (right column from top) 2-200, 4-200-square tip probes, 4-500-side view of gear from left column.

The minimum negative or positive feature size that 50TATATO+50BPAEDA(512) can pattern is 5 μm or better, since 5 μm is the minimum resolution of the mask (Figure 4.12). The negative features appear to be larger than those of the mask due to optical effects, including washout of the photomask lines due to the large surrounding whitespace. The minimum spacing between features depends on the thickness due to geometry and the angle of divergence; the general geometrical rule for this scenario is a minimum of 8.75 μm space between structures for every 100 μm of thickness. Structures with an aspect ratio of >3:1 were created.

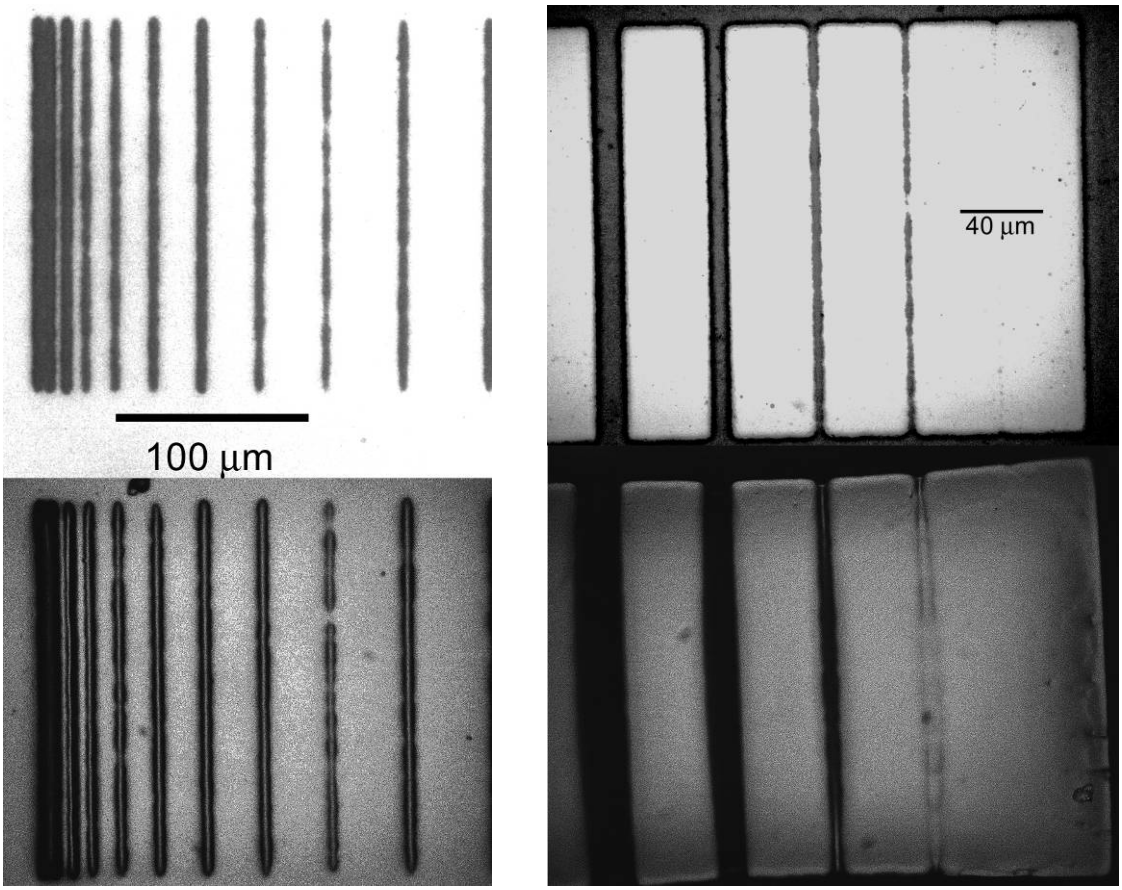

Figure 4.12. Optical micrographs showing (a) negative and (b) positive features. The top part of both images is the photomask, with the bottom being the resulting patterned polymer (a) slide 7 (b) slide 4 from the first factorial design study.

4.5. Discussion

50TATATO+50BPAEDA(512) and the binary acrylate 30.2BPAEDA(512)69.8PEGPEA(236) are substantially equivalent thermomechanically, as revealed by DMA. 50TATATO+50BPAEDA(512) was also the fastest material to reach 50% of maximum conversion among the materials to be photopatterned, which is important because this is near the conversion that resulted in the best structures during preliminary screening studies. However, the difference between the time-to-50% for this mixture and that for the binary acrylate was essentially inconsequential. Additionally,

50TATATO+50BPAEDA(512) released the smallest amount of energy on a per-gram basis during polymerization, reducing potential thermal gradients and related effects that can alter viscosity, diffusion rates, and the dimensional stability of resultant structures. Comparison materials, such as the triacrylate SR9020 showed the extremely rapid polymerization behavior common in popular photopatternable materials. The monofunctional acrylate PEGPEA(236) polymerized faster than the difunctional acrylate BPAEDA(512) in contrast to the general trend of higher functionality leading to higher speed, but the polymerization of the Bisphenol A-based acrylate is likely diffusion-limited due to its much higher viscosity.

During photopatterning and development, the shrinkage of the binary acrylate 30.2BPAEDA(512)69.8PEGPEA(236) was extreme and led to wavy and nonuniform edges, features of varying width, and extremely rounded corners (Figure 4.5 and Figure 4.6). The 50TATATO+50BPAEDA(512), on the other hand, replicated the pattern of the photomask very well and shrank very little, reproducing corners and straight-line features faithfully. Even 10PETMP+25BPAEDA(512), which has a rubbery modulus (and therefore crosslink density) 80% lower than that of the binary acrylate system, still exhibited only 1/3 the shrinkage of the acrylate. Additionally, the shrinkage of 10PETMP+25BPAEDA(512) was more controlled and predictable. The overall shapes, corners, and linear features were maintained (Figure 4.8), indicating that masks for this materials could possibly be designed to account for the shrinkage.

The preliminary screening studies for the 50TATATO+50BPAEDA(512) showed that even a standard UV light benchtop setup would result in structures that accurately pattern

from the mask with very little shrinkage. The angle of divergence for these structures is worse than was desirable due to the lack of source collimation, but thin (<25 μm) structures should be produced with sufficient accuracy. These initial studies also created a benchmark range for exposure dose for the factorial design studies.

The factorial design studies themselves served to narrow the processing parameter space which results in excellent polymer structures. In addition to using a collimated source to greatly reduce the divergence angle, the source had a more uniform irradiance than the Blak-Ray and it had a controllable dosage output utilizing a shutter system. The best processing conditions from the study appear to be structure dependent, but are generally found with dosages ranging from 58.5 mJ/cm^2 to 85.5 mJ/cm^2 in thicknesses from about 75 μm to 500 μm, with a development of at least 60-75 seconds or more. The most well-defined structures came from test #'s 2 and 4, which had the lowest aspect ratio and highest development time. This is largely due to the flexibility of polymer at room temperature which makes high-aspect ratio structures fall over or bend, and partly due to the reduced potential for scattered/refracted radiation and radical diffusion at lower depths in the liquid monomer mixture. Potential solutions to the flexibility issue are to use cold acetone as a wash and to cool the material prior to development to enhance the rigidity of the structures.

The greatest challenge in the processing of these copolymers is the post-exposure development of the crosslinked portions of polymer. Insufficient development will result in unwashed structures while excessive development can cause curling and complete

delamination of the polymer from the substrate in acetone[‡]. Residual monomer on a structure (e.g. Figure 4.10, top right) poses a problem because the thiol-ene monomers are prone to a "dark reaction," whereby the monomer mixture will polymerize over time without any external stimulus, destroying any definition imposed by the photomasking process.

4.6. Conclusions

Thiol-ene/acrylate copolymers showed good patternability for a range of thermomechanical properties. The thiol-ene/acrylate copolymer patterned much better than a binary acrylate mixture that had the same thermomechanical properties; even a thiol-ene/acrylate with a fraction of the crosslink density of the binary acrylate was able to pattern much better than the acrylate was. These results demonstrate that thiol-ene/acrylates can fulfill a role in micropatterning that pure acrylates cannot because the selected thiol-ene chemistry and reaction scheme allows for a system that is tunable, has a lower crosslink density and stiffness, and can still be reliably photopatterned. A particular thiol-ene/acrylate mixture, 50TATATO+50BPAEDA(512), has been photopatterned into shapes and structures that are particularly suitable for/capable of being used in MEMS or small-scale biomedical devices. However, the critical issue which remains to be solved for this system is the polymer-to-substrate adhesion, which is directly linked to the ability to properly develop the patterned structures.

[‡] Numerous attempts at enhancing the adhesion of the polymer to the substrate utilizing various coatings (gold, 2-hydroxyethyl methacrylate, etc.) met with limited success, with sputter-coated gold showing the most promise.

Direct fabrication of polymeric microdevices generally wastes less material and can be more accurate than creating a mold with a sacrificial photoresist material and direct writing also takes only a fraction of the time needed to create either a mold or direct feature with a typical photoresist. Thiol-ene/acrylate copolymers show promise as a system that can be directly patterned with a range of crosslink densities and properties.

CHAPTER 5. CONCLUSION

The first chapter provided an introduction to the materials and methods that were to be used in the research. Critical techniques that were used in the research included mechanics of materials methods, such as bulk tensile deformation, and polymer characterization, such as DMA, PhotoDSC, FTIR, and sol-fraction testing. A newer mechanical characterization method, nanoindentation, was used because of the extreme force and displacement resolution which was necessary to study, for the first time, the properties of structures created by laser focal point polymerization. The main materials that were studied were (meth)acrylates and thiol-ene polymers, both in bulk and at the small scale. The first chapter also established the purpose and scope for performing the research, as well as discussing the potential impact and the expected benefits. The thermomechanical properties of thiol-ene/acrylate polymers are not well studied, but knowledge of their properties and understanding the various relationships between monomer/network structure, thermomechanical properties, reaction mechanism, and polymerization behavior is critical before thiol-ene/acrylate copolymers can be adopted for use and used in design work. Additionally, photopatterning of polymers at the micrometer scale usually requires the sacrifice of desired thermomechanical properties in favor of desired polymerization behavior, whereas thiol-ene/acrylate materials have the potential to avoid the sacrifice; this research showed that this held true.

The second chapter described the first instance of the mechanical characterization of polymers formed at the sub-micrometer scale using two-photon stereolithography and compared the results to those of bulk-polymerized photopolymers. It was determined

that intensity (or power) had a larger effect on the resultant properties than stage translation speed did, as was expected from first principles of two-photon absorption. As with standard photopolymerization, the modulus and hardness of the material dropped when overall dose was reduced, most likely due to reduced conversion. Higher intensity also resulted in stiffer materials, even for the same dose, as a result of higher conversion caused by larger polymerization exotherms, in agreement with earlier bulk single-photon photopolymerization studies. It was also discovered that materials fabricated via the two-photon process could be made stiffer and harder than a material fabricated using standard photopolymerization routes as a result of the combination of high intensity and high dose. The mechanical characterization of both the bulk polymer and micrometer-scale structures in the second chapter was performed via nanoindentation. This technique was uniquely suited to measuring the properties of the two-photon-produced polymer structures because the scale of the indentation required for characterization was small compared to the size of the structure.

Chapter 3 covered the establishment and understanding of a structure-property map for thiol-ene(/acrylate) copolymers in bulk form. The kinetics of thiol-ene(/acrylate) polymerization and modeling of the network are well described in the literature, but a rigorous description of the thermomechanical behavior of thiol-ene(/acrylate) networks was necessary in order to provide a more complete description of thiol-ene/acrylate materials. It was found that thiol-ene copolymers tend to exhibit a subambient T_g and low-to-moderate E_r, while the addition of a high-T_g difunctional acrylate increased both properties. The magnitudes of the changes in the properties were highly dependent on the amount of acrylate added, as anticipated. Thiol-ene(/acrylate) networks exhibited a

broad range of thermomechanical behaviors, from a nearly thermoplastic elastomer to a highly crosslinked network.

Chapter 4 discussed the photopatterning capabilities and processing fundamentals of thiol-ene/acrylate networks selected from the third chapter for either their "average" properties or their low crosslinking. An acrylate with equivalent properties was patterned alongside to emphasize the uniqueness of thiol-ene/acrylate copolymers' ability to maintain pattern fidelity and polymerize rapidly with even low-to-moderate crosslinking densities. The acrylate material was unable to retain the features of the photomask, while the thiol-ene/materials showed much lower, more predictable shrinkage with excellent pattern transfer. Exposure doses for various intensities and development times were determined for two different monomer layer thicknesses. The minimum resolution for feature spacing and size for both positive and negative features was determined. Different solvents were examined for their ability to wash away the unexposed monomer. The importance of source collimation for low wall divergence was investigated. A multitude of sample structures suitable for MEMS and biomedical devices were created and imaged.

The research described in this work was an investigation into the relationship between bulk photopolymerized materials and polymer structures made via two-photon stereolithography, the thermomechanical properties of thiol-ene and thiol-ene/acrylate polymers in bulk form, and the ability of thiol-ene/acrylate materials to be photopatterned at the micrometer scale. Using nanoindentation, the mechanical properties of TPS structures were determined and a basic understanding of the process-mechanical property

map for two-photon polymerization was developed. Analysis of a study of fourty-one thiol-ene(/acrylate) copolymers using various standard chemical and thermomechanical characterization techniques provided an understanding of the links between the process, structure, and properties of thiol-ene(/acrylate) materials in bulk form. A series of screening and factorial design studies using the hard contact photopatterning method with thiol-ene/acrylate materials and an acrylate material showed the superior ability of thiol-ene/acrylates over pure acrylates to photopattern at the micrometer scale with moderate crosslink density.

Based on the results of the research, there are several recommendations for future research that would strengthen and expand the current results. A study comparing the received dose to the mechanical properties of TPS polymers would provide a parameter that, along with intensity, would describe the expected properties of structures made with TPS. Additionally, comparison of the properties of samples made with different monomers (especially with different functionality) would establish a more universal process-property map for TPS. A swelling study and elemental analysis of the eluent of the thiol-ene networks would provide information about the structure of the polymer network and of the materials extracted via sol-fraction testing. For instance, large amounts of swelling would indicate a loosely crosslinked network, which, along with FTIR and DMA data, could determine the amount of pendant bonds on dangling chains compared to the amount of unconverted bonds on soluble monomer and oligomer. This additional information would further enhance the understanding of the structure-property relationship in thiol-ene/acrylate networks. Finally, additional studies investigating the post-exposure development, in terms of both time and solvent, and substrate adhesion

promotion would enhance the adoption of thiol-ene/acrylate materials in photopatterning processes. Solution of these two issues would greatly enhance the repeatability and predictability of the photopatterning of thiol-ene/acrylates, since these two facets were identified as the most critical issues hindering the process.

This research will have a significant impact on the understanding of thiol-ene/acrylate polymers and of the capabilities of two-photon stereolithography. This work provides the groundwork for significant advancement in polymer photolithography, MEMS, and micro-biomedical devices because of the first quantification of TPS-produced structures compared to bulk materials and the demonstration of the photopatternability of thiol-ene/acrylate copolymers with tunable mechanical properties (and low crosslink density). These newly developed and characterized materials and processes will allow designers more choices when designing microdevices with mechanically functional components; these choices will allow for new devices and components to de designed which were previously bulky or impossible with silicon and other current materials because of their property ranges and given device size/mass constraints. Potential microscale applications for these materials and processing techniques include soft cantilevers, sensor/actuator components with properties that exhibit temperature sensitivity (such as valves), and soft neuronal probes.

APPENDIX A:

NANOINDENTATION OF TWO-PHOTON POLYMERS

The first generation of structures polymerized via-two photon were squares composed of 50:50 wt:wt SR368:SR9008, both triacrylates, in an array form with power varying in the horizontal direction and speed varying in the vertical direction. Part of the array can be seen in Figure A.1, and detail shots of a square with good exposure conditions and a square with poor exposure conditions are shown in Figure A.2. The inter-line spacing is sufficiently large compared to the lateral voxel dimensions that individual raster scans can be seen. Surface roughness affected indentation results (not shown).

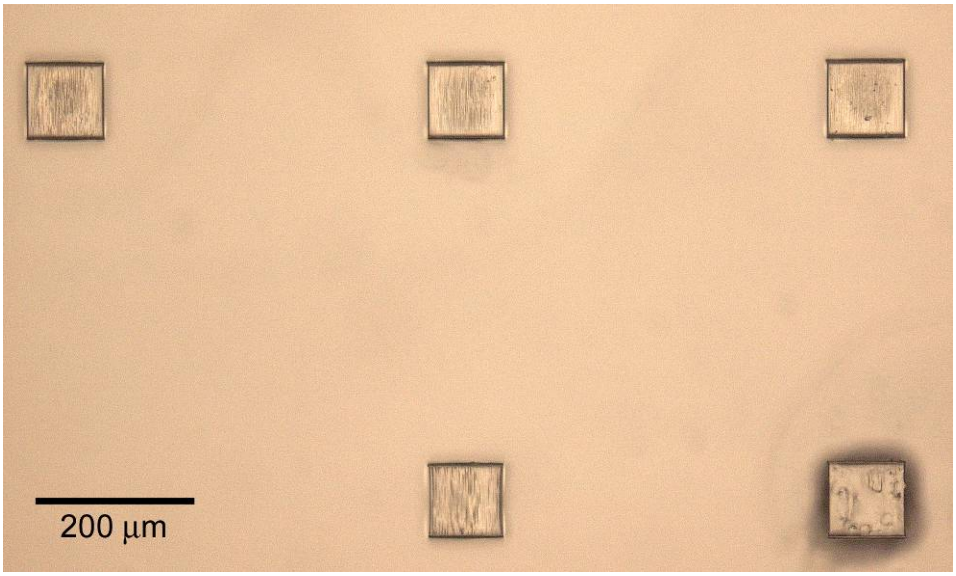

Figure A.1. Two-photon squares of 50:50 wt:wt mixture of SR9008:SR368.

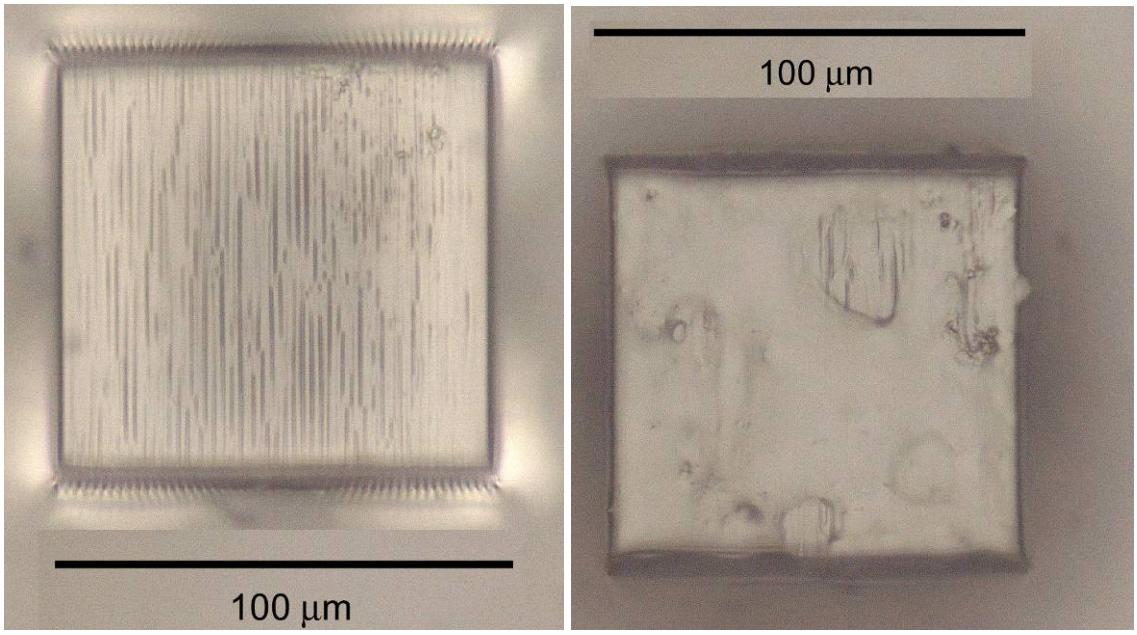

(a) (b)

Figure A.2. Two-photon squares with (a) good and (b) poor processing conditions.

Second generation materials were bar shapes, similar to third generation materials reported in Chapter 2, but polymerized out of the earlier mixture of 50:50 wt:wt SR368:SR9008. SR9008 was subsequently discontinued by the manufacturer, prompting the switch to SR9020. The second generation bars can be seen in Figure A.3. Detail images of bars with good development and poor development can be seen in Figure A.4.

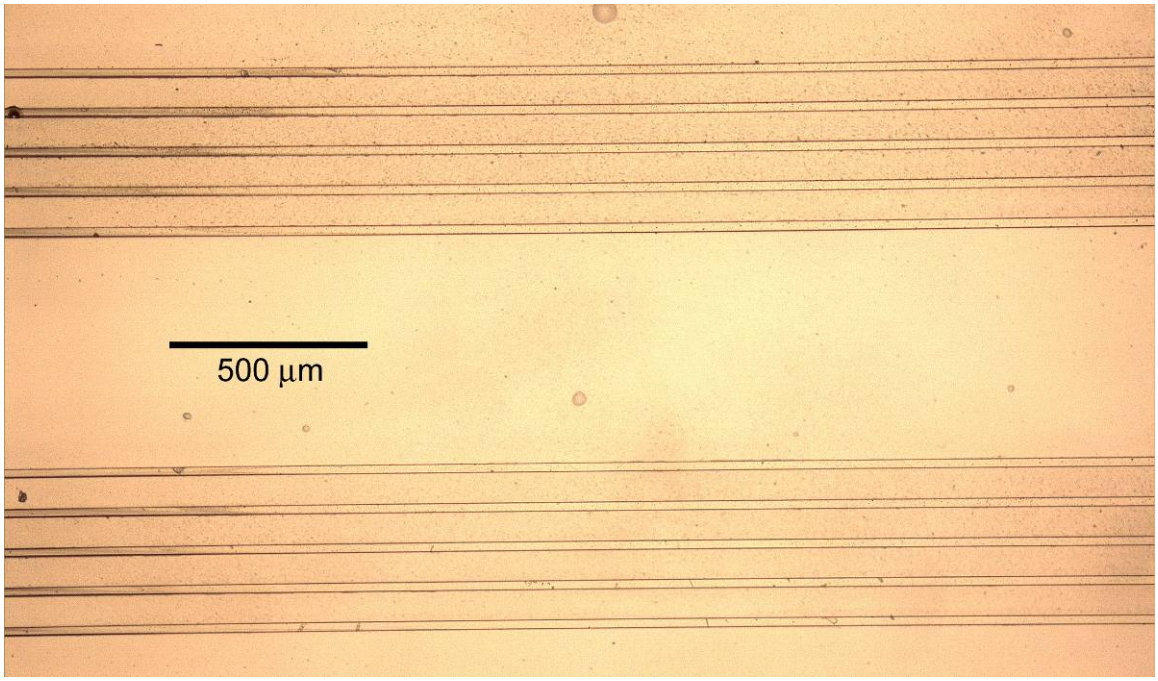

Figure A.3. Portion of second generation two-photon array of SR9008:SR368.

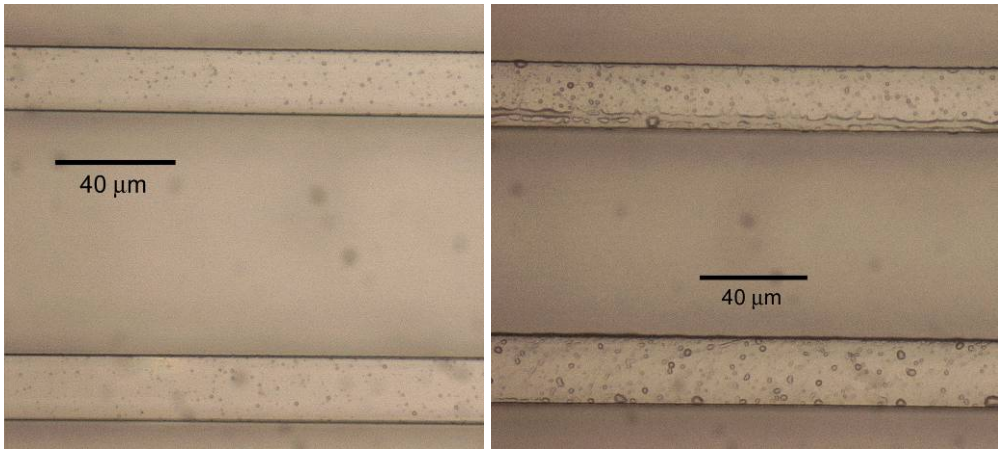

(a) (b)

Figure A.4. Detail views of bars with (a) good and (b) poor development.

Nanoindentation was performed on these structures. The modulus and hardness of the materials is plotted against speed, with series listed as a function of input power. The modulus and hardness results are shown in Figure A.5 and Figure A.6, respectively.

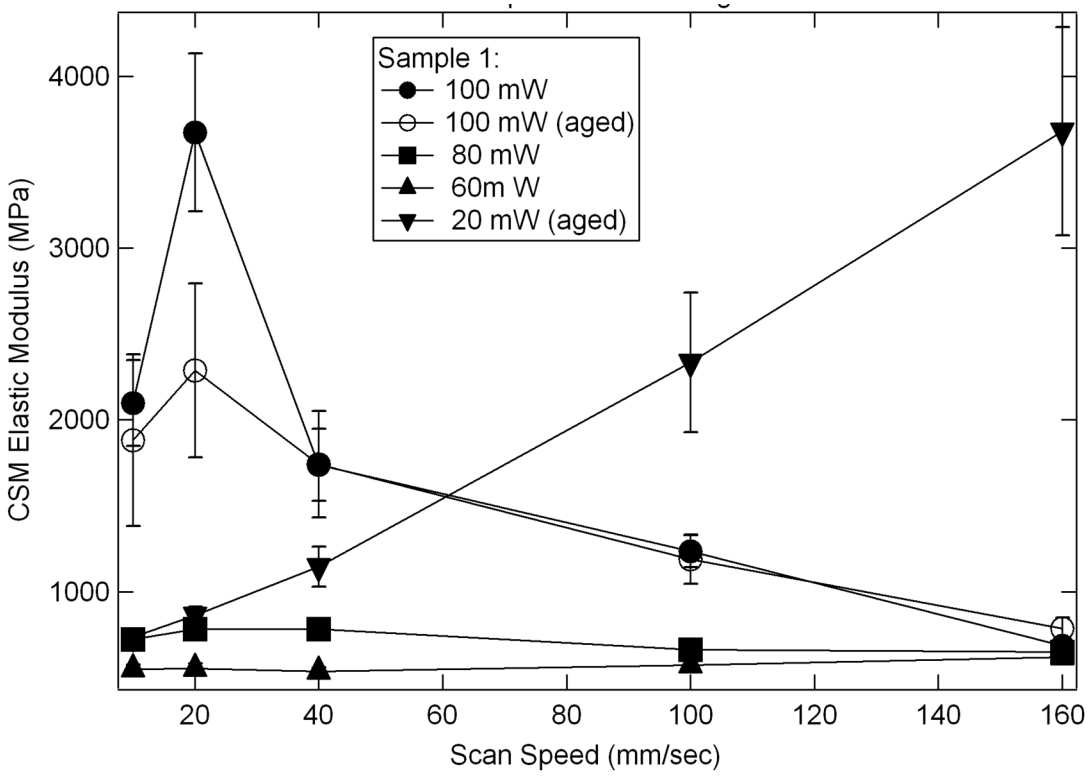

Figure A.5. CSM modulus for second generation two-photon array.

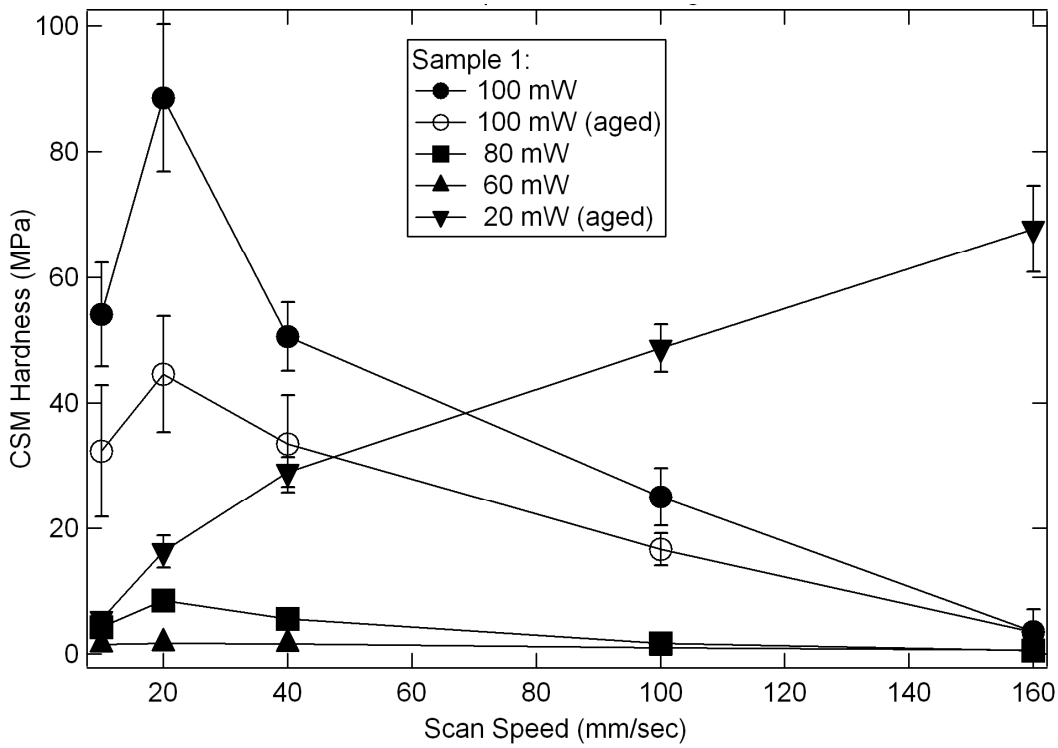

Figure A.6. CSM hardness for second generation two-photon array.

The modulus and hardness followed the expected trends with the exception of the 20 mW power setting and speeds below 20 mm/s. The 20 mW samples exhibited trends quite opposite those of the other materials, for reasons unknown. The drop in modulus and hardness below 20 mm/s was thought to be caused by damage as a result of overexposure and thermal chain scission. However, the same effect did not appear in the third generation samples, which more accurately represents the typical processing parameter window for two-photon stereolithography, and so the cause for this low-speed behavior in the second generation samples remains undiscovered and uninvestigated.

APPENDIX B:

SUPPLEMENTAL OPTICAL/ELECTRON IMAGES OF PHOTOPATTERNED POLYMERS

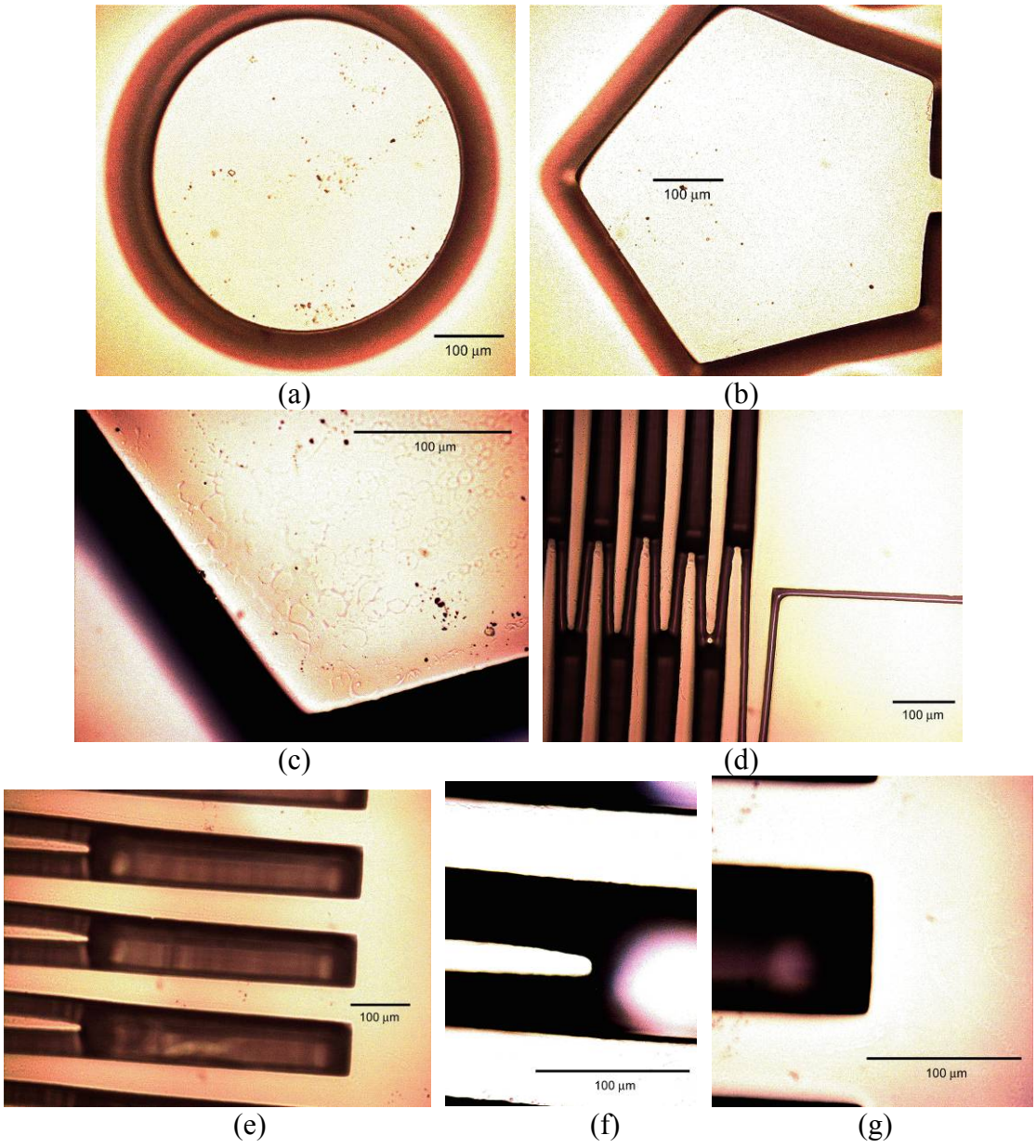

Figure B.1. Additional photopatterned structures of 10PETMP+25BPAEDA(512). (a) circle (b) pentagon (c) pentagon corner detail (d) "resistor" flow baffles with microchannel corner (e) flow baffle edges, corners and tips (f) baffle tip detail and (g) baffle internal corner detail. Scale bars are all 100 µm.

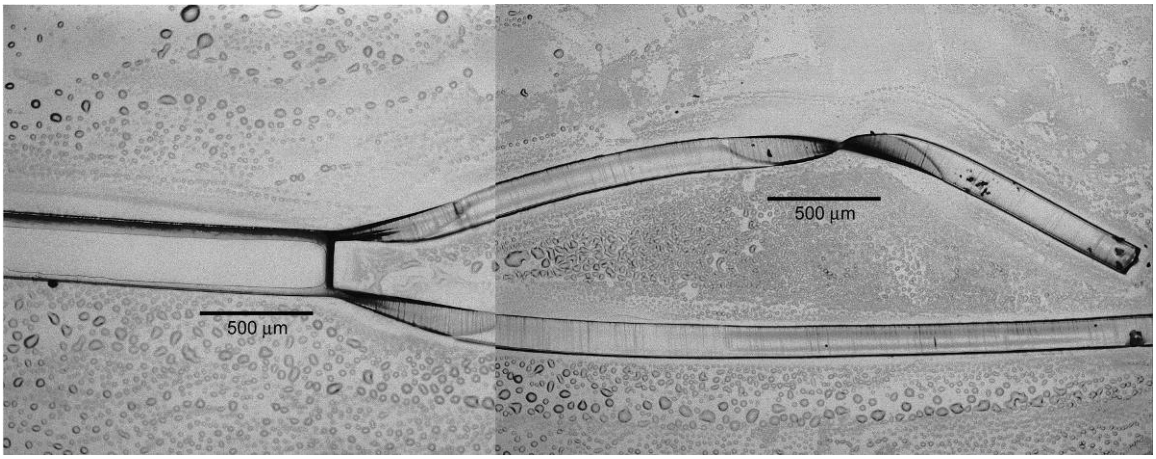

Figure B.2. Optical microscope image of tweezer shape.
Material is 50TATATO+50BPAEDA(512) and tips have a height:width aspect ratio of ~4:1. Due to rubbery nature of polymer at room temperature and poor substrate adhesion, tips have fallen over and twisted after development in acetone.

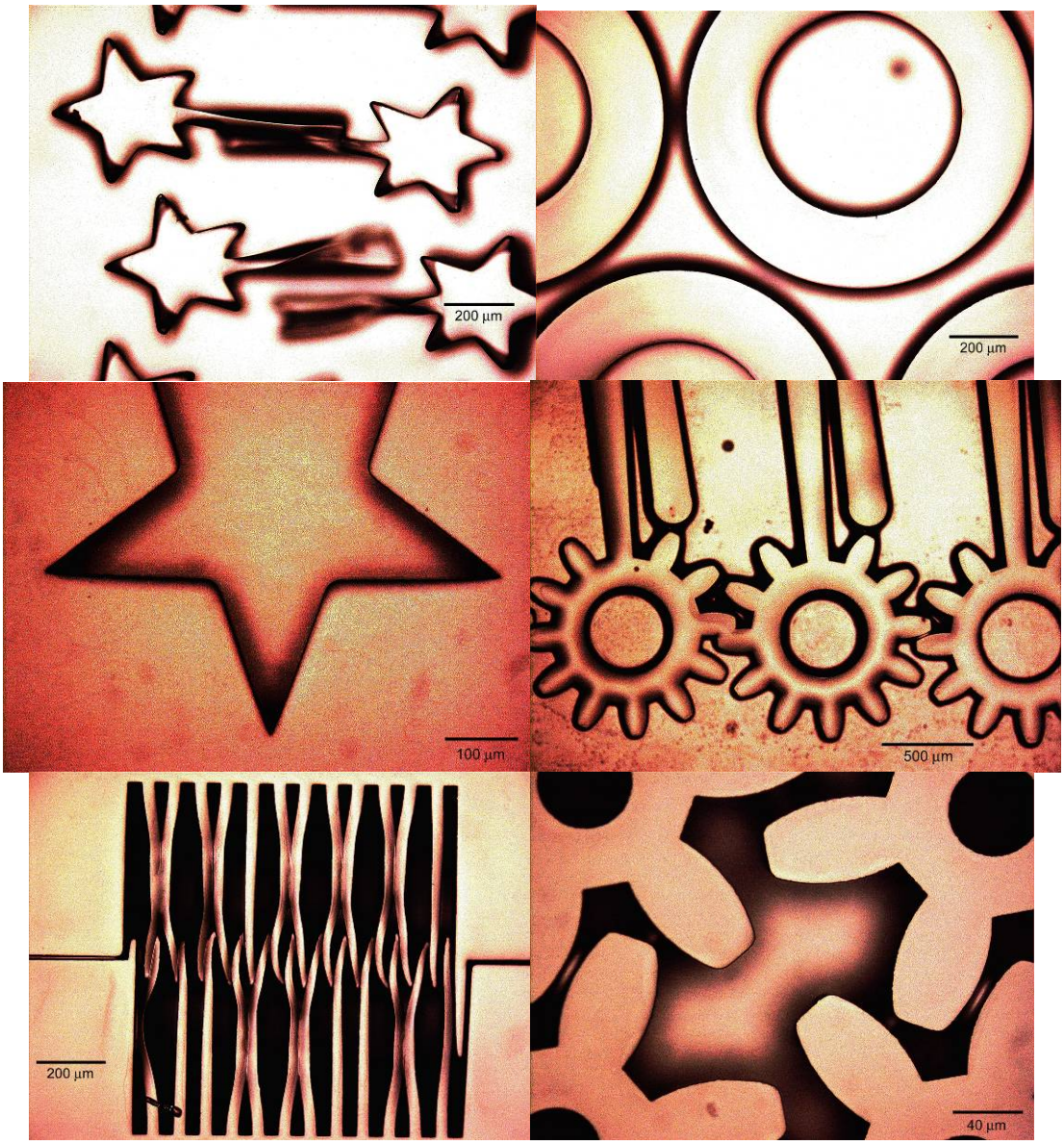

Figure B.3. Other shapes from photopatterning screening studies. Material is 50TATATO+50BPAEDA(512), scale bars as shown. (top left) stars on wand shafts, used for manipulation (top right) annuli (middle left) star-shaped hole, used as a target for star wands (middle right) gears on wand shafts, used to manipulate gears and operate miniature gear trains (bottom left) fluid resistor baffle system, baffles have moved due to surface tension and flexibility in acetone during development (bottom right) detail of small gears, near where teeth are in close proximity on mask.

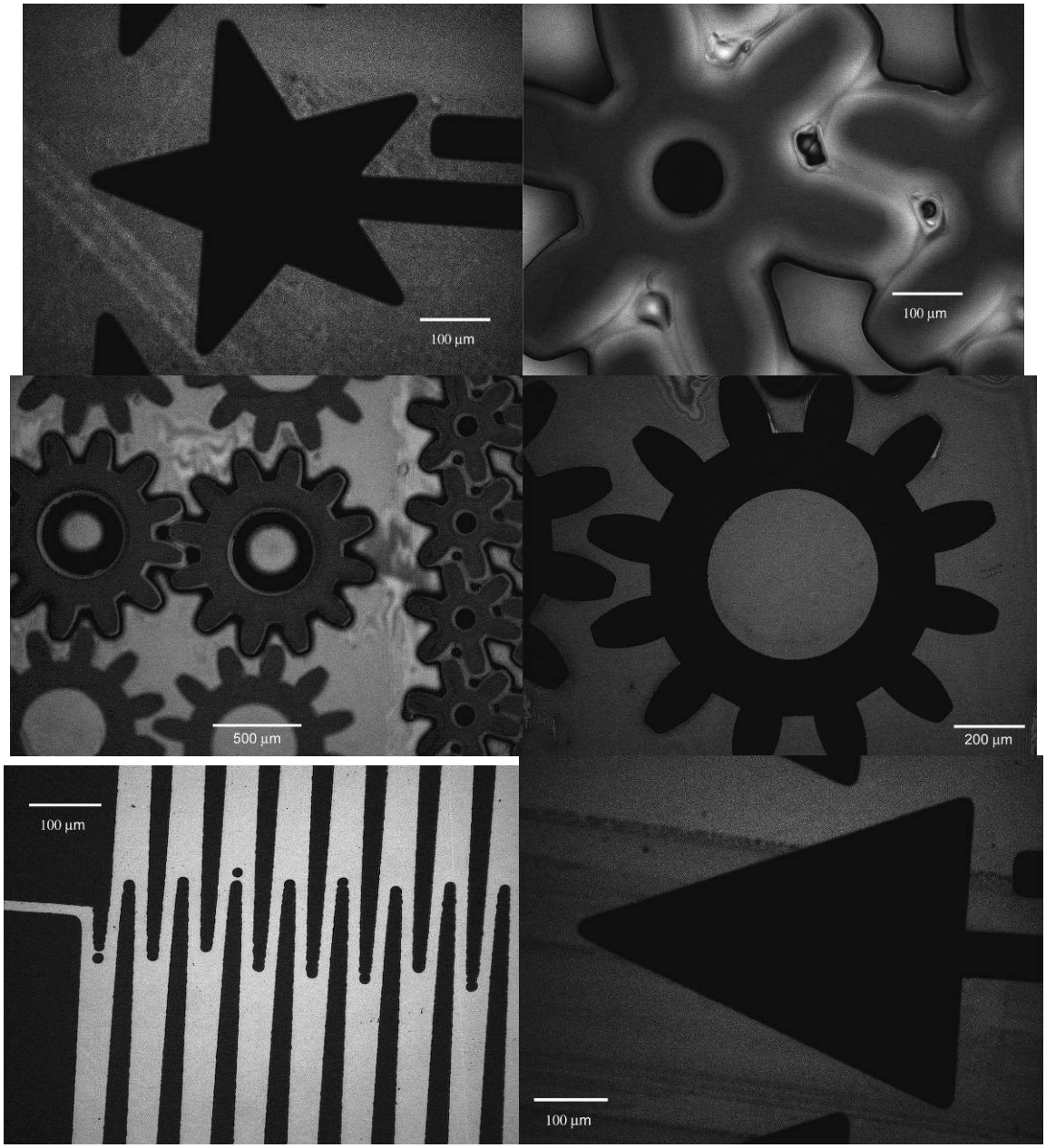

Figure B.4. Optical images of photomask and bottoms of gears. Material is 50TATATO+50BPAEDA(512) from screening studies using Blak-Ray lamp, scale bars as shown. (top left) photomask of star wand (top right) bottom of small gears in close proximity (middle left) bottom of large and small gears and photomask of big gears (middle right) detail view of big gear photomask (bottom left) photomask of fluid resistor baffle system (bottom right) triangle wand photomask.

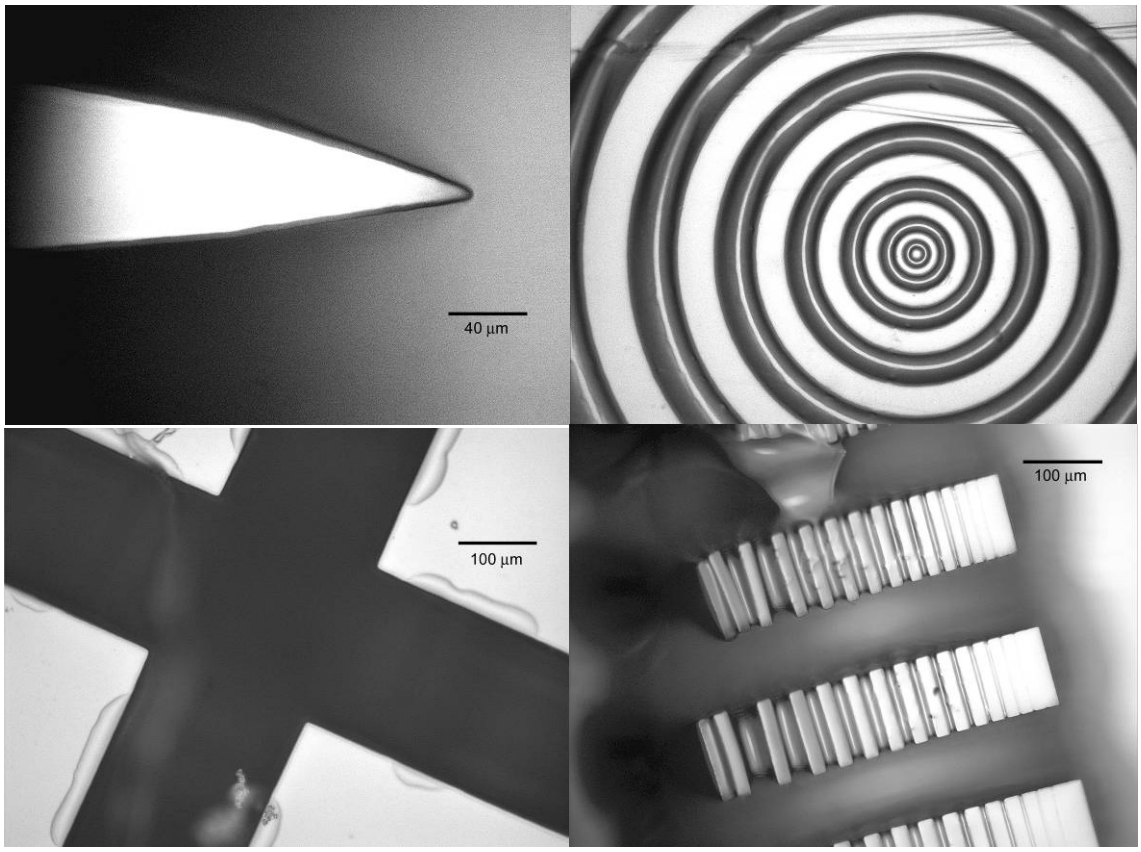

Figure B.5. Optical images from screening study using exposure chamber. Material is 50TATATO+50BPAEDA(512) and exposure time was 3 minutes at ~6 mW/cm^2. Sample was covered with crossed microlouver sheets which eliminate incident light at angles more than ±35º. (top left) probe tip shape (top right) concentric positive/negative circles (bottom left) negative cross shape (bottom right) positive bars of varying width and spacing, used for resolution study, incident light from high angles causes unwanted crosslinking between structures.

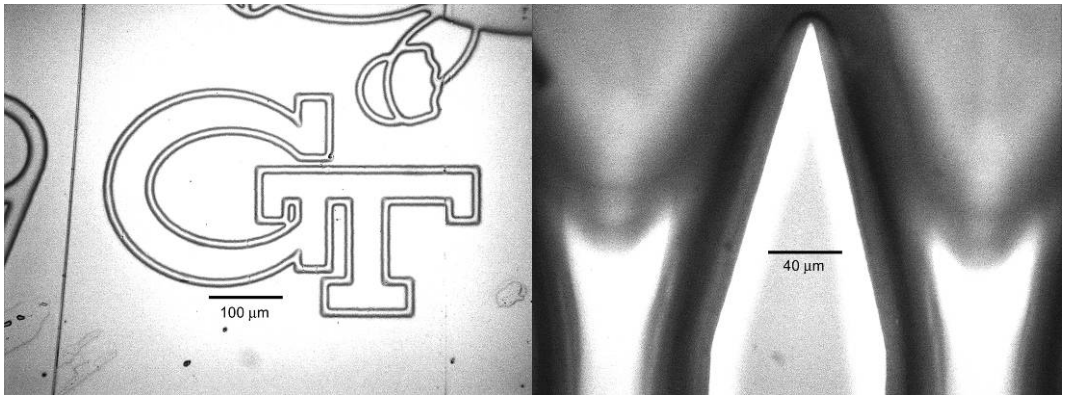

Figure B.6. Structures from first factorial design study. (left) negative lines forming school symbol, linewidth <20 µm (right) probe tip showing ability to obtain and maintain form and sharpness.

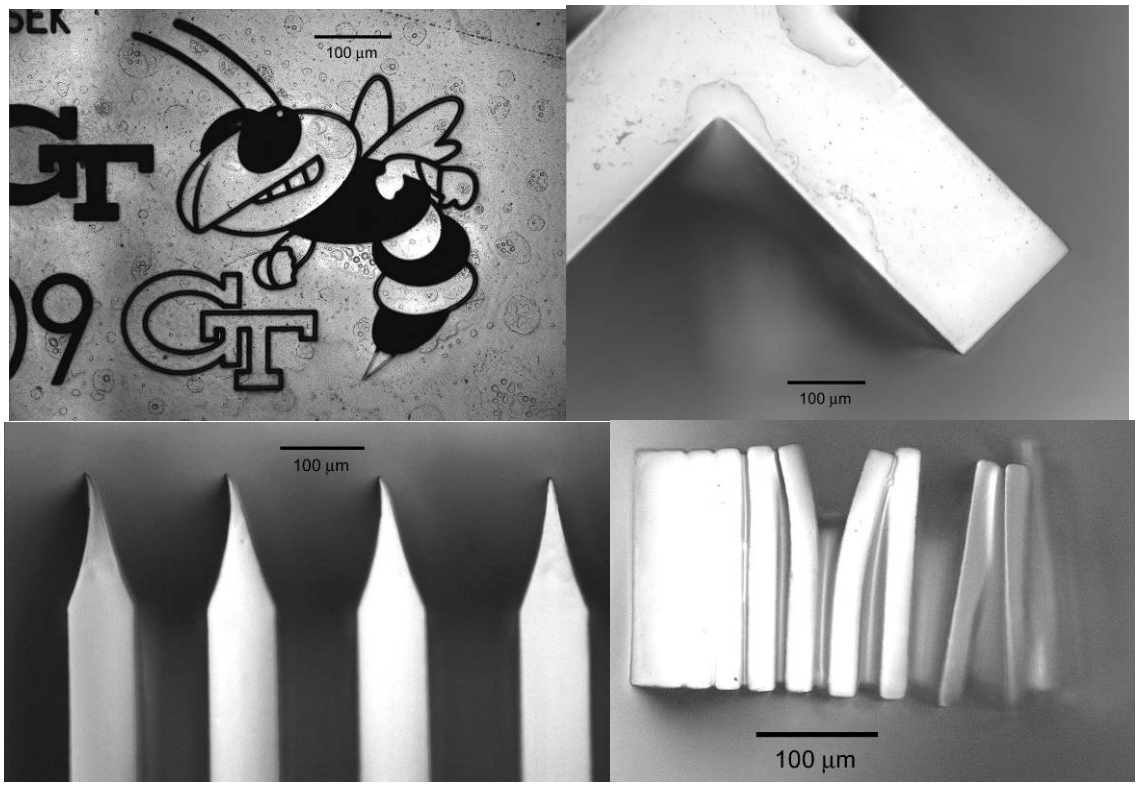

Figure B.7. Images from slide 1, factorial design study round 2.
(top left) negative-tone "Buzz" and "GT" symbol, linewidth ~5 µm (top right) positive cross, showing inside and outside corners (bottom left) concave probe tips (bottom right) bars of varying spacing for resolution study.

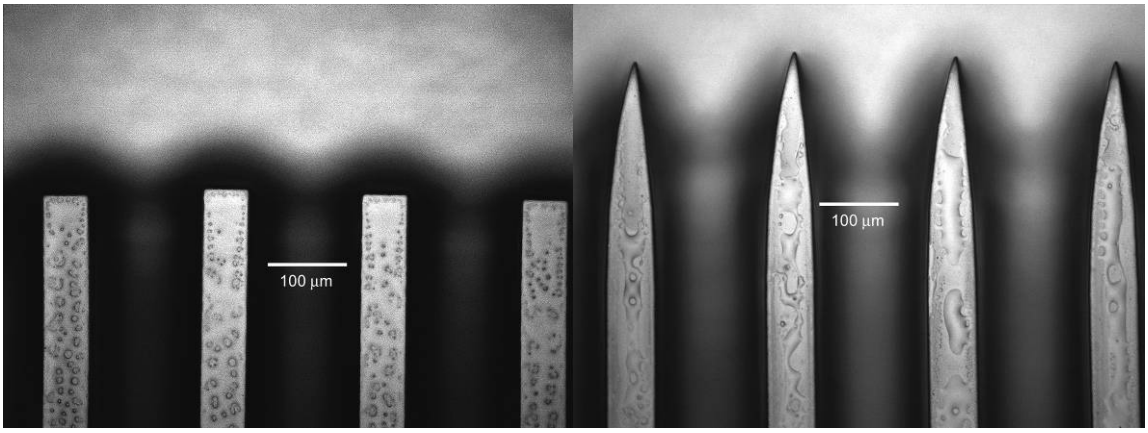

Figure B.8. Probe tips from slide 2, factorial design study round 2.

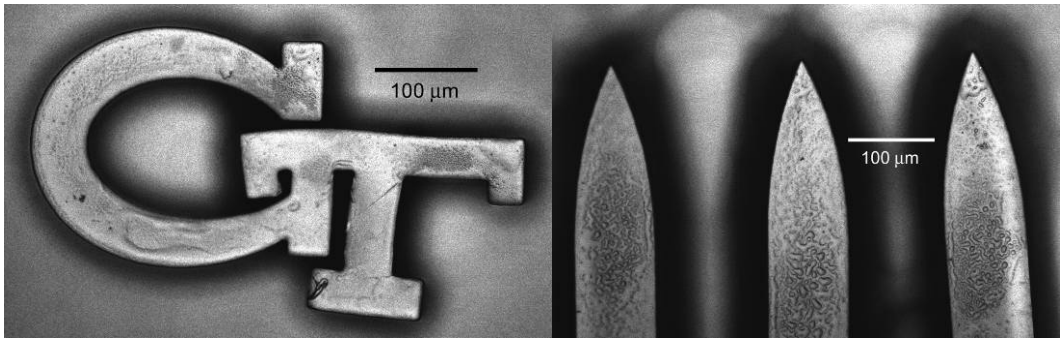

Figure B.9. Structures from slide 4, factorial design study round 2.
(left) positive "GT" (right) convex probe tips. Warping is a result of delamination and resettling during and after development in acetone. Residual monomer can be seen on both the "GT" symbol and on probes.

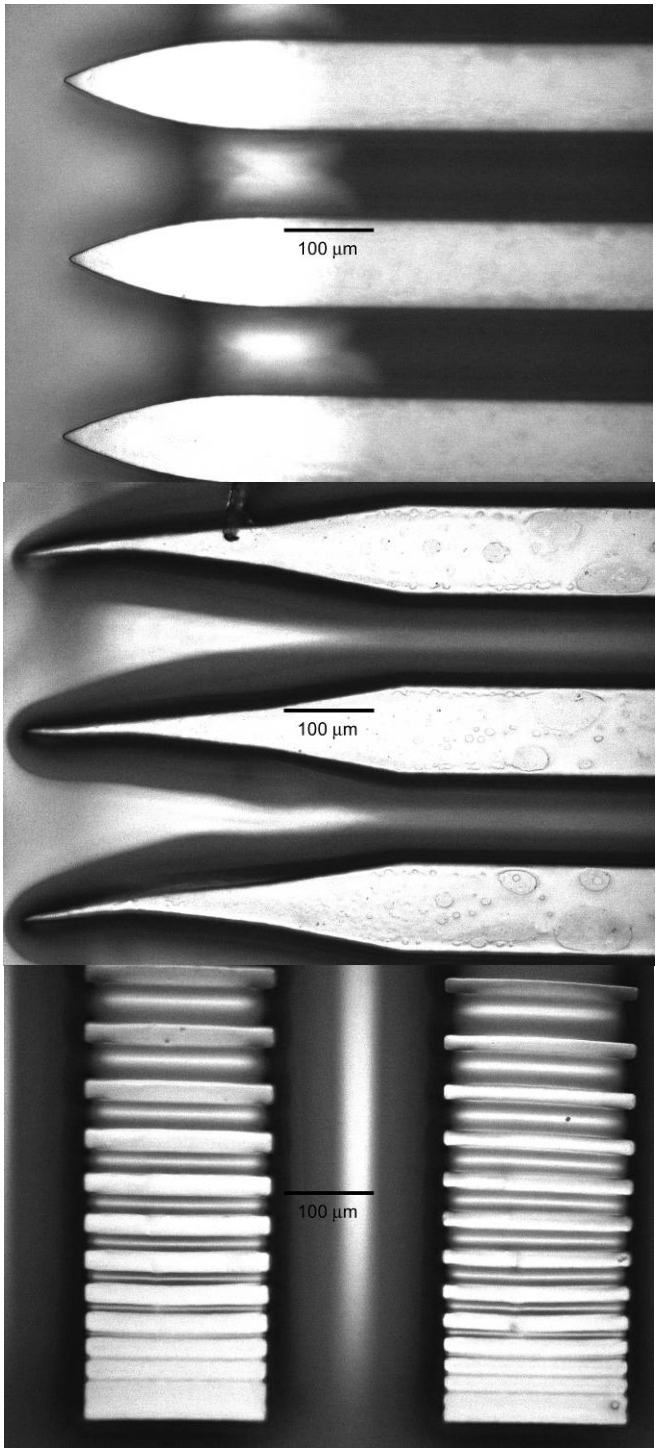

Figure B.10. Structures from slide 6, factorial design round 2.
(top) convex and (middle) concave probe tips (bottom) blocks of varying size and spacing for resolution study.

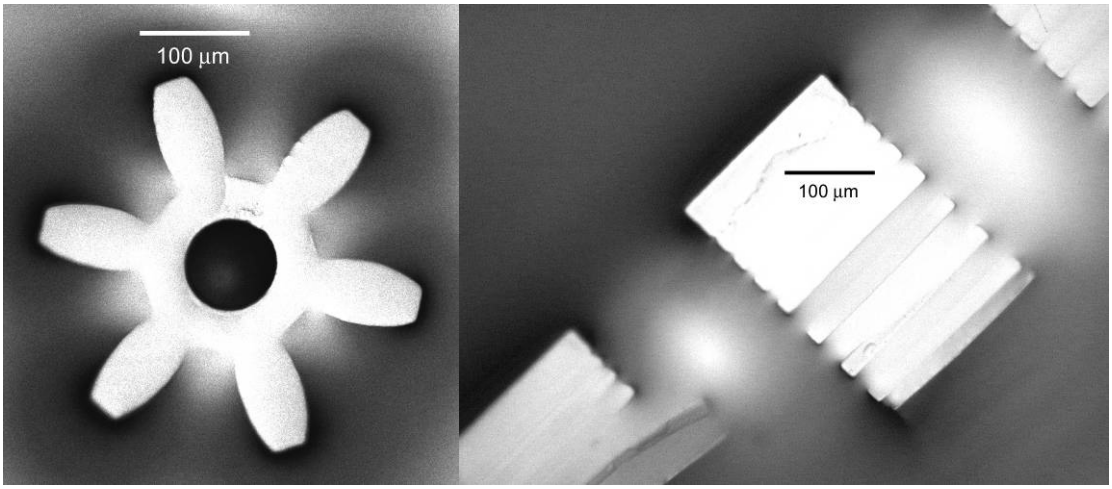

Figure B.11. Structures from slide 7, factorial design round 2, showing poor development.

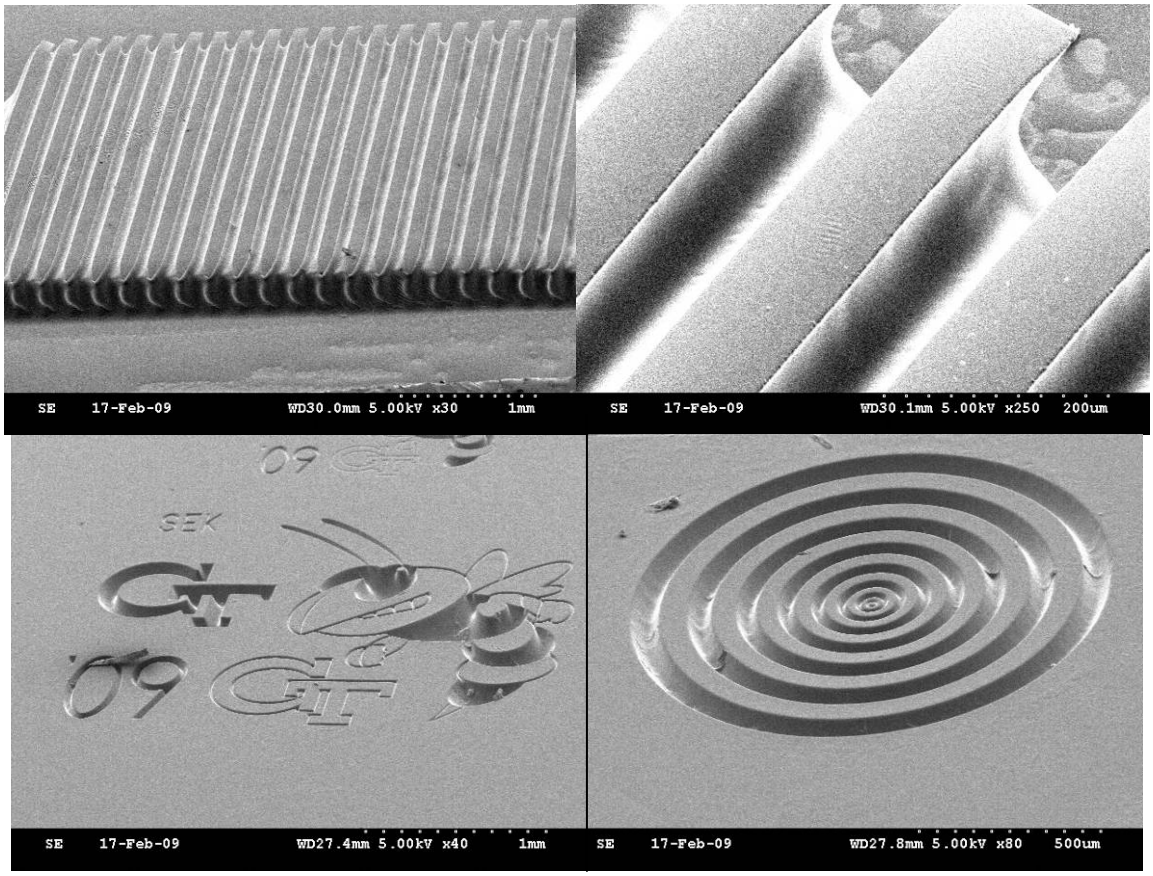

Figure B.12. Oblique SEM images of structures from round 2.
Slide 3:(top left) probe array (top right) probe array detail, showing undercutting as a result of poor exposure and development conditions.
Slide 1: (bottom left) Buzz/GT detail (bottom right) negative concentric rings.

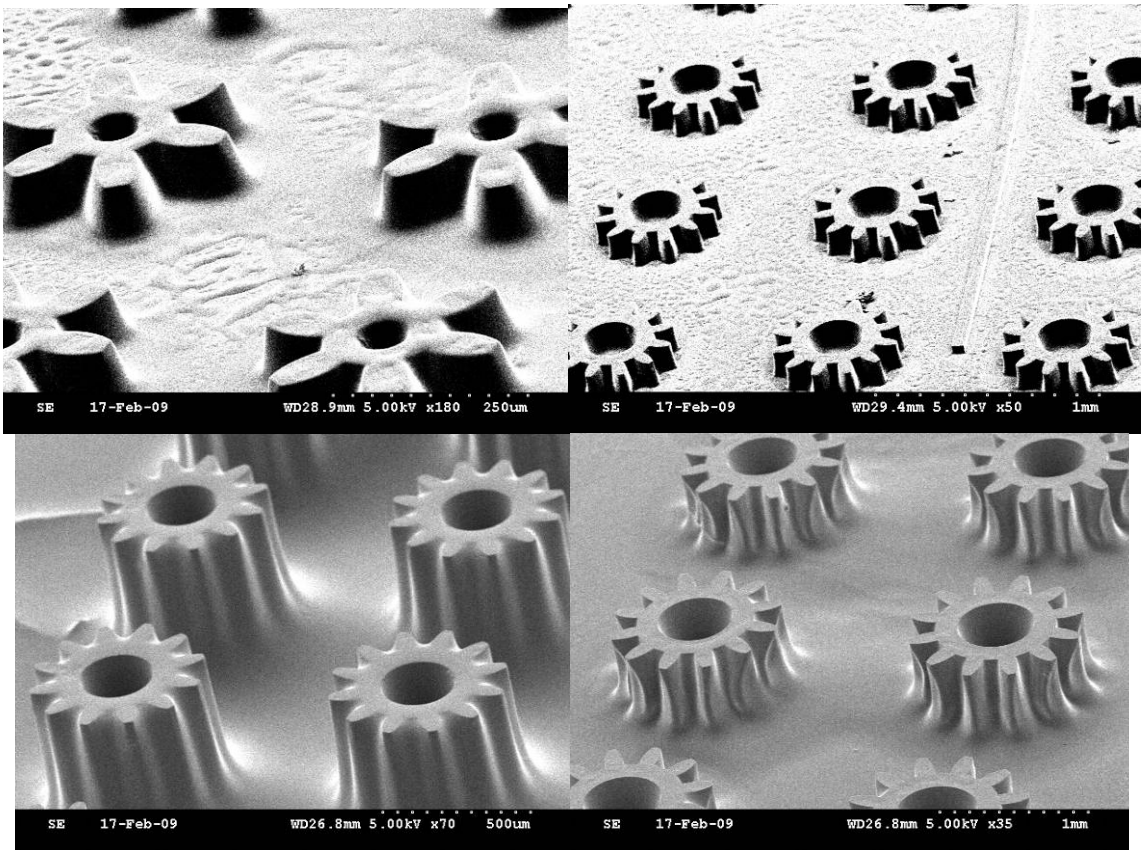

Figure B.13. Oblique SEM images of gear arrays from round 2.
(top left) slide 2 (top right) slide 4 (bottom left) slide 1 (bottom right) slide 1.

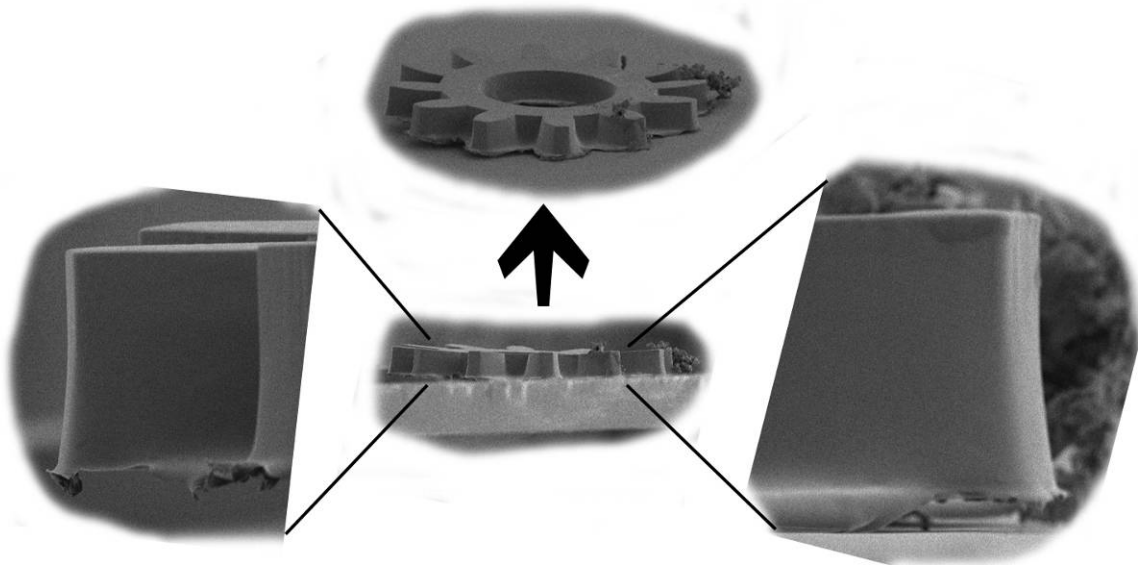

Figure B.14. Various views of a small gear from round 2.
(top) oblique (bottom left) tooth side/tip detail (bottom middle) side view of gear (bottom right) tooth side/tip detail

REFERENCES

1. Chiou BS and Kham SA. "Real-time FTIR and in situ rheological studies on the UV curing kinetics of thiol-ene polymers". Macromolecules 1997; 30(23):7322-7328.

2. Cramer NB and Bowman CN. "Kinetics of thiol-ene and thiol-acrylate photopolymerizations with real-time Fourier transform infrared". Journal of Polymer Science Part A-Polymer Chemistry 2001; 39(19):3311-3319.

3. Cramer NB, Davies T, O'Brien AK, and Bowman CN. "Mechanism and modeling of a thiol-ene photopolymerization". Macromolecules 2003; 36(12):4631-4636.

4. Cramer NB, Reddy SK, O'Brien AK, and Bowman CN. "Thiol-ene photopolymerization mechanism and rate limiting step changes for various vinyl functional group chemistries". Macromolecules 2003; 36(21):7964-7969.

5. Cramer NB, Scott JP, and Bowman CN. "Photopolymerizations of thiol-ene polymers without photoinitiators". Macromolecules 2002; 35(14):5361-5365.

6. Griesbaum K. "Problems and possibilities of free-radical addition of thiols to unsaturated compounds". Angewandte Chemie-International Edition 1970; 9(4):273-287.

7. Hoyle CE, Cole M, Bachemin M, Kuang W, et al. Photoinitiated polymerization of selected thiol-ene systems. Photoinitiated Polymerization, vol. 847, 2003. pp. 52-64.

8. Hoyle CE, Hensel RD, and Grubb MB. "Laser-Initiated Polymerization of a Thiol-Ene System". Polymer Photochemistry 1984; 4(1):69-80.

9. Hoyle CE, Hensel RD, and Grubb MB. "Temperature-Dependence of the Laser-Initiated Polymerization of a Thiol-Ene System". Journal of Polymer Science Part a-Polymer Chemistry 1984; 22(8):1865-1873.

10. Jacobine AF. Thiol-Ene Photopolymers. In: Fouassier JP and Rabek JF, editors. Radiation Curing in Polymer Science and Technology, Volume III: Polymerisation Mechanisms. New York: Elsevier Science Publishers, Ltd., 1993. pp. 219-268.

11. Jacobine AF, Glaser DM, and Nakos ST. "Photoinitiated Cross-Linking of Norbornene Resins with Multifunctional Thiols". Acs Symposium Series 1990; 417:160-175.

12. Klemm E and Sensfuss S. "Addition Polymerization of Aliphatic Dithiols with Diene Monomers". Journal of Macromolecular Science-Chemistry 1991; A28(9):875-883.

13. Krongauz VV and Chawla CP. "Revisiting aromatic thiols effects on radical photopolymerization". Polymer 2003; 44(14):3871-3876.

14. Lecamp L, Houllier F, Youssef B, and Bunel C. "Photoinitiated cross-linking of a thiol-methacrylate system". Polymer 2001; 42(7):2727-2736.

15. Lee TY, Smith Z, Reddy SK, Cramer NB, et al. "Thiol-allyl ether-methacrylate ternary systems. Polymerization mechanism". Macromolecules 2007; 40(5):1466-1472.

16. Lu H, Carioscia JA, Stansbury JW, and Bowman CN. "Investigations of step-growth thiol-ene polymerizations for novel dental restoratives". Dental Materials 2005; 21(12):1129-1136.

17. Marvel CS and Cripps HN. "Polyalkylene Sulfides .10. the Reaction of Hexamethylenedithiol with 1,3-Butadiene". Journal of Polymer Science 1952; 8(3):313-320.

18. Marvel CS and Kotch A. "Polyalkylene Sulfides .7. the Polymer from Tetramethylenedithiol and Biallyl". Journal of the American Chemical Society 1951; 73(1):481-481.

19. Morgan CR, Magnotta F, and Ketley AD. "Thiol-Ene Photo-Curable Polymers". Journal of Polymer Science Part a-Polymer Chemistry 1977; 15(3):627-645.

20. Okay O and Bowman CN. "Kinetic modeling of thiol-ene reactions with both step and chain growth aspects". Macromolecular Theory and Simulations 2005; 14(4):267-277.

21. Reddy SK, Cramer NB, and Bowman CN. "Thiol-vinyl mechanisms. 1. Termination and propagation kinetics in thiol-ene photopolymerizations". Macromolecules 2006; 39(10):3673-3680.

22. Reddy SK, Cramer NB, and Bowman CN. "Thiol-vinyl mechanisms. 2. Kinetic modeling of ternary thiol-vinyl photopolymerizations". Macromolecules 2006; 39(10):3681-3687.

23. Reddy SK, Cramer NB, O'Brien AK, Cross T, et al. "Rate mechanisms of a novel thiol-ene photopolymerization reaction". Macromolecular Symposia 2004; 206:361-374.

24. Reddy SK, Okay O, and Bowman CN. "Network development in mixed step-chain growth thiol-vinyl photopolymerizations". Macromolecules 2006; 39(25):8832-8843.

25. Reddy SK, Sebra RP, Anseth KS, and Bowman CN. "Living radical photopolymerization induced grafting on thiol-ene based substrates". Journal of Polymer Science Part a-Polymer Chemistry 2005; 43(10):2134-2144.

26. Szmant HH, Mata AJ, Namis AJ, and Panthananickal AM. "Thiol-olefin co-oxidation (toco) reaction .4. Temperature effects on product distribution in toco reaction of indene and aromatic thiols". Tetrahedron 1976; 32(22):2665-2680.

27. Zonca Jr MR, Falk B, and Crivello JV. "LED-Induced Thiol-ene Photopolymerizations". Journal of Macromolecular Science: Pure & Applied Chemistry 2004; 41(7):741-756.

28. Carioscia JA, Lu H, Stanbury JW, and Bowman CN. "Thiol-ene oligomers as dental restorative materials". Dental Materials 2005; 21(12):1137-1143.

29. Carioscia JA, Schneidewind L, O'Brien C, Ely R, et al. "Thiol-norbornene materials: Approaches to develop high T-g thiol-ene polymers". Journal of Polymer Science Part a-Polymer Chemistry 2007; 45(23):5686-5696.

30. Carioscia JA, Stansbury JW, and Bowman CN. "Evaluation and control of thiol-ene/thiol-epoxy hybrid networks". Polymer 2007; 48(6):1526-1532.

31. Chiou BS, English RJ, and Khan SA. UV cross-linking of thiol-ene polymers: A rheological study. Photopolymerization, vol. 673, 1997. pp. 150-166.

32. Chiou BS, English RJ, and Khan SA. "Rheology and photo-cross-linking of thiol-ene polymers". Macromolecules 1996; 29(16):5368-5374.

33. Hoyle CE, Lee TY, and Roper T. "Thiol-enes: Chemistry of the past with promise for the future". Journal of Polymer Science Part A-Polymer Chemistry 2004; 42(21):5301-5338.

34. Jacobine AF, Glaser DM, Grabek PJ, Mancini D, et al. "Photocrosslinked Norbornene Thiol Copolymers - Synthesis, Mechanical-Properties, and Cure Studies". Journal of Applied Polymer Science 1992; 45(3):471-485.

35. Rydholm AE, Reddy SK, Anseth KS, and Bowman CN. "Development and characterization of degradable thiol-allyl ether photopolymers". Polymer 2007; 48(15):4589-4600.

36. Senyurt AF, Wei H, Phillips B, Cole M, et al. "Physical and mechanical properties of photopolymerized thiol-ene/acrylates". Macromolecules 2006; 39(19):6315-6317.

37. Senyurt AF, Wei HY, Hoyle CE, Piland SG, et al. "Ternary thiol-ene/acrylate photopolymers: Effect of acrylate structure on mechanical properties". Macromolecules 2007; 40(14):4901-4909.

38. Wei HY, Senyurt AF, Jonsson S, and Hoyle CE. "Photopolymerization of ternary thiol-ene/acrylate systems: Film and network properties". Journal of Polymer Science Part a-Polymer Chemistry 2007; 45(5):822-829.

39. Winter H, Nusselder JJH, and Steeman PAM. "Synthesis, characterization and mechanical properties of networks prepared from poly(propylene glycol) di(ethylmaleate) and a trifunctional thiol". Polymer 1996; 37(21):4841-4847.

40. Varadan VK, Vinoy KJ, and S. G. Smart material systems and MEMS design and development methodologies. Chichester, England: John Wiley & Sons, 2006.

41. Varadan VK, Jiang XY, and Varadan VV. Microstereolithography and other fabrication techniques for 3D MEMS. Chichester, England: Wiley, 2001.

42. Smith WF. Principles of Materials Science and Engineering, 3 ed. New York: McGraw-Hill, 1999.

43. Degarmo EP, Black JT, Kohser RA, and Klamecki BE. Materials and Processes in Manufacturing, 9 ed.: John Wiley & Sons, Inc., 2003.

44. Ward IM and Sweeney J. An Introduction to the Mechanical Properties of Solid Polymers, 2004.

45. Anseth KS, Wang CM, and Bowman CN. "Reaction behavior and kinetic constants for photopolymerizations of multi(meth)acrylate monomers". Polymer 1994; 35(15):3243-3250.

46. Decker C. "New developments in UV radiation curing of protective coatings". Surface Coatings International Part B-Coatings Transactions 2005; 88(1):9-17.

47. Decker C. "Kinetic study and new applications of UV radiation curing". Macromolecular Rapid Communications 2002; 23(18):1067-1093.

48. Decker C. "The use of UV irradiation in polymerization". Polymer International 1998; 45(2):133-141.

49. Decker C, Bendaikha T, Decker D, and Zahouily K. "High-speed polymerization of acrylate monomers by UV irradiation". Abstracts of Papers of the American Chemical Society 1997; 213:210-POLY.

50. Decker C, Elzaouk B, and Decker D. "Kinetic study of ultrafast photopolymerization reactions". Journal of Macromolecular Science-Pure and Applied Chemistry 1996; A33(2):173-190.

51. Decker C. "Photoinitiated curing of multifunctional monomers". Acta Polymerica 1994; 45(5):333-347.

52. Decker C. "uv curing of acrylate coatings by laser-beams". Journal of Coatings Technology 1984; 56(713):29-34.

53. Anseth KS and Bowman CN. "Reaction behavior and kinetics of multifunctional (meth)acrylate photopolymerizations". Abstracts of Papers of the American Chemical Society 1994; 207:427.

54. Dietz JE, Elliott BJ, and Peppas NA. "Real-time attenuated total reflectance fourier-transform infrared-spectroscopy to monitor multiacrylate polymerization reactions". Macromolecules 1995; 28(15):5163-5166.

55. Baldacchini T, LaFratta CN, Farrer RA, Teich MC, et al. "Acrylic-based resin with favorable properties for three-dimensional two-photon polymerization". Journal of Applied Physics 2004; 95(11):6072-6076.

56. Chang LC and Read TA. "Experimental Evidence of Relaxation During Diffusionless Phase Changes of Single Crystal Beta-Au-Cd Alloys Containing 47.5 Atomic Percent Cd". Physical Review 1951; 82(5):770-770.

57. Buehler WJ and Wiley RC. Naval Ordnance Laboratory Report, 1961. pp. 61-75.

58. Delange RG and Zijderve J.A. "Shape-Memory Effect and Martensitic Transformation of TiNi". Journal of Applied Physics 1968; 39(5):2195-&.

59. Echigo S, Matsuda T, and Kamiya T. "Development of device made of shape memory polymer for closure of ductus arteriosus". Japanese Journal of Artificial Organs 1990; 19(3):1186-1189.

60. Kimura H and Teraoka F. "Application of shape memory polymer to dental materials (part 1). Physical properties". J Osaka Univ Dent Sch 1986; 26:59-65.

61. Tobushi H, Hayashi S, and Kojima S. "Mechanical-properties of shape memory polymer of polyurethane series - (basic characteristics of stress-strain-temperature relationship)". Jsme International Journal Series I-Solid Mechanics Strength of Materials 1992; 35(3):296-302.

62. Ward RS. "Softenable shape-memory thermoplastics for biomedical use". Medical Device and Diagnostic Industry 1985; 7(8):24, 26, 28, 30, 32.

63. Gall K, Yakacki CM, Liu YP, Shandas R, et al. "Thermomechanics of the shape memory effect in polymers for biomedical applications". Journal of Biomedical Materials Research Part A 2005; 73A(3):339-348.

64. Yakacki CM, Lyons MB, Rech B, Gall K, et al. "Cytotoxicity and thermomechanical behavior of biomedical shape-memory polymer networks post-sterilization". Biomedical Materials 2008; 3(1).

65. Yakacki CM, Shandas R, Lanning C, Rech B, et al. "Unconstrained recovery characterization of shape-memory polymer networks for cardiovascular applications". Biomaterials 2007; 28(14):2255-2263.

66. Wood JH. Frameless aircraft canopy actuation system and method. In: Office USP, editor. United States of America, 2003.

67. Spartech Corp., 2007.

68. Krieg M, Weber C, and Szigeti P. Transparent plastic pane containing a copolymer of methylmethacrylate and polyfunctional acrylates. In: Office USP, editor. United States of America, 1997.

69. Labra JJ. "Finite-element modeling of a fighter aircraft canopy acrylic panel". Journal of Aircraft 1982; 19(6):480-484.

70. Kent Periscopes Inc., 2008.

71. Uniscope Optical Systems Inc., 2008.

72. Yang S-J and Abel R. Stabilized UV transparent acrylic composition. In: Office USP, editor. United States of America, 2008.

73. Hashida T, Ando E, and Goto Y. Optical storage media. In: Office USP, editor. United States of America, 1992.

74. Ward JM. Plexiglas speakers. In: Office USP, editor. United States of America, 1976.

75. Anan K, Murata Y, Amaya N, and Miyazaki T. Contact lens. In: Office USP, editor. United States of America, 1999.

76. Muniz Plastics. 2008.

77. Santini AF. Washable acrylic paint. In: Office USP, editor. United States of America, 1994.

78. Weiss P and Cheever GD. Powdered acrylic paint composition and method. In: Office USP, editor. United States of America, 1976.

79. Junkin JH, Ginn ME, and Fronczak ET. Powder-resistant acrylic polymer floor finishes. In: Office USP, editor. United States of America, 1974.

80. Everaerts AI, Purgett MD, and Momchilovich BS. Tackified acrylic adhesives. In: Office USP, editor. United States of America, 1994.

81. Stow RH. Solvent-resistant pressure-sensitive adhesive tape. In: Office USP, editor., 1960.

82. Edelman R and Catena WJ. Rapid curing structural acrylic adhesive. In: Office USP, editor. United States of America, 1999.

83. Kondo K, Hoshida S, Aizawa M, and Amano T. Acrylic adhesive sheet. In: Office USP, editor. United States of America, 2008.

84. Safranski DL and Gall K. "Effect of Chemical Structure and Crosslinking Density on the Thermo-Mechanical Properties and Toughness of (Meth)acrylate Shape-Memory Polymer Networks". Polymer 2008.

85. Sawhney AS, Pathak CP, and Hubbell JA. "Bioerodible hydrogels based on photopolymerized poly(ethylene glycol)-co-poly(alpha-hydroxy acid) diacrylate macromers". Macromolecules 1993; 26(4):581-587.

86. Sawhney AS, Pathak CP, Vanrensburg JJ, Dunn RC, et al. "Optimization of photopolymerized bioerodible hydrogel properties for adhesion prevention". Journal of Biomedical Materials Research 1994; 28(7):831-838.

87. West JL and Hubbell JA. "Photopolymerized hydrogel materials for drug-delivery applications". Reactive Polymers 1995; 25(2-3):139-147.

88. Feng ZG and Zhao SP. "Synthesis and characterization of biodegradable hydrogels based on photopolymerizable acrylate-terminated CL-PEG-CL macromers with supramolecular assemblies of alpha-cyclodextrins". Polymer 2003; 44(18):5177-5186.

89. Hern DL and Hubbell JA. "Incorporation of adhesion peptides into nonadhesive hydrogels useful for tissue resurfacing". Journal of Biomedical Materials Research 1998; 39(2):266-276.

90. Martens P, Holland T, and Anseth KS. "Synthesis and characterization of degradable hydrogels formed from acrylate modified poly(vinyl alcohol) macromers". Polymer 2002; 43(23):6093-6100.

91. Lu SX and Anseth KS. "Release behavior of high molecular weight solutes from poly(ethylene glycol)-based degradable networks". Macromolecules 2000; 33(7):2509-2515.

92. Martens P, Metters AT, Anseth KS, and Bowman CN. "A generalized bulk-degradation model for hydrogel networks formed from multivinyl cross-linking molecules". Journal of Physical Chemistry B 2001; 105(22):5131-5138.

93. Ortega AM, Kasprzak SE, Yakacki CM, Diani J, et al. "Structure–Property Relationships in Photopolymerizable Polymer Networks: Effect of Composition on the Crosslinked Structure and Resulting Thermomechanical Properties of a (Meth)acrylate-Based System". Journal of Applied Polymer Science 2008; 110:1559-1572.

94. Treloar LRG. The Physics of Rubber Elasticity, 2nd. ed. London: Oxford University Press, 1958.

95. Elliott JE and Bowman CN. "Kinetics of primary cyclization reactions in cross-linked polymers: An analytical and numerical approach to heterogeneity in network formation". Macromolecules 1999; 32(25):8621-8628.

96. Posner T. "Information on unsaturated compounds II The addition of mercaptan to unsaturated hydrocarbon". Berichte Der Deutschen Chemischen Gesellschaft 1905; 38:646-657.

97. Kharasch MS, Nudenberg W, and Mantell GJ. "Reactions of atoms and free radicals in solution .25. The reactions of olefins with mercaptans in the presence of oxygen". Journal of Organic Chemistry 1951; 16(4):524-532.

98. O'Brien AK, Cramer NB, and Bowman CN. "Oxygen inhibition in thiol-acrylate photopolymerizations". Journal of Polymer Science Part a-Polymer Chemistry 2006; 44(6):2007-2014.

99. Lee TY, Carioscia J, Smith Z, and Bowman CN. "Thiol-allyl ether-methacrylate ternary systems. Evolution mechanism of polymerization-induced shrinkage stress and mechanical properties". Macromolecules 2007; 40(5):1473-1479.

100. Kharasch MS, Read AT, and Mayo FR. Chemistry and Industry 1938; (57):752.

101. Marvel CS and Aldrich PH. "Polyalkylene Sulfides .2. Preparation of Polyhexamethylene Sulfide in Emulsion". Journal of the American Chemical Society 1950; 72(5):1978-1981.

102. Marvel CS and Baumgarten HE. "Polyalkylene Sulfides with Rubberlike Properties". Journal of Polymer Science 1951; 6(2):127-143.

103. Marvel CS and Chambers RR. "Polyalkylene Sulfides from Diolefins and Dimercaptans". Journal of the American Chemical Society 1948; 70(3):993-998.

104. Marvel CS and Cripps HN. "Polyalkylene Sulfides Containing Silicon .11". Journal of Polymer Science 1952; 9(1):53-60.

105. Marvel CS, Hinman CW, and Inskip HK. "Polyalkylene Sulfides .12. Termination by Disulfide Formation". Journal of the American Chemical Society 1953; 75(8):1997-1998.

106. Marvel CS and Markhart AH. "Polyalkylene Sulfides .6. New Polymers Capable of Cross-Linking". Journal of Polymer Science 1951; 6(6):711-716.

107. Marvel CS and Markhart AH. "Polyalkylene Sulfides .5. the Rate of Formation in Emulsion". Journal of the American Chemical Society 1951; 73(3):1064-1065.

108. Marvel CS and Nowlin G. "Polyalkylene Sulfides .4. the Effect of Ph on Polymer Size". Journal of the American Chemical Society 1950; 72(11):5026-5029.

109. Marvel CS and Olson LE. "Polyalkylene Sulfides .13. Polymers from 4-Vinyl-1-Cyclohexene and D-Limonene". Journal of Polymer Science 1957; 26(112):23-28.

110. Marvel CS and Roberts CW. "Polyalkylene Sulfides .8. Polymers from 4-Vinylcyclohexene". Journal of Polymer Science 1951; 6(6):717-724.

111. Rakas MA and Jacobine AF. "Mechanical and Dynamic Mechanical-Properties of Photocrosslinked Norbornene-Thiol Copolymer Films". Journal of Adhesion 1992; 36(4):247-263.

112. Oliver WC and Pharr GM. "Measurement of hardness and elastic-modulus by instrumented indentation: Advances in understanding and refinements to methodology". Journal of Materials Research 2004; 19(1):3-20.

113. Oliver WC and Pharr GM. "An improved technique for determining hardness and elastic modulus using load and displacement sensing indentation experiments". Journal of Materials Research 1992; 7(6):1564-1583.

114. Lee D, Zhao MH, Wei XD, Chen X, et al. "Observation of plastic deformation in freestanding single crystal Au nanowires". Applied Physics Letters 2006; 89(11):3.

115. Pharr GM, Oliver WC, and Brotzen FR. "On the Generality of the Relationship among Contact Stiffness, Contact Area, and Elastic-Modulus During Indentation". Journal of Materials Research 1992; 7(3):613-617.

116. Lee D, Wei X, Chen X, Zhao M, et al. "Microfabrication and mechanical properties of nanoporous gold at the nanoscale". Scripta Materialia 2007; 56(5):437-440.

117. Herbert EG, Oliver WC, and Pharr GM. On the measurement of yield strength by spherical indentation. Taylor & Francis Ltd, 2006. pp. 5521-5539.

118. Herbert EG, Pharr GM, Oliver WC, Lucas BN, et al. "On the measurement of stress-strain curves by spherical indentation". Thin Solid Films 2001; 398:331-335.

119. Cao YF, Yang DH, and Soboyejoy W. "Nanoindentation method for determining the initial contact and adhesion characteristics of soft polydimethylsiloxane". Journal of Materials Research 2005; 20(8):2004-2011.

120. Shen L, Tjiu WC, and Liu TX. "Nanoindentation and morphological studies on injection-molded nylon-6 nanocomposites". Polymer 2005; 46(25):11969-11977.

121. Tweedie CA and Van Vliet KJ. "Contact creep compliance of viscoelastic materials via nanoindentation". Journal of Materials Research 2006; 21(6):1576-1589.

122. Yashiro K, Furuta A, and Tomita Y. Molecular dynamics simulation of nanoindentation on folded chain crystal of polyethylene. Advances in Fracture and Strength, Pts 1- 4, vol. 297-300, 2005. pp. 2247-2252.

123. Herbert EG, Oliver WC, and Pharr GM. "Nanoindentation and the dynamic characterization of viscoelastic solids". Journal of Physics D-Applied Physics 2008; 41(7).

124. Gall K, Dunn ML, Liu Y, Finch D, et al. "Shape memory polymer nanocomposites". Acta Materialia 2002; 50:5115-5126.

125. Maruo S and Kawata S. "Two-photon-absorbed near-infrared photopolymerization for three-dimensional microfabrication". Journal of Microelectromechanical Systems 1998; 7(4):411-415.

126. Maruo S, Nakamura O, and Kawata S. "Three-dimensional microfabrication with two-photon-absorbed photopolymerization". Optics Letters 1997; 22(2):132-134.

127. Zhou W, Kuebler SM, Braun KL, Yu T, et al. "An Efficient Two-Photon-Generated Photoacid Applied to Positive-Tone 3D Microfabrication". Science 2000; 296(5570):1106-1109.

128. Cumpston BH, Ananthavel SP, Barlow S, Dyer DL, et al. "Two-photon polymerization initiators for three-dimensional optical data storage and microfabrication". Nature 1999; 398(6722):51-54.

129. Kawata S and Sun H-B. "Two-Photon Photopolymerization of Functional Micro-Devices". Journal of Photopolymer Science and Technology 2002; 15(3):471-474.

130. Sun H-B and Kawata S. "Two-Photon Laser Precision Microfabrication and Its Applications to Micro-Nano Devices and Systems". Journal of Lightwave Technology 2003; 21(3):624-633.

131. Sun H-B, Maeda M, Takada K, Chon JWM, et al. "Experimental investigation of single voxels for laser nanofabrication via two-photon photopolymerization". Applied Physics Letters 2003; 83(5):819-821.

132. Belfield KD and Schafer KJ. Two-photon photoinitiated polymerization. Photoinitiated Polymerization, vol. 847, 2003. pp. 464-481.

133. Lu Y, Hasegawa F, Okhuma S, Goto T, et al. "Highly efficient two-photon initiated polymerization in solvent by using a novel two-photon chromophore and co-initiators". Journal of Materials Chemistry 2004; 14:1391-1395.

134. Lee C-H, Chang T-W, Lee K-L, Lin J-Y, et al. "Fabricating high-aspect-ratio sub-diffraction-limit structures on silicon with two-photon photopolymerization and reactive ion etching". Applied Physics A 2004; 79:2027-2031.

135. Stute U, Serbin J, Kulik C, and Chichkov BN. "Three-dimensional micro- and nanostructuring with two-photon polymerisation". International Journal of Materials and Product Technology 2004; 21(4):273-284.

136. Duan X-M, Sun H-B, and Kawata S. "Microfabrication of Two and Three Dimensional Structures by Two-Photon Polymerization". Journal of Photopolymer Science and Technology 2004; 17(3):393-396.

137. Sun H-B and Kawata S. "Two-Photon Photopolymerization and 3D Lithographic Microfabrication". Applied Physics Letters 2004; 170:169-273.

138. Lu Y, Hasegawa F, Goto T, Okhuma S, et al. "Highly sensitive measurement in two-photon absorption cross section and investigation of the mechanism of two-photon-induced polymerization". Journal of Luminescence 2004; 110:1-10.

139. Kang BY, Wu JW, Lee K-S, Rhee BK, et al. "Fabrication of 3D Nano-Structures by Using Two-Photon Absorption Polymerization". Journal of the Korean Physical Society 2004; 45(5):1154-1157.

140. Lemercier G, Mulatier J-C, Martineau C, Anémian R, et al. "Two-photon absorbtion: from optical power limiting to 3D microfabrication". Compte Rednus Chimie 2005; 8:1308-1316.

141. Yan Y-X, Tao X-T, Sun Y-H, Xu G-B, et al. "Two new asymmetrical two-photon photopolymerization initiators: Synthesis, characterization and nonlinear optical properties". Optical Materials 2005; 27:1787-1792.

142. Park SH, Lim TW, Lee SH, Yang D-Y, et al. "Fabrication of Microstructures Using Double Countour (DCS) Method by Two-Photon Polymerization". Polymer (Korea) 2005; 29(2):146-150.

143. Lim TW, Park SH, Yang D-Y, Kong HJ, et al. "Fabrication of Three-Dimensional Curved Microstructures by Two-Photon Polymerization Employing Multi-Exposure Voxel Matrix Scanning Method". Polymer (Korea) 2005; 29(4):418-421.

144. Strickler JH and Webb WW. "3-dimensional optical-data storage in refractive media by 2-photon point excitation". Optics Letters 1991; 16(22):1780-1782.

145. Marder SR, Bredas JL, and Perry JW. "Materials for multiphoton 3D microfabrication". Mrs Bulletin 2007; 32(7):561-565.

146. Dong WT and Perry JW. "Two-photon microfabrication of photonic crystal structures using titania-polymer hybrid materials". Abstracts of Papers of the American Chemical Society 2006; 231.

147. Perry JW. "3-D microfabrication, sensing and imaging with two-photon". Abstracts of Papers of the American Chemical Society 2005; 230:U317-U317.

148. Perry JW, Dong WT, Chen V, Zhou J, et al. "Two-photon 3-D micro- and nano-fabrication with polymer, metal nanocomposite and hybrid materials". Abstracts of Papers of the American Chemical Society 2006; 231.

149. Zheng SJ, Leclercq A, Fu J, Beverina L, et al. "Two-photon absorption in quadrupolar bis(acceptor)-terminated chromophores with electron-rich bis(heterocycle)vinylene bridges". Chemistry of Materials 2007; 19(3):432-442.

150. Watanabe T, Akiyama M, Totani K, Kuebler SM, et al. "Photoresponsive hydrogel microstructure fabricated by two-photon initiated polymerization". Advanced Functional Materials 2002; 12(9):611-614.

151. Yu TY, Ober CK, Kuebler SM, Zhou WH, et al. "Chemically amplified positive resists for two-photon three-dimensional microfabrication". Advanced Materials 2003; 15(6):517-521.

152. Yu TY, Ober CK, Zhou WH, Kuebler SM, et al. "Two-photon positive tone lithography for 3-D micro fabrication". Abstracts of Papers of the American Chemical Society 2002; 224:U502-U502.

153. Cumpston BH, Ananthavel SP, Barlow S, Dyer DL, et al. "Two-photon polymerization initiators for three-dimensional optical data storage and microfabrication". Nature 1999; 398(4):51-54.

154. Kuebler SM, Braun KL, Zhou WH, Cammack JK, et al. "Design and application of high-sensitivity two-photon initiators for three-dimensional microfabrication". Journal of Photochemistry and Photobiology a-Chemistry 2003; 158(2-3):163-170.

155. Marder SR. "Two-photon absorption chemistry". Abstracts of Papers of the American Chemical Society 2002; 224:U108-U108.

156. Kogej T, Beljonne D, Meyers F, Perry JW, et al. "Mechanisms for enhancement of two-photon absorption in donor-acceptor conjugated chromophores". Chemical Physics Letters 1998; 298(1-3):1-6.

157. Lipson M, Levin MD, Perry JW, and Marder SR. "The photochemistry and photophysics of some rationally designed two-photon absorbing chromophores". Abstracts of Papers of the American Chemical Society 1998; 216:U459-U459.

158. Perry JW, Albota M, Ananthavel S, Beljonne D, et al. "Design of organic molecules with large two-photon absorption cross-sections". Abstracts of Papers of the American Chemical Society 1999; 217:U378-U378.

159. Hertz H. On the Contact of Elastic Solids. In: Jones DE and Schott GA, editors. Miscellaneous Papers by Heinrich Hertz. London: MacMillan and Co., 1896. pp. 146-162.

160. Hertz H. On the Contact of Rigid Elastic Solids and on Hardness. In: Jones DE and Schott GA, editors. Miscellaneous Papers by Heinrich Hertz. London: MacMillan and Co., 1896. pp. 163-183.

161. Love AEH. "The Stress Produced in a Semi-Infinite Solid by Pressure on Part of the Boundary". Philosophical Transactions of the Royal Society of London. Series A, Containing Papers of a Mathematical or Physical Character 1929; 228:377-420.

162. Love AEH. "Boussinesq's problem for a rigid cone". Quarterly Journal of Mathematics 1939; 10:161-175.

163. Sneddon IN. "The relation between load and penetration in the axisymmetric Boussinesq problem for a punch of arbitrary profile". International Journal of Engineering Science 1965; 3:47-57.

164. King RB. "Elastic Analysis of Some Punch Problems for a Layered Medium". International Journal of Solids and Structures 1987; 23(12):1657-1664.

165. Fischer-Cripps AC. Nanoindentation. New York: Springer-Verlag, 2002.

166. VanLandingham MR, Chang N-K, Drzal PL, White CC, et al. "Viscoelastic characterization of polymers using instrumented indentation. I. Quasi-static testing". Journal of Polymer Science: Part B: Polymer Physics 2005; 43:1794-1811.

167. White CC, VanLandingham MR, Drzal PL, Chang N-K, et al. "Viscoelastic characterization of polymers using instrumented indentation. II. Dynamic testing". Journal of Polymer Science: Part B: Polymer Physics 2005; 43:1812-1824.

168. VanLandingham MR, Villarrubia JS, Guthrie WF, and Meyers GF. "Nanoindentation of Polymers: An Overview". Macromol. Symp. 2001; 167:15-43.

169. Lu H, Wang B, Ma J, Huang G, et al. "Measurement of creep compliance of solid polymers by nanoindentation". Mechanics of Time-Dependent Materials 2003; 7(3-4):189-207.

170. Maner KC, Begley MR, and Oliver WC. "Nanomechanical testing of circular freestanding polymer films with sub-micron thickness". Acta Materialia 2004; 52:5451-5460.

171. Zhang TY, Wang XS, and Huang B. "Microbridge testing of thin films". Materials Science and Engineering A-Structural Materials Properties Microstructure and Processing 2005; 409(1-2):329-339.

172. Bonin WA and Hysitron. Multi-dimensional capacitive transducer. In: Office USPaT, editor. United States, 1997.

173. Bonin WA and Hysitron. Multi-dimensional capacitive transducer. United States, 1999.

174. Field JS. Penetrating measuring instrument. United States, 1991.

175. Russell PE, Stark TJ, Griffis DP, Phillips JR, et al. "Chemically and geometrically enhanced focused ion beam micromachining". Journal of Vacuum Science & Technology B 1998; 16(4):2494-2498.

176. Yu N and Polycarpou AA. "Use of the focused ion beam technique to produce a sharp spherical diamond indenter for sub-10 nm nanoindentation measurements". Journal of Vacuum Science & Technology B 2004; 22(2):668-672.

177. VanLandingham MR, Juliano TF, and Hagon MJ. "Measuring tip shape for instrumented indentation using atomic force microscopy". Measurement Science and Technology 2005; 16:2173-2185.

178. Feng G and Ngan AHW. "Effects of creep and thermal drift on modulus measurement using depth-sensing indentation". Journal of Materials Research 2002; 17(3):660-668.

179. Briscoe BJ, Fiori L, and Pelillo E. "Nano-indentation of polymeric surfaces". J. Phys. D: Applied Physics 1998; 31:2395-2405.

180. Roberts SG, Lawrence CW, Bisrat Y, and Warren PD. "Determination of surface residual stresses in brittle materials by Hertzian indentation: Theory and experiment". Journal of the American Ceramic Society 1999; 82(7):1809-1816.

181. Haske W, Chen VW, Hales JM, Dong WT, et al. "65 nm feature sizes using visible wavelength 3-D multiphoton lithography". Optics Express 2007; 15(6):3426-3436.

182. Chen V and Perry JW. "Unpublished results". 2009.

183. Lovell LG, Newman SM, and Bowman CN. "The effects of light intensity, temperature, and comonomer composition on the polymerization behavior of dimethacrylate dental resins". Journal of Dental Research 1999; 78(8):1469-1476.

184. Decker C, Decker D, and Morel F. Light intensity and temperature effect in photoinitiated polymerization. Photopolymerization, vol. 673, 1997. pp. 63-80.

185. Fox TG and Loshaek S. "Influence of molecular weight and degree of crosslinking on the specific volume and glass temperature of polymers". Journal of Polymer Science 1955; 15(80):371-390.

186. Loshaek S. "Crosslinked polymers .2. Glass temperatures of copolymers of methyl methacrylate and glycol dimethacrylates". Journal of Polymer Science 1955; 15(80):391-404.

187. Bicerano J, Sammler RL, Carriere CJ, and Seitz JT. "Correlation between glass transition temperature and chain structure for randomly crosslinked high polymers". Journal of Polymer Science Part B-Polymer Physics 1996; 34(13):2247-2259.

188. Kannurpatti AR, Anseth JW, and Bowman CN. "A study of the evolution of mechanical properties and structural heterogeneity of polymer networks formed by photopolymerizations of multifunctional (meth)acrylates". Polymer 1998; 39(12):2507-2513.

189. Greenberg AR and Kusy RP. "Influence of crosslinking on the glass-transition of poly(acrylic acid)". Journal of Applied Polymer Science 1980; 25(8):1785-1788.

190. Young JS, Kannurpatti AR, and Bowman CN. "Effect of comonomer concentration and functionality on photopolymerization rates, mechanical properties and heterogeneity of the polymer". Macromolecular Chemistry and Physics 1998; 199(6):1043-1049.

191. Thian SCH, Tang Y, Fuh JYH, Wong YS, et al. "Micro-rapid-prototyping via multi-layered photo-lithography". International Journal of Advanced Manufacturing Technology 2006; 29(9-10):1026-1032.

192. Duffy DC, McDonald JC, Schueller OJA, and Whitesides GM. "Rapid prototyping of microfluidic systems in poly(dimethylsiloxane)". Analytical Chemistry 1998; 70(23):4974-4984.

193. Duffy DC, Schueller OJA, Brittain ST, and Whitesides GM. "Rapid prototyping of microfluidic switches in poly(dimethyl siloxane) and their actuation by electro-osmotic flow". Journal of Micromechanics and Microengineering 1999; 9(3):211-217.

194. Anderson JR, Chiu DT, Jackman RJ, Cherniavskaya O, et al. "Fabrication of topologically complex three-dimensional microfluidic systems in PDMS by rapid prototyping". Analytical Chemistry 2000; 72(14):3158-3164.

195. Hoettges KF, Gwilliam RM, Homewood KP, and Stevenson D. Fast prototyping of microfluidic devices for separation science. Vieweg, 2001. pp. S424-S426.

196. Farsari M, Claret-Tournier F, Huang S, Chatwin CR, et al. "A novel high-accuracy microstereolithography method employing an adaptive electro-optic mask". Journal of Materials Processing Technology 2000; 107(1-3):167-172.

197. Haraldsson KT, Hutchison JB, Sebra RP, Good BT, et al. "3D polymeric microfluidic device fabrication via contact liquid photolithographic polymerization (CLiPP)". Sensors and Actuators B 2006; 113:454-460.

198. Hutchison JB, Haraldsson KT, Good BT, Sebra RP, et al. "Robust polymer microfluidic device fabrication via contact liquid photolithographic polymerization (CLiPP)". Lab on a Chip 2004; 4(6):658-662.

199. Betancourt T and Brannon-Peppas L. "Micro- and nanofabrication methods in nanotechnological medical and pharmaceutical devices". International Journal of Nanomedicine 2006; 1(4):483-495.

200. Cong HL and Pan TR. "Photopatternable conductive PDMS materials for microfabrication". Advanced Functional Materials 2008; 18(13):1912-1921.

201. Becker H and Gartner C. "Polymer microfabrication methods for microfluidic analytical applications". Electrophoresis 2000; 21(1):12-26.

202. O'Brien J, Hughes PJ, Brunet M, O'Neill B, et al. "Advanced photoresist technologies for microsystems". Journal of Micromechanics and Microengineering 2001; 11(4):353-358.

203. Linder V, Wu HK, Jiang XY, and Whitesides GM. "Rapid prototyping of 2D structures with feature sizes larger than 8 mu m". Analytical Chemistry 2003; 75(10):2522-2527.

204. Dellmann L, Roth S, Beuret C, Paratte L, et al. "Two steps micromoulding and photopolymer high-aspect ratio structuring for applications in piezoelectric motor components". Microsystem Technologies-Micro-and Nanosystems-Information Storage and Processing Systems 1998; 4(3):147-150.

205. Dellmann L, Roth S, Beuret C, Racine GA, et al. "Fabrication process of high aspect ratio elastic and SU-8 structures for piezoelectric motor applications". Sensors and Actuators A-Physical 1998; 70(1-2):42-47.

206. Lorenz H, Despont M, Fahrni N, Brugger J, et al. "High-aspect-ratio, ultrathick, negative-tone near-UV photoresist and its applications for MEMS". Sensors and Actuators A-Physical 1998; 64(1):33-39.

207. Lorenz H, Despont M, Vettiger P, and Renaud P. "Fabrication of photoplastic high-aspect ratio microparts and micromolds using SU-8 UV resist". Microsystem Technologies 1998; 4(3):143-146.

208. Myung D, Koh W, Bakri A, Zhang F, et al. "Design and fabrication of an artificial cornea based on a photolithographically patterned hydrogel construct". Biomedical Microdevices 2007; 9(6):911-922.

209. Bens A, Seitz H, Bermes G, Emons M, et al. "Non-toxic flexible photopolymers for medical stereolithography technology". Rapid Prototyping Journal 2007; 13(1):38-47.

210. Bland MH and Peppas NA. "Photopolymerized multifunctional (meth)acrylates as model polymers for dental applications". Biomaterials 1996; 17(11):1109-1114.

211. Kou HG, Asif A, and Shi WF. "Hyperbranched acrylated aromatic polyester used as a modifier in UV-curable epoxy acrylate resins". Chinese Journal of Chemistry 2003; 21(1):91-95.

212. Wei HY, Kou HG, Shi WF, Nie KM, et al. "Photopolymerizable hyperbranched (meth)acrylated poly(amine ester)". Journal of Applied Polymer Science 2003; 87(2):168-173.

213. Schmidt LE, Yi S, Jin YH, Leterrier Y, et al. "Acrylated hyperbranched polymer photoresist for ultra-thick and low-stress high aspect ratio micropatterns". Journal of Micromechanics and Microengineering 2008; 18(4).

214. Karrer P, Corbel S, Andre JC, and Lougnot DJ. "Shrinkage effects in photopolymerizable resins containing filling agents - application to stereophotolithography". Journal of Polymer Science Part a-Polymer Chemistry 1992; 30(13):2715-2723.

215. Linden LA and Jakubiak J. "Contraction (shrinkage) in polymerization - Part II. Dental resin composites". Polimery 2001; 46(9):590-595.

216. Gan ZW, Mo JH, Huang SH, and Xie HQ. "Development of a hybrid photopolymer for stereolithography". Journal of Wuhan University of Technology-Materials Science Edition 2006; 21(1):99-101.

217. Vaessen DM, Ngantung FA, Palacio MLB, Francis LF, et al. "Effect of lamp cycling on conversion and stress development in ultraviolet-cured acrylate coatings". Journal of Applied Polymer Science 2002; 84(14):2784-2793.

218. Beebe DJ, Moore JS, Bauer JM, Yu Q, et al. "Functional hydrogel structures for autonomous flow control inside microfluidic channels". Nature 2000; 404(6778):588-+.

219. Beebe DJ, Moore JS, Yu Q, Liu RH, et al. "Microfluidic tectonics: A comprehensive construction platform for microfluidic systems". Proceedings of the National Academy of Sciences of the United States of America 2000; 97(25):13488-13493.

220. Bryant SJ, Hauch KD, and Ratner BD. "Spatial patterning of thick poly(2-hydroxyethyl methacrylate) hydrogels". Macromolecules 2006; 39(13):4395-4399.

221. Jung KH and Bae BS. "Synthesis and characterization of photopatternable epoxy hybrid materials for the fabrication of thick and thermally stable microstructures with a high aspect ratio". Journal of Applied Polymer Science 2008; 108(5):3169-3176.

222. Stohr U, Vulto P, Hoppe P, Urban G, et al. "High-resolution permanent photoresist laminate for microsystem applications". Journal of Micro-Nanolithography Mems and Moems 2008; 7(3).

223. MicroChem Inc. SU-8 Resists. 2008.

224. Tokyo OHKA Kogyo Co. Permanent Photoresist for MEMS. 2008.

225. Perry JW, Haske W, Rumi M, Marder SR, et al. "Two-photon 3D lithography: Materials and applications". Abstracts of Papers of the American Chemical Society 2004; 228:U444-U444.

226. DeVor RE, Chang T, and Sutherland JW. Statistical Quality Design and Control: Contemporary Concepts and Methods. New York: Macmillan, 1992.

227. NIH. ImageJ - Image Processing and Analysis in Java. 2009.